SYNTHESIS, STRUCTURE, AND PROPERTIES OF NEW GERMANATE PHASES

SYNTHESIS, STRUCTURE, AND LUMINESCENT PROPERTIES OF NEW GERMANATE PHASES

By SERGEI NOVIKOV, B.Sc.

A Thesis Submitted to the School of Graduate Studies

in Partial Fulfilment of the Requirements for Degree Doctor of Philosophy

McMaster University

McMaster University DOCTOR OF PHILOSOPHY (2022) Hamilton, Ontario (Chemistry)

TITLE: Synthesis, structure, and luminescent properties of new germanate phases

AUTHOR: Sergei Novikov, B.Sc. (Samara State University, Samara, Russia)

SUPERVISOR: Professor Yurij Mozharivskyj

NUMBER OF PAGES: xx, 157

Lay Abstract

In the past two decades a significant decrease in the energy consumption for the lighting purposes was achieved. The more efficient sources of white light for the general purposes rely on the phenomenon of luminescence. Search of new efficient luminescent materials, known as phosphors, is ongoing. Rigorous study is required before a new material can be considered as a good candidate for practical applications.

In this work we focus on the phases emitting red light, which is crucial for the high-quality lighting. During the research, we prepared a series of inorganic materials that demonstrate red luminescence after the doping with Mn^{4+}. We characterized the structures of the new phases, optimized their synthesis procedures, and studied their properties. The combined information on the composition, structure, and properties is vital for the practical applications. These results are also critical for the further performance optimization of the new phosphors.

Abstract

A series of new germanates was prepared and their structures were characterized with X-ray diffraction (XRD). We employed solid-state synthesis, flux growth, and crystallization from melts to obtain crystals of the new materials. The crystals were studied by means of single crystal XRD, providing the information on the structure and composition of the new materials. Germanates suitable to accommodate Mn^{4+} – a well-known activator ion for the preparation of the rare-earth-free red phosphors – were of a particular interest. The Ge^{4+} substitution for Mn^{4+} is possible if the crystal structure features octahedrally coordinated germanium atoms, and we indeed were able to prepare such germanates.

The crystal structures of the following phases were characterized: $Mg_3Ge_{1-\delta}O_{4(1-\delta)}F_{2(1+2\delta)}$ ($\delta \approx 0.1$), $Mg_{14}Ge_4O_{20}F_4$, $Mg_2Pb_2Ge_2O_7F_2$, $Sr_3GeO_4Cl_2$, $Ba_3GeO_4Br_2$, $Sr_6Ge_2O_7Cl_6$, $Ba_5GeO_4Br_6$, $Na_2BaGe_8O_{18}$, $Rb_2BaGe_8O_{18}$, $Na_{0.36}Sr_{0.82}Ge_4O_9$, $Na_2SrGe_6O_{14}$, and $K_2SrGe_8O_{18}$. Two phases, $Mg_3Ge_{1-\delta}O_{4(1-\delta)}F_{2(1+2\delta)}$ and $Na_{0.36}Sr_{0.82}Ge_4O_9$ demonstrate deficiency on certain crystallographic sites. We analyzed the connectivity of the GeO_4 and GeO_6 units in the new and reported tetra- and octagermanates. Despite the similar stoichiometry, the connectivity of GeO_n polyhedra is different in $R^I_2Ge_4O_9$, $R^{II}Ge_4O_9$ and $R^IR^{II}Ge_8O_{18}$ germanates (R^I = alkali, R^{II} = alkaline earth metal).

The Ge^{4+} substitution for Mn^{4+} was successfully done for the $Na_2BaGe_8O_{18}$, $Rb_2BaGe_8O_{18}$, $Na_2SrGe_6O_{14}$, and $K_2SrGe_8O_{18}$ phases yielding new red phosphors. Based on the powder XRD data, the optimal synthetic strategies were developed yielding high purity (≈ 99 wt. %) samples. The photoluminescent excitation and emission spectra were collected for the new phosphors. Strong absorption of the UV light and emission in the far-red region of the visible spectra were confirmed, which is in a good agreement with the literature. The Mn^{4+} doping level was optimized to achieve the highest luminescence in the studied phases. Temperature-dependent luminescence

spectra were collected for the $Na_2SrGe_6O_{14}$: Mn^{4+} and $K_2SrGe_8O_{18}$: Mn^{4+}, and the $K_2SrGe_8O_{18}$: Mn^{4+} showed the highest resistance to temperature quenching.

Acknowledgements

First and foremost, I thank my supervisor Dr. Yurij Mozharivskyj for the opportunity to join his group, to work on this project, and to gain an expertise in the field of solid-state chemistry. I am grateful to my committee members, Dr. Gillian Goward and Dr. John Greedan for the evaluation of my research progress and valuable advice which made this progress possible.

I thank my group member Dr. Timothy Lo for the provided trainings on the lab equipment and the software.

I thank my collaborators, Dr. W. Zhang, Dr. P. S. Halasyamani, S. Hariyani, Dr. J. Brgoch, Dr. V.V. Klepov and Dr. H.-C zur Loye for the provided measurements and calculations.

I also thank the Department of Chemistry and Chemical Biology staff members Dr. Jim Britten and Victoria Jarvis for the assistance with some XRD experiments.

I thank my friends and family.

Table of Contents

Chapter 1. Introduction 1

1.1 Luminescence 1

1.1.1 Luminescent materials 1

1.1.2 Excitation of an activator ion 4

1.1.3 Emission 9

1.1.4 Nonradiative return to the ground state 11

1.1.5 Energy transfer 13

1.2 Mn^{4+} as luminescent center in solids 17

1.2.1 Energy levels of free Mn^{4+} ion and Mn^{4+} in the crystal field 17

1.2.2 Nephelauxetic effect 22

1.2.3 Mn^{4+} phosphors for lighting 22

1.2.4 Germanates as host matrices for Mn^{4+} 24

1.2.5 Mn^{4+} phosphors, Eu^{3+} and Eu^{2+} phosphors 25

Chapter 2. Preparation and characterization methods for the new materials 29

2.1 Synthesis of the new materials 29

2.2 X-ray diffraction for the materials characterization 30

2.2.1 Generation of X-rays 31

2.2.2 X-ray tube emission spectrum 32

2.2.3 X-ray scattering 34

2.2.4 Reciprocal lattice. Ewald sphere 36

2.2.5 X-ray diffraction from a single crystal and a polycrystalline sample 38

2.2.6 Structure factor 39

2.2.7 Fourier transformation and phase problem 41

2.2.8 Single crystal X-ray diffraction 43

2.2.9 Powder X-ray diffraction 45

2.3 Neutron diffraction 47

2.4 Nuclear magnetic resonance 48

2.5 Optical properties measurements 50

Chapter 3. Two new magnesium and magnesium-lead fluorogermanates and revision of the $Mg_{28}Ge_{7.5}O_{38}F_{10}$ phase 52

3.1 Introduction 53

3.2 Experimental 55

3.2.1 Reagents 55

3.2.2 Synthesis 55

3.2.3 X-ray diffraction 56

3.2.4 Solid-state nuclear magnetic resonance (NMR) spectroscopy 57

3.2.5 Neutron powder diffraction and IR spectroscopy 57

3.3 Results and Discussion 58

3.3.1 Structure of $Mg_3Ge_{1-\delta}O_{4(1-\delta)}F_{2(1+2\delta)}$ (1) 58

3.3.2 Refinement of the twined $Mg_{14}Ge_4O_{20}F_4$ (2) crystal 61

3.3.3 Ge deficiency and environment in $Mg_3Ge_{1-\delta}O_{4(1-\delta)}F_{2(1+2\delta)}$ (1) and $Mg_{14}Ge_4O_{20}F_4$ (2) 62

3.3.4 NMR study of $Mg_3Ge_{1-\delta}O_{4(1-\delta)}F_{2(1+2\delta)}$ (1) 63

3.3.5 Neutron scattering study of MgF_2 and IR spectroscopy 64

3.3.6 Structure of $Mg_2Pb_2Ge_2O_7F_2$ (3) 65

3.3.7 High-temperature (HT) powder XRD 67

3.4 Conclusions 68

3.5 Supplementary information 69

Chapter 4. New halogen-germanates of Sr and Ba 71

4.1 Introduction 72

4.2 Experimental 74

4.2.1 Synthesis 74

4.2.2 Crystal structure determination 74

4.2.3 Powder x-ray diffraction 75

4.3 Results and Discussion 76

4.3.1 Crystal structures 76

4.3.2 Topology of R^{2+}- Hal (R^{2+} = Ca-Ba, Hal = F-Br) nets in halogen germanates 81

4.4 Conclusions 83

Chapter 5. Synthesis and structure of the Na-Ba and Rb-Ba octagermanates and phosphorescence of the $Rb_2BaGe_{8-x}O_{18}:xMn^{4+}$ series 85

5.1 Introduction 86

5.2 Experimental 88

5.2.1 Single crystal growth 88

5.2.2. Determination of crystal structure by X-ray diffraction 89

5.2.3 Preparation of the $Rb_2BaGe_8O_{18}$: Mn^{4+} phosphors 90

5.2.4 Phosphorescence measurements 91

5.3 Results and Discussion 91

5.3.1 Crystal structures of Na-Ba and Rb-Ba octagermanates 91

5.3.2 Photoluminescent properties of the $Rb_2BaGe_8O_{18}$: Mn^{4+} phosphors 95

5.4 Conclusion 97

5.5 Supplementary information 98

Chapter 6. Phosphorescence in Mn^{4+}-doped R^+ / R^{2+} germanates (R^+ = Na^+ or K^+, R^{2+} = Sr^{2+}) 100

6.1 Introduction 101

6.2 Experimental 103

6.2.1 Synthesis of the new phases as single crystals 102

6.2.2 Single crystal X-ray diffraction 104

6.2.3 Synthesis of the new germanate phosphors by solid-state reaction 106

6.2.4 Photoluminescence measurements 107

6.2.5 Second harmonic generation (SHG) measurements 107

6.2.6 Band gap calculations and experimental measurement 108

6.3 Results and Discussion 108

6.3.1 Crystal structure 108

6.3.2 Calculated and experimental band gap 114

6.3.3 Photoluminescent properties of the Pr^{3+} and Mn^{4+} activated germanates 115

6.3.4 Temperature-dependent phosphorescence in $Na_2SrGe_6O_{14}$ (2) and $K_2SrGe_8O_{18}$ (3) 120

6.4 Conclusion 122

6.5 Supplementary information 122

Chapter 7. Conclusions and future work 127

7.1 Magnesium fluorogermanates 128

7.2 R^{2+} halogen-germanates (R^{2+} = Sr^{2+} or Ba^{2+}) 128

7.3 New germanates with extended anionic frameworks 128

Appendix A1. Energy levels of octahedrally coordinated activator 130

Appendix A2. Na^{+} ionic conductivity in the $Na_{4-x}Sn_{2-x}Sb_xGe_5O_{16}$ series 131

A2.1 Introduction 132

A2.2 Methods 134

A2.2.1 Synthesis of the $Na_4Sn_2Ge_5O_{16}$ single crystals 134

A2.2.2 Single crystal XRD 134

A2.2.3 Synthesis of the $Na_{4-x}Sn_{2-x}Sb_xGe_5O_{16}$ series (x = 0, 0.05, 0.10, 0.15, 0.25, 0.30, 0.35) 135

A2.2.4 Powder XRD 135

A2.2.5 Calculations 135

A2.3 Results and Discussion 136

A2.3.1 Crystal structure 136

A2.3.2 Na^{+} ionic conductivity 138

A2.3.3 BVEL calculations 141

Appendix A3. Single exponential fit of the decays for the $Rb_2BaGe_{8-x}O_{18}$: xMn^{4+} phosphors 142

References 143

Lists of Figures

Number	Title	Page
1.1	Schematic representation of the direct activator ion (A) excitation in a host matrix	2
1.2	Schematic representation of Stokes shift: the absorption maxima correspond to blue light, while the emission one – to the red light	3
1.3	Configurational coordinate diagram. Zero-phonon line shown as blue arrow	5
1.4	Probability density functions for two vibrational levels v = 0 and v = 6 of the quantum harmonic oscillator	6
1.5	The origin of the absorption peak width from the configurational coordinate diagram consideration for two parabolas with a horizontal offset	7
1.6	The adsorption followed by radiative return to the ground state on the configurational coordinate diagram. The relaxation is shown by red arrows	9
1.7	Configurational coordinate diagram corresponding to the radiative (left) and nonradiative (right) return to the ground state. The nonradiative processes are indicated by green arrows	11
1.8	Schematic representation of the cross relaxation. The isolated center return to the ground state via emission (left). The cross relaxation between two centers quenches the emission (right)	17
1.9	Tanabe–Sugano diagram for the ion with d^3 electron configuration in the octahedral crystal field. Solid lines are for spin quartets, dashed – for spin doublets	19
1.10	(left) Configurational coordinate diagram for Mn^{4+}. The $^4A_2 \rightarrow {}^4T_2$ transition shown as blue arrow, $^4A_2 \rightarrow {}^4T_1(^4F)$ transition – as purple arrow, $^2E_2 \rightarrow {}^4A_2$ transition – as red arrow. The nonradiative processes shown as green arrows. (right) Excitation and emission data for the Mn^{4+} doped magnesium oxofluoride with peak assignment (data from M. G. Brik and A. M. Srivastava)	21
1.11	White light PC LED schemes: blue LED with yellow phosphor (left) and UV LED with RGB phosphors (right)	23
1.12	Energy levels of Eu^{3+} and Eu^{2+} in $Ca_3Y_2(SiO_4)_3$	27
2.1	Scheme of the laboratory X-ray tube. Be windows are shown in blue.	31
2.2	X-ray spectrum from a laboratory X-ray tube	33
2.3	X-ray scattering from an atom	34
2.4	Illustration of Bragg's law	35

2.5	Ewald sphere with r =1/λ, a crystal at the center and the corresponding reciprocal lattice with a* and b* lattice vectors. For all reciprocal lattice points indices *l* assumed to be 0 so only h and k are given for the clarity. Incident and diffracted beam vectors are connected by d^*_{230} if diffraction happens from 230 reciprocal point. $\overline{CA}$ is an altitude of a triangle formed by incident and diffracted beam vectors and d^*_{230} vector	37
2.6	Diffraction from a single crystal. At the given moment of time, Bragg's condition is satisfied for a few unequal d^*_{hkl} (d^*_{hkl}(1-3), shown in red, green, and blue respectively). On the detector three spots are expected plus an incident beam spot	38
2.7	Diffraction from a polycrystalline sample. Bragg's condition is satisfied for d^*_{hkl} simultaneously in an infinite number of grains generating a diffraction cone. The projection of the cone on the detector is a Debye ring. In a real sample Bragg's condition is satisfied for several d^*_{hkl} and thus a corresponding number of the concentric rings constitute the diffraction pattern	39
2.8	Vector representation of the structure amplitude F(h). Projection of F(h) on the real axis is A(h) (red), projection on the imaginary axis is B(h) (blue, shifted from the origin for clarity). In the acentric structure (*left*) B(h) ≠ 0, in the centrosymmetric structure (*right*) B(h) = 0. The α(h) angle is a "phase angle"	41
2.9	A single frame from the STOE IPDS II. The dark spots are the reflections, the big dark area in the middle is from a beam stop, preventing the detector damage	44
2.10	Coaxial diffraction cones from a polycrystalline sample	46
2.11	MAS solid state NMR scheme	49
2.12	Scheme of the UV-vis-NIR spectrometer (not to scale). The monochromator scheme is shown only for the excitation light for charity. Emission monochromator is operated on the same principles	51
3.1	(left) Ball and stick representation of the $Mg_3GeO_4F_2$ unit cell. (right) Infinite polyhedral layer parallel to the *ab* plane in $Mg_3GeO_4F_2$	59
3.2	The ^{19}F NMR spectral comparison of MgF_2 and the $Mg_3Ge_{1-\delta}O_{4(1-\delta)}F_{2(1+2\delta)}$ (**1**) sample, where * represents MAS spinning side bands	64
3.3	Polyhedral representation of the $Mg_2Pb_2Ge_2O_7F_2$ (**3**) structure (2×2×2 unit cells fragment) in two projections. Lead atoms are orange with bonds omitted for clarity	66
3.4	The diffraction data from the heating of Mg_2GeO_4 and MgF_2 in the 1:1 molar ratio on the Pt strip in air. The decomposition of MgF_2 and the	68

formation of MgO can be seen. The 25 °C measurement (top) was done after the system cooled down from 1200 °C

3.5 The Rietveld refinement of the MgF_2 neutron scattering data. R_p = 15.4 % 69

3.6 The IR spectra of MgF_2 (red) and the solid state reaction product (green). The product contains $Mg_3GeO_4F_2$ (89.9(7) wt. %), MgF_2 (6.4(1) wt. %) and $Mg_{14}Ge_4O_{20}F_4$ (4.6(1) wt. %). Absence of peaks in the characteristic region of the ν(H_2O) vibrations (at ~ 3615, 4350, and 1640 cm^{-1} for ν3, ν1, and ν2 respectively) indicates the absence of the OH^- group in the structure 69

4.1 Schematic representation of $Sr_3GeO_4Cl_2$ (**1**) framework formation: $(Sr2Cl)_\infty$ layers (top) are connected in 3D unit (middle) by GeO_4, and then the residual volume is filled by Sr1 (bottom). Hereinafter, alkaline earth atoms and their polyhedra are blue, Ge polyhedra are cyan, oxygen atoms are red, and halogen atoms are green 77

4.2 Schematic representation of the $Ba_3GeO_4Br_2$ (**2**) formation (*ab* projection): 2D and 1D Ba-Br units form a 3D framework, with further connections by GeO_4 tetrahedra 78

4.3 0D - 2D units Sr-Cl units forming a 3D framework in $Sr_6Ge_2O_7Cl_6$ (**3**). (bottom) The fragment (3×1×3 unit cells) of the $Sr_6Ge_2O_7Cl_6$ (**3**) crystal structure (*ab* projection) 79

4.4 1D and 3D Ba-Br units in $Ba_5GeO_4Br_6$ (**4**) 80

4.5 (left) Ba-Br framework in $Ba_5GeO_4Br_6$ (**4**). (right) $Ba_5GeO_4Br_6$ (**4**) structure (2×2×1 unit cells) projected on *ab* plane (right) 80

4.6 The transformation of two-, three-, and four coordinated Hal^- ligands in the topological analysis of R^{2+}- *Hal* nets 81

4.7 The topology of 2D R^{2+}-*Hal* nets in the halogen germanates 82

4.8 The topology of 3D R^{2+}-*Hal* nets in the $Ba_5GeO_4Br_6$ (**4**). Ba3 atoms are shown in dark blue. The bonds between *sra* and *lon nets* are omitted for clarity 83

5.1 (a), (b) A $Ge^oGe^t_{18}O_{54}$ cluster in the $Na_2BaGe_8O_{18}$ structure in two projections; (c) the $Na_2BaGe_8O_{18}$ unit cell viewed along the *c* direction. GeO_4 polyhedra are cyan, GeO_6 polyhedra are green, Na atoms are yellow, Ba atoms are green, O atoms are red. Na–O and Ba–O bonds are omitted for clarity 92

5.2 (a), (b) A $Ge^oGe^t_{36}O_{108}$ cluster in the $Li_3RbGe_8O_{18}$ structure in two projections; (c) the $Li_3RbGe_8O_{18}$ unit cell viewed along the *c* direction. GeO_4 polyhedra are cyan, GeO_6 polyhedra are green, Rb and Li atoms are yellow, O atoms are red. Li–O and Rb–O bonds are omitted for clarity 94

5.3 The underlying nets of the anionic frameworks in germanates (projections on the *ab* plane): (a) *cat* net in $Na_2Ge_4O_9$; (b) *ben* net in $BaGe_4O_9$; (c) *fsb* net in $Li_3RbGe_8O_{18}$; (d) a new net in $Na_2BaGe_8O_{18}$ and $Rb_2BaGe_8O_{18}$ 95

5.4 (a) PL and PLE spectra of the $Rb_2BaGe_{7.995}O_{18} : 0.005Mn^{4+}$ sample at room temperature; (b) PLE spectra of the $Rb_2BaGe_{8-x}O_{18} : xMn^{4+}$ samples 97

5.5 Rietveld refinement for the unsuccessful $Rb_2BaGe_8O_{18}$ synthesis directly from carbonates 99

6.1 A view of the $Na_{0.36}Sr_{0.82}Ge_4O_9$ (**1**) structure fragment along the *c* direction. Hereinafter, GeO_6 octahedra are green, GeO_4 tetrahedra are cyan, oxygen atoms are red. Na^+ and Sr^{2+} cations are gray (with □ representing the deficiency) 109

6.2 The comparison between GeO_n (n = 4 and 6) polyhedra connectivity in $Na_{0.36}Sr_{0.82}Ge_4O_9$ (**1**) and $SrGe_4O_9$. Oxygen atoms are omitted 110

6.3 GeO_n polyhedra connectivity in $Na_2SrGe_6O_{14}$ (**2**) and a fragment of the $Na_2SrGe_6O_{14}$ (**2**) structure in two projections 112

6.4 The fragment of the $K_2SrGe_8O_{18}$ (**3**) structure in two projections. K atoms are yellow, Sr – gray 113

6.5 Density of states of $Na_2SrGe_6O_{14}$(a) and $K_2SrGe_8O_{18}$ (b) 114

6.6 The F(R) versus energy (in eV) plot for the pristine $Na_2SrGe_6O_{14}$ (a) and $K_2SrGe_8O_{18}$ (b) phases. The corresponding optical band gap values are given on the plot 115

6.7 PLE and PL spectra of the $Na_2Sr_{0.994}Ge_6O_{14} : 0.006\ Pr^{3+}$ sample at room temperature 116

6.8 PLE and PL spectra of the $Na_2SrGe_{5.998}O_{14} : 0.002\ Mn^{4+}$ sample (a) and the PLE spectra of the $Na_2SrGe_{6-x}O_{14} : xMn^{4+}$ series (x = 0.002, 0.008, and 0.016) (b) 117

6.9 PLE and PL spectra of the $K_2SrGe_{7.995}O_{18} : 0.005\ Mn^{4+}$ sample (a) and the emission spectra of $K_2SrGe_{8-x}O_{18} : xMn^{4+}$ (x = 0.003, 0.005, 0.016, and 0.032) (b) 118

6.10 Contour plot of the temperature dependent PL spectra for $K_2SrGe_{7.995}O_{18} : 0.005Mn^{4+}$ (a) and the normalized integrated intensity of its emission as a function of temperature (b) 121

6.11 Rietveld refinement of the $Na_2SrGe_{5.992}O_{14} : 0.008Mn^{4+}$ sample 122

6.12 Rietveld refinement of the $K_2SrGe_{7.995}O_{18} : 0.005Mn^{4+}$ sample 123

6.13 DTA curve (heating) for the $SrGe_4O_9$ phase. Sample starts melting at 1142 °C. There is no indication of phase transitions prior the melting point 123

6.14 Experimental data and the Le Bail simulation (*R*32 and *C*2 space groups) for $Na_{0.36}Sr_{0.82}Ge_4O_9$ 124

6.15 Fragment of the Figure S1 at 50–80° 2Θ range. The features of experimental peaks (black) matching the *R*32 Le Bail model (red), but not the *C*2 model (blue) 124

6.16 Temperature dependent emission spectra of $Na_2SrGe_{5.992}O_{14}$: $0.008Mn^{4+}$ sample in the 100-500 K range 125

6.17 Temperature dependent emission spectra of the $K_2SrGe_{7.995}O_{18}$: $0.005Mn^{4+}$ sample in two temperature regions (for clarity): 77-300 K (a) and 320-520 K (b) 124

6.18 Normalized temperature dependent emission spectra of the $K_2SrGe_{7.995}O_{18}$: $0.005Mn^{4+}$ sample in 77-520 K range 126

6.19 Linear fitting of the $\ln(I_0/I_T\text{-}1)$ versus 1/kT data for the $K_2SrGe_{7.995}O_{18}$: $0.005Mn^{4+}$ sample 126

A1.1 The energy levels of the octahedrally coordinated activator A in terms of the molecular orbital theory. The “ligand-to-metal” charge transfer transition is shown by red arrows. 130

A2.1 (top left) $Ge_5O_{16}^{12-}$ polyanions stacking in the $Na_4Sn_2Ge_5O_{16}$ structure; (top right) anionic framework built on GeO_4 and SnO_6 units in the $Na_4Sn_2Ge_5O_{16}$ structure; (bottom center) Na^+ cations in the channels of the anionic framework 137

A2.2 SnO_6 and TO_4 (T = Si or Ge) polyhedra connection in the $Na_4Sn_2Si_5O_{16}\cdot H_2O$ (left) and $Na_4Sn_2Ge_5O_{16}$ (right) structures. One SnT_2O_3 cycle forms in silicate, while two cycles form in the germanate. 138

A2.3 (a) EIS spectrum (black circles) and corresponding equivalent circuit model fit (red line) of the undoped $Na_4Sn_2Ge_5O_{16}$ phase. The EIS spectrum of the doped $Na_{3.8}Sn_{1.8}Sb_{0.2}Ge_5O_{16}$ phase is included or comparison (blue circles). (b) EIS spectrum of the $Na_{3.8}Sn_{1.8}Sb_{0.2}Ge_5O_{16}$, zoomed into the high frequency region (blue circles). As well as the corresponding equivalent circuit model fit (black line). (c) Ionic conductivity values of each $Na_{4-x}Sn_{2-x}Sb_xGe_5O_{16}$ phase. 139

A2.4 Temperature dependent ionic conductivity measurements of $Na_4Sn_2Ge_5O_{16}$ (black) and $Na_{3.8}Sn_{1.8}Sb_{0.2}Ge_5O_{16}$ (blue), with the corresponding activation energies obtained from the slope. 140

A2.5 (top) Na^+ conduction pathways in the $Na_4Sn_2Ge_5O_{16}$ unit cell viewed on *ac* plane; (bottom) 2D Na^+ conduction pathways in the $Na_4Sn_2Ge_5O_{16}$ unit cell with atoms omitted for clarity. 141

A3.1 Single exponential fit of the luminescence decay curves for the $Rb_2BaGe_{8-x}O_{18}$: xMn^{4+} phosphors (x = 0.001, 0.003, 0.005, and 0.010). 142

List of tables

Number	Title	Page
1.1	The mathematical relationship between Racah parameters and electrostatic terms energy in the ions with d^3 electron configuration. The ground term energy taken as 0	18
2.1	Characteristic wavelength of Cu and Mo anodes	34
3.1	Selected crystallographic data and parameters of XRD experiments for structures 1-3	60
3.2	Fractional atomic coordinates and equivalent isotropic displacement parameters for $Mg_3Ge_{1-\delta}O_{4(1-\delta)}F_{2(1+2\delta)}$ prepared by the solid state route. U_{eq} is defined as 1/3 of the trace of the orthogonalised U_{ij} tensor. The O and F sites were assumed to be occupied only by O and F atoms, respectively	70
3.3	Interatomic distances for the Ge3 surrounding in $Mg_{14}Ge_4O_{20}F_4$	70
3.4	Bond lengths for $Mg_2Pb_2Ge_2O_7F_2$	70
4.1	Selected crystallographic data and parameters of XRD experiments for $Sr_3GeO_4Cl_2$ (**1**), $Ba_3GeO_4Br_2$ (**2**), $Sr_6Ge_2O_7Cl_6$ (**3**), and $Ba_5GeO_4Br_6$ (**4**)	75
5.1	Selected crystallographic data and refinement results for $Na_2BaGe_8O_{18}$ (**1**) and $Rb_2BaGe_8O_{18}$ (**2**)	89
5.2	Two examples of the $Rb_2BaGe_8O_{18}$ synthesis attempts from Rb_2CO_3, $BaCO_3$ and GeO_2	98
6.1	Selected crystallographic data and refinement results for **1-3**	105
6.2	PLE and PL parameters of the Mn^{4+} doped $Na_2SrGe_6O_{14}$ (**2**) and $K_2SrGe_8O_{18}$ (**3**) samples	119
A2.1.	Selected crystallographic data and refinement results for $Na_4Sn_2Ge_5O_{16}$	136

List of all Abbreviations and Symbols

Abbreviation	Meaning
calc	Calculated
HV	High voltage
ICSD	Inorganic Crystal Structure Database
LED	light emitting diode
MAS	Magic angle spinning
NIR	Near infra-red
NMR	Nuclear magnetic resonance
obs	Observed
PC LED	phosphor-converted LED
PL	Photoluminescence emission
PLE	Photoluminescence excitation
RGB	Red-green-blue
UV	Ultraviolet
vis	Visible
XRD	X-ray diffraction

Symbol	Meaning
a, b, c	Unit cell parameters
α, β, γ	
V	Unit cell volume
d^*_{hkl}	Reciprocal lattice vector
D_{calcd}	Calculated density
F(000)	Structure factor for h=k=l=0
F(h)	Structure amplitude
hkl	Miller indices
I	Intensity
λ	Wavelength
μ	X-ray linear absorption coefficient
ρ(x)	Electron density
θ	Bragg angle

Declaration of Academic Achievement

Papers in peer-reviewed journals

(1) **Novikov, S. A**.; Lu, Y.; Zhang, W.; Halasyamani, P. S.; Hariyani, S.; Brgoch, J.; Klepov, V. V.; zur Loye, H.-C.; Mozharivskyj, Y. Phosphorescence in Mn^{4+}-doped R^{+}/R^{2+} germanates (R+ = Na^{+} or K^{+}, R^{2+} = Sr^{2+}). *Inorg. Chem.* **2022**, 61 (24), 9364–9374.

(2) **Novikov, S**.; Bagum, R.; Yan, Z. B.; Clancy, J. P.; Mozharivskyj, Y. Two New magnesium and magnesium-lead fluorogermanates and revision of the $Mg_{28}Ge_{7.5}O_{38}F_{10}$ phase. *Journal of Solid State Chemistry* **2021**, 293, 121741.

(3) **Novikov, S. A.;** Mozharivskyj, Y. Synthesis and Structure of the Na–Ba and Rb–Ba Octagermanates and Phosphorescence of the $Rb_2BaGe_{8-x}O_{18}$:xMn^{4+} Series. *Journal of Solid State Chemistry* **2021**, 304, 122607

(4) **Novikov, S**.; Mozharivskyj, Y. New Halogen Germanates of Sr and Ba. *Journal of Solid State Chemistry* **2020**, 282, 121075.

(5) Shadap, L.; Tyagi, J. L.; Poluri, K. M.; **Novikov, S**.; Lo, C.-W. T.; Mozharivskyj, Y.; Kollipara, M. R. Synthesis and Biological Evaluation of Some New Class of Benzothiazole–Pyrazole Ligands Containing Arene Ruthenium, Rhodium and Iridium Complexes. *Transit Met Chem* **2021**, 46 (3), 231–240

(6) Shadap, L.; Tyagi, J. L.; Poluri, K. M.; **Novikov, S**.; Timothy Lo, C.-W.; Mozharivskyj, Y.; Kollipara, M. R. Insights to the Strained Thiocarbamate Derivative Complexes of Platinum Group Metals Induced by Azide as a Co-Ligand: Characterization and Biological Studies. *Journal of Organometallic Chemistry* **2020**, 920, 121345.

“Ut desint vires, tamen est laudanda voluntas.”

Ovidius, Epistulae ex Ponto, III, 4, 79.

Chapter 1. Introduction

1.1 Luminescence

In the literature on the photoluminescence two terms, “phosphorescence” and “fluorescence”, appear very often. The “fluorescence” is associated with fast spin-allowed ($\Delta S=0$) electronic transitions in the materials, while the slow spin-forbidden transitions account for the “phosphorescence”. On the other hand, the spin-selection rule is not the single one governing the rate of the electronic transitions in the phosphors: parity selection rule account for the slow rates of some transitions in the rare-earth cations. To avoid the use of additional terms, the general term “luminescence” will be used in this chapter to describe the phenomenon of the luminescent materials glowing after the excitation.

1.1.1 Luminescent materials

Luminescence is the ability of a material to convert certain types of energy into electromagnetic radiation above the thermal radiation.[1] This definition distinguishes luminescence from the thermal radiation of hot solids. Additionally, in contrast to light reflection, dispersion of light, and Cherenkov radiation the luminescence does not quench immediately in the absence of the excitation. Materials capable of luminescence are known as phosphors.

The valuable and intriguing property of luminescence is the ability to give us an insight into energies sometimes invisible by a naked eye through the conversion of those energies into visible light. For example, photoluminescence is caused by light (for example UV), cathodoluminescence – by the energy of electron beams (cathode rays), electroluminescence – by voltage, X-ray luminescence – by X-rays, chemiluminescence – by the energy of a chemical reaction. Depending on the type of luminescence, various materials are used as phosphors.

Common photoluminescent materials are electrical insulators containing a small level of the impurity ions in their structures. The impurity ions accounting for the luminescence are known as 'activator' ions and are embedded into the 'host matrix', i.e. into the structure of a pristine material (Figure 1.1).

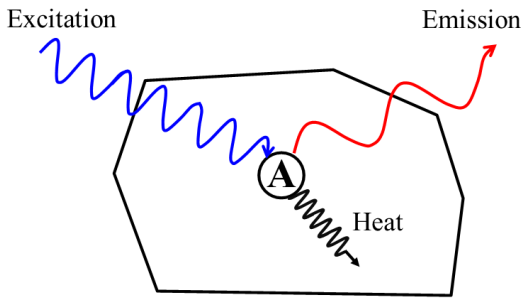

Figure 1.1. Schematic representation of the direct activator ion (A) excitation in the host matrix.

In a phosphor, the excitation radiation causes the transition from the ground state to one of the excited states in an activator ion. Return to the ground state occurs through the emission of light (luminescence) from an activator. The luminescence involves a series of relaxation processes accounting for the Stokes shift – an energy difference between the excitation (absorption) and emission bands originating from the same electronic transition. The excitation radiation typically undergoes a down-conversion in a phosphor material (Figure 1.2). The return to the ground state can be nonradiative with the energy of the excited state dissipated by heating a host lattice. The radiative and nonradiative relaxations are in competition, so the latter one should be suppressed in favor of the radiative one to achieve a high-efficiency phosphor.

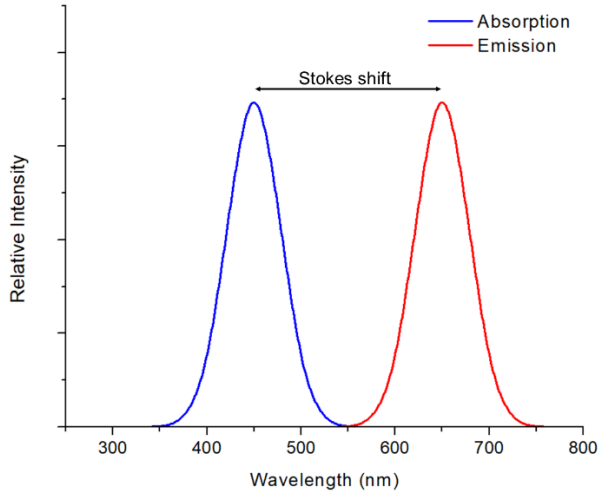

Figure 1.2. Schematic representation of Stokes shift: the absorption maximum corresponds to blue light, while the emission one – to the red light.

The excitation does not necessary happen only within an activator ion. The incoming radiation can be absorbed by another ion of the host lattice. This excited ion would return to the ground state through the transfer of energy to an activator. Such ion is referred as a sensitizer (S). The host lattice itself can act as sensitizer and thus transfer the energy to activator ions. The schematic process of energy transfer from sensitizer to an activator is shown below:

$S + h\nu \rightarrow S^*$ (sensitizer excitation)

$S^* \rightarrow S + h\nu$ or $S^* + A \rightarrow S + A^*$ (sensitizer relaxation via luminescence or energy transfer to an activator)

$A^* \rightarrow A + h\nu$ (activator relaxation).

Thus, the luminescence process starts with an absorption of energy (excitation). The relaxation from an excited state to the ground state is possible through the emission of light or through the nonradiative return. The energy transfer between activators or sensitizer (including

host lattice) and activator may occur. These processes are discussed in more details in the following sections.

1.1.2 Excitation of an activator ion

In photoluminescent materials, the excitation radiation is UV or visible light, and the absorption happens within an activator ion. An absorption peak has some intensity and width. Intensity is associated with a probability of the specific electronic transitions. The width of an absorption peak can be explained using the configurational coordinate model.

In the host lattice, an activator and its surroundings participate in lattice vibrations. The vibration of the surroundings causes a change in the electronic states of an activator and vice versa. In the configurational coordinate model, electrons are assumed to move in the static nucleus surrounding (adiabatic approximation). The second assumption is that the only vibrational mode under consideration is a fully symmetrical stretching, in which an activator remains at rest, while surrounding atoms (ligands) move in phase toward and away from the center. In this case only one nuclear coordinate, known as configurational coordinate, is needed. This coordinate corresponds to the interatomic distance between the luminescence center and ligands. A configuration coordinate energy diagram provides a graphical interpretation of the model.[2] On the diagram, the energies of the ground and excited states of an activator are plotted as functions of the configurational coordinate (interatomic distance, R). A configurational coordinate diagram in Figure 1.3 includes two parabolas, corresponding to the ground state (lower one) and an excited state (upper one). The parabolic shape of the potential energy curves comes from the harmonic oscillator approximation. In this approximation, the restoring force F is a proportional to the displacement and for the ground state $F = -k(R - R_0)$. The potential energy depends on R as:

$E = \frac{1}{2}k(R - R_0)^2$, thus, the shape of a E vs R curve is parabolic. R_0 is an equilibrium distance and correspond to the minimum energy in the ground state. Discrete energy levels marked in Figure 1.3 as v = 0, v =1, etc. and depicted as horizontal lines correspond to the quantized energy levels of the harmonic oscillator. The permitted phonon energy of the oscillator depends on the vibrational frequency υ as $E = \left(v + \frac{1}{2}\right)h\nu$, where v = 0, 1, 2, etc. For v = 0 (lowest vibrational level), the highest probability of finding the system is at R_0, while for higher values of v, the highest probability is at turning points (edges of parabola, Figure 1.4). The ground state and an excited state have different values of the equilibrium distance R_0' and force constant k'. This arises from differences in the chemical bonding between the ground and excited states. The difference in the equilibrium distances ΔR (i.e., horizontal offset of parabolas) is shown in Figure 1.3.

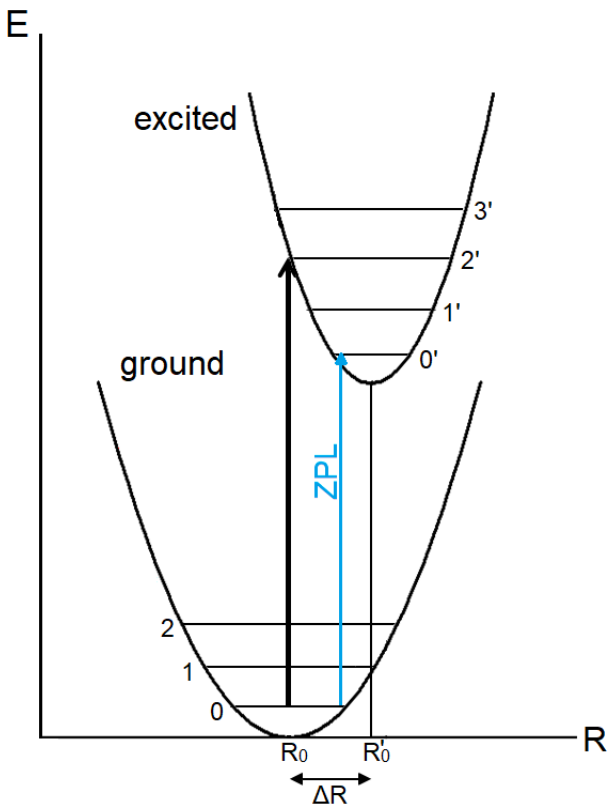

Figure 1.3. Configurational coordinate diagram. Zero-phonon line shown as blue arrow.

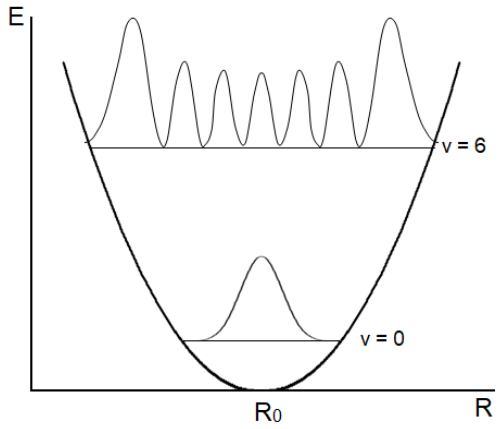

Figure 1.4. Probability density functions for two vibrational levels v = 0 and v = 6 of the quantum harmonic oscillator.

In the configurational coordinate diagram, the horizontal displacement corresponds to the change of the internuclear distances R due to the vibrations. Transitions between two parabolas are electronic transitions (shown with a black vertical arrow in Figure 1.3). Vertical transition happens without changes in the configurational coordinate and depicts the static surrounding of an electron during the transition (Franck–Condon principle).

Since the vibrational wavefunction has the maxima at R_0 for the lowest vibrational states and at the edges of parabola for the higher states (Figure 1.4), the most probable optical absorption transition starts at the lowest vibrational level v = 0, R = R_0 of the ground state and ends at the edge of the excited state parabola. This transition corresponds to the absorption band maximum. Transitions starting away from R_0 are less probable, but still possible. Such transitions account for the width of the absorption peak: for R > R_0, the energy difference between the lowest vibrational level of the ground state and higher vibrational levels of the excited state is less, while for R < R_0, the energy difference is more, compared to R = R_0 (Figure 1.5). For the case of a zero offset ($\Delta R = 0$) the most probable transition is from v = 0 of the ground state to v' = 0 of the excited state. The

absorption spectra corresponding to that transition consist of a single line, known as zero-phonon line (ZPL).

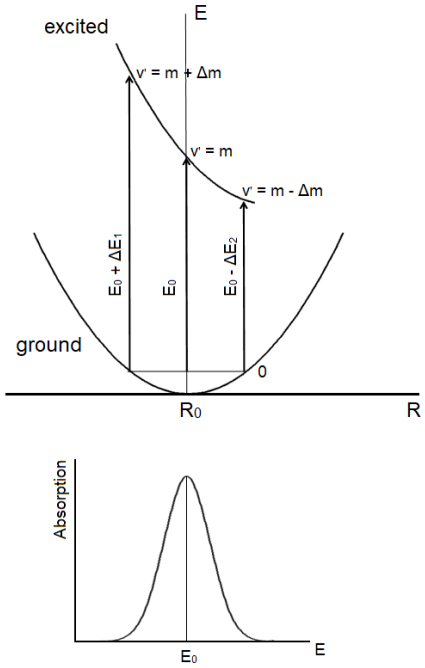

Figure 1.5. The origin of the absorption peak width from the configurational coordinate diagram consideration for two parabolas with a horizontal offset.

The vertical transition ends up away from the R_0' of the excited state. The large parabolas offset accounts for the broad absorption peaks. The large offset also means that there is a significant difference in chemical bonding between the ground and the excited states. The value of ΔR is a measure of the interaction between the electrons and the vibrations of the optically active center. This interaction is referred to as "coupling" and the $\Delta R = 0$ case corresponds to a weak-coupling scheme (weak interaction), while the $\Delta R \gg 0$ case to a strong-coupling scheme (strong interaction). The increase of ΔR reflects on the absorption spectra as follows: for weak coupling, a strong zero-phonon line is observed in the absorption spectra (with some side bands

due to the coupling to the vibrational states), while for the strong coupling, the zero-phonon line vanishes and the absorption spectra consist of a very broad peak.

The intensity of an optical absorption transition from the ground to the excited state is attributed to the electronic states. The selection rules dictate what transitions are allowed. The spin selection rule forbids the transitions between levels with different spin states ($\Delta S \neq 0$). The parity selection rule ($\Delta l \neq \pm 1$) forbids electronic transition between levels with the same parity, such as transitions within the *d* shell, *f* shell ($\Delta l = 0$) or between *d* and *s* shells ($\Delta l = 2$). In the solid state, the selection rules are relaxed by various phenomena (spin-orbital coupling, electron-vibration coupling etc.) making possible some of the formally forbidden transitions.

An activator ion spectral features depend on the host lattice. Different host lattices are characterized by different covalency of the activator surroundings. The interactions between the electrons decrease in more covalent surroundings compared to the more ionic ones. The reduced interaction shifts the electronic transitions to the lower energy. This means that experimentally observed absorption peaks for the same activator would shift to the longer wavelength in a sulfide matrix compared to an oxide one, or in an oxide when compared to a more ionic fluoride surroundings. The influence of the covalency is known as the nephelauxetic effect.[3]

Even within the same chemical surroundings, the absorption properties of an activator vary between compounds (for example between oxides). Phosphors are prepared by doping of an activator into the host matrix. Depending on the host lattice, an activator will experience different crystal field strengths. The influence of a crystal field is especially pronounced for the transition metals as discussed below in 1.2.1.

1.1.3 Emission

To illustrate the radiative return of the activator to the ground state (i.e. emission) we refer again refer to the configurational coordinate diagram (Figure 1.6). For the case with an offset in the parabolas, after the excitation the activator center is in a higher vibrational level (v' > 0). By releasing part of the energy to the surrounding (relaxation process, shown with red arrow in Figure 1.6), the center returns to the lowest vibrational state (v' = 0) of the excited state. Almost no emission happens during the relaxation due to much faster vibrational rates compared to the emission rates. The return from the excited state to the ground state is possible through the emission of radiation. Unlike the absorption, the emission process is spontaneous meaning no external radiation is involved.

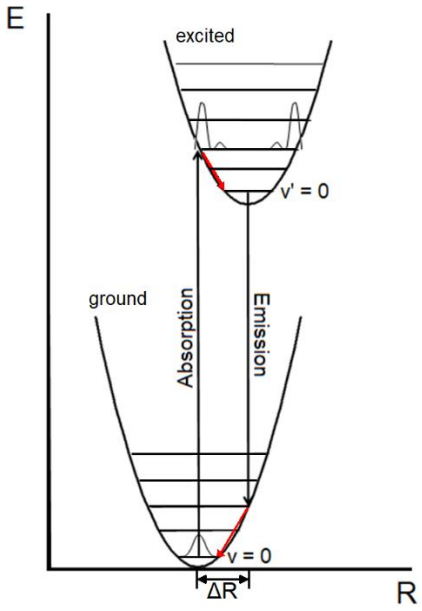

Figure 1.6. The adsorption followed by radiative return to the ground state on the configurational coordinate diagram. The relaxation is shown by red arrows.

The emission brings the center to a higher vibrational level of the ground state from where further relaxation to the v = 0 and R = R_0 state occurs. As mentioned earlier, the relaxation processes accounts for the Stokes shift. These shifts are observed experimentally and used to infer the difference in the electron-vibration coupling in the ground and the excited states. In order to do so, the Stokes shift should be expressed in the terms of the parabolas displacement, ΔR (page 7). In the literature, two relations are the most common: $E_{Stokes} = (2S - 1)\hbar\omega$ and $E_{Stokes} = 2S\hbar\omega$, where S is the dimensionless Huang-Rhys parameter[2,4] proportional to ΔR^2. Thus, S relates the Stokes shift and the change in the bonding between the ground and the excited states.

Additional factors influencing the emission spectra are the coupling with vibrational modes and the influence of a host lattice. For luminescent centers with weak electron-lattice coupling, the zero-phonon line would dominate in the emission spectra. In case of moderate coupling, zero-phonon line intensity is significantly reduced, and the emission consists of equidistant lines (the distance corresponds to some vibrational mode frequency). For centers with strong coupling the emission spectra are not informative and consist of a broad band, and the zero-phonon line can be hard to distinguish.

The influence of a host lattice on the emission is associated with the stiffness of the luminescent center surrounding. Stiff surrounding limits the values of S and ΔR (thus decreasing Stokes shift) so the vibrational structure may appear in some cases. The nephelauxetic effect and crystal field also influence the emission spectra, and they will be discussed in 1.2.2 for the Mn^{4+} activator.

The crucial property of an emission is the lifetime of the excited state. If we have a system with two states, ground and excited, the population of the excited state decreases as:

$$\frac{dN_e}{dt} = -N_e P_{eg} \quad (1.1),$$

where N_e is a number of luminescence centers in the excited state after an excitation pulse, t is the time, P_{eg} – a probability of the spontaneous emission. Integration of (1) gives

$$N_e(t) = N_e(0)e^{-P_{eg}t} \quad (1.2)$$

or

$$N_e(t) = N_e(0)e^{-t/\tau_R} \quad (1.3),$$

where $\tau_R=(P_{eg})^{-1}$ is a radiative decay time. The logarithm of intensity decays linearly with time.

1.1.4 Nonradiative return to the ground state

Emission of radiation is not the only way for a system to return to the ground state. The competing nonradiative return is also possible. In Figure 1.7, two configurational coordinate diagrams for the strong electron-lattice coupling scheme are shown. Unlike the previously shown diagrams, here a crossover point exists between the ground and the excited state parabolas (marked as X).

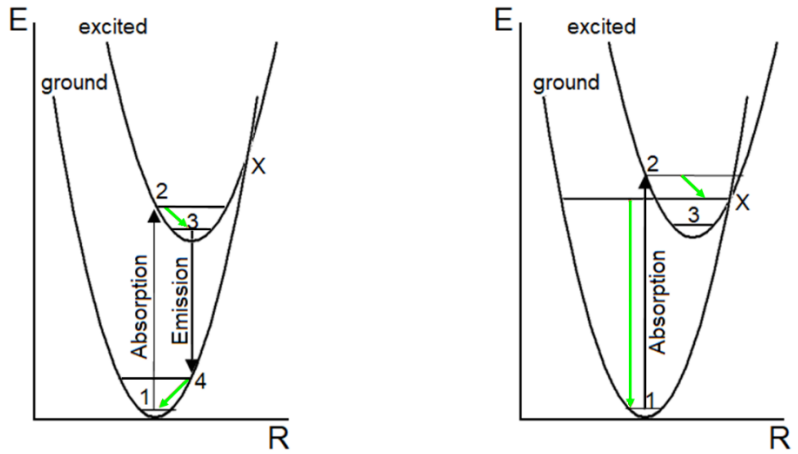

Figure 1.7. Configurational coordinate diagram corresponding to the radiative (left) and nonradiative (right) return to the ground state. The nonradiative processes are indicated by green arrows.

In the left diagram, the absorption starts from the lowest vibrational level of the ground state (point 1 in the Figure 1.7) and ends in the higher vibrational level of the excited state (point 2). This transition corresponds to the maximum overlap of the vibrational wavefunctions (see Figure 1.4). Note, that point 2 lies below the crossover point X. The fast relaxation brings the system to the lowest vibrational state (point 3) from which the emission occurs. After the emission of light, the system relaxes from the non-zero vibrational level of the ground state (point 4) back to the starting point.

The right diagram in Figure 1.7 describes a luminescent center with a higher Huang-Rhys constant, so the crossover point X now appears lower than point 2. After the excitation, the luminescent center relaxes to the vibrational state corresponding to the crossover point. The level at the crossover of the ground and the excited state parabolas is degenerate in energy. From this vibrational level the nonradiative relaxation is much more likely through the phonon states of the ground state parabola rather than through the excited state one. Level marked as 3 remains unpopulated and further return to the ground state via emission is not possible. Instead of the emission, the system undergoes a full nonradiative relaxation within the ground state parabola[5].

The configurational coordinate diagrams above can qualitatively explain the thermal quenching of luminescence – a phenomenon of decreasing and complete cease of luminescence in a phosphor at elevated temperatures. At higher temperatures, the higher vibrational levels are thermally populated. This means the level corresponding to the crossover becomes populated too. The system returns to the ground state via nonradiative decay, and luminescence is not observed.

The diagrams in Figure 1.7 correspond to the strong coupling scheme. For the weak coupling scheme ($S \approx 0$) there is no crossover points for two parabolas, so that nonradiative return to the ground state described above is not feasible. Alternatively, the processes known as

multiphonon emission and cross-relaxation happen for such luminescent centers. The multiphonon emission is possible if the energy difference between ground and exited states is equal to or less than 4-5 times the higher vibrational frequencies of the center surroundings. The energy is spent to excite the high-energy vibrations rather than being used in the emission process. The multiphonon relaxation does not depend on the concentration of the luminescent centers. The cross-relaxation relates to the energy transfer between two centers and discussed in the next chapter.

1.1.5 Energy transfer

The luminescent center can return to the ground state via emission or via nonradiative processes, as discussed in the previous sections. There is however also a probability of the return to the ground state via energy transfer to another luminescent center. A schematic representation of the process is S* + A → S + A* (asterisk for excited state). If the energy transfer is followed by the emission from A, S is referred as a sensitizer for emission by A. In many cases however, the A center return to the ground state non-radiatively, thus A acts as a quencher of the emission by S. Energy transfer is possible between different luminescent centers (two dopants in one matrix) as well as between the identical centers.

For two centers, S and A, located in the host matrix at some distance R, energy transfer is possible if there is some interaction mechanism between these centers. The interaction includes exchange interaction or an electrical or magnetic multipolar interaction. The probability of the energy transfer from S to A is[6,7]:

$$P_t = \frac{2\pi}{\hbar} \left| \langle \psi_S \psi_{A^*} \left| H_{int} \right| \psi_{S^*} \psi_A \rangle \right|^2 \int g_S(E) g_A(E) dE \qquad (1.4),$$

where ψ_S and ψ_{S^*} denote the wavefunctions of the ground and excited states of the S center respectively, ψ_A and ψ_{A^*} – wavefunctions of the A center, H_{int} is the interaction Hamiltonian for the initial and final states, $|\psi_S\psi_{A^*}\rangle$ and $|\psi_{S^*}\psi_A\rangle$ respectively. The integral in the equation (1.4) represents the spectral overlap between the normalized optical line shape functions of the luminescent centers, $g_X(E)$ ($g_S(E)$ – normalized emission line shape function for S, $g_A(E)$ – normalized absorption line shape function for A). This term is at maximum when the energy differences between the ground and excited states for S and A are the same (resonance conditions). This is known as resonant energy transfer. The unlike luminescent centers usually have energy mismatch[5]. In this situation, the energy transfer is assisted by lattice phonons of the appropriate energy compensating the energy difference between the energy levels of S and A. This is known as phonon-assisted energy transfer and electron-phonon coupling should be considered along with the interaction mechanism allowing the energy transfer.

The interaction Hamiltonian in eq. (1.4) may involve quantum mechanical exchange interaction or multipolar (electric and magnetic) interactions. The dominant interaction is determined by the spatial separation between the S and A centers and the nature of their wavefunctions.

For the electric multipolar interactions, the rate of the energy transfer varies with the distance R as $1/R^n$, n = 6, 8, 10 for electric dipole-dipole, dipole-quadrupole, quadrupole-quadrupole interactions. Exchange interaction depend on the distance exponentially. Conditions for the high rate of the energy transfer (high P_{SA}) are:

1) considerable level of resonance, meaning the spectral overlap of the S emission and A absorption bands;

2) considerable interaction, either exchange or multipolar. High transfer rates are anticipated if the involved optical transitions are allowed electric dipole transitions for both S and A centers. The rates due to the exchange interactions depend only on the wavefunctions overlap, but not on the optical transition nature. Generally, for the electrical dipole-dipole allowed optical transitions with a considerable spectral overlap the energy transfer is possible at the distances ≈ 30 Å. The exchange interactions are possible only between the closest neighbors at 5-8 Å range.

For the energy transfer between identical luminescent centers, the same considerations should be used. In case of a weak coupling (rare earth ions), the interactions between ions are very weak since the 4f electrons are shielded. On the other hand, the spectral overlaps are large since the absorption and emission lines coincide. The transfer rate surpasses the radiative rate because the emission represents the forbidden electronic transition.

Energy transfer can be studied with luminescent decay curves. For the case of the isolated center S with no energy transfer, the intensity decays exponentially with time:

$$I = I_0 e^{-\gamma t} \qquad (1.5),`$$

where I_0 is the intensity at time t = 0 and γ is the radiative rate. The deviation from the exponential law is an evidence of energy transfer. The decay rates for the SA transfer only as well as simultaneous SA and SS transfers can be found in the literature.[1]

For the intermediate coupling scheme due to the larger Stokes shift of the emission, the spectral overlap of the emission and absorption is very small or even nonexistent. In this case we expect no energy transfer between the same luminescent centers at low temperatures. At higher temperatures however with higher vibrational states being populated, the spectral bands broaden and thus the overlap increases. The increased overlap makes a thermally stimulated transfer possible.

Energy transfer accounts for the concentration quenching of luminescence, a phenomenon of a decreasing luminescence efficiency after some critical concentration of an activator is reached. This is associated with efficient energy transfer between luminescent centers at higher concentration when the spatial separation of the centers is reduced. Two mechanisms of the concentration quenching are used for the explanation of the phenomenon:

1) the efficient energy transfer is not limited to the pair of neighboring centers. The excitation energy can be transferred to some impurity ions or defects of the lattice which return to their ground state via nonradiative processes. These ions and defect are referred as killers or quenching traps;

2) the cross-relaxation mechanism. Here two centers are required, and the excitation energy is transferred partially from one center, acting as donor to another, acting as acceptor. The resonant energy transfer between two centers occurs due to the specific energy-level scheme. The illustration is shown in Figure 1.8. In the absence of energy transfer the center return to the ground radiatively (E3→E0 emission). If the energy difference between levels 0 and 1 is the same as for 2 and 3, the resonant energy transfer brings the excited center from 3 to 2, while the neighboring center goes up in energy from 0 to 1 (Figure 1.8). Because of this relaxation this state, the E3→E2 emission is quenched.

Generally, the concentration quenching is detected clearly with the luminescence decay time rather than with quantum efficiency. At certain critical concentration the luminescence lifetime is reduced indicating the concentration quenching.

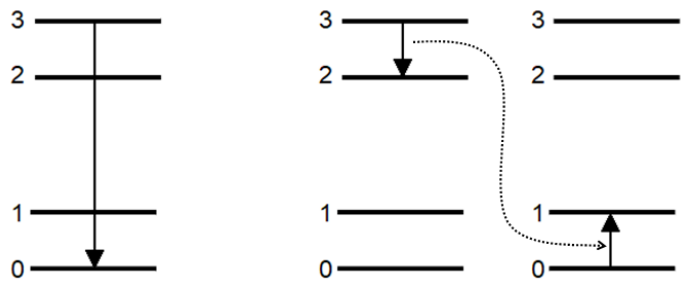

Figure 1.8. Schematic representation of the cross relaxation. The isolated center return to the ground state via emission (left). The cross relaxation between two centers quenches the emission (right).

1.2 Mn^{4+} as luminescent center in solids

In this section the photoluminescent properties of tetravalent manganese are discussed. The energy diagram of a free ion and an ion in the crystal field will be used to explain the absorption and emission spectra of Mn^{4+}. Influence of the host lattice on the peak positions, possible applications, and a brief comparison to the Eu^{2+}- and Eu^{3+}- based phosphors will be provided.

1.2.1 Energy levels of free Mn^{4+} ion and Mn^{4+} in the crystal field

Tetravalent manganese has a $3d^3$ electronic configuration. Three electrons can be distributed over five *d* orbitals in 120 ways as can be found from the combination formula ${}_nC_r = \frac{n!}{r!(n-r)!}$, where n is the maximum number of electrons in five orbitals and r is the number of electrons available. The formula gives $\frac{10!}{3!\cdot 7!}$ = 120 microstates for the d^3 configuration. The microstates form eight terms, ^4P, ^4F, ^2P, $^2D_{(1)}$, $^2D_{(2)}$, ^2F, ^2G, and ^2H. General symbol for the term is ^{2S+1}L, where S is the total spin quantum number and L is the total orbital angular number (L = 0, 1, 2, 3, 4, 5, 6, 7… for the S, P, D, F, G, H, I, K terms respectively etc.). The ground state defined by Hund's rules for Mn^{4+} corresponds to the ^4F term. In quantum mechanical approach the

wavefunctions for each term are built up based on the angular momentum addition theory. In practice the relative energy positions of each term can be calculated by combination of the Racah parameters (Table 1.1). The numerical values of B and C were calculated for free d^3 ions, and for Mn^{4+} they are equal to 1160 and 4303 cm^{-1}, respectively[8].

Table 1.1. The mathematical relationship between Racah parameters and electrostatic terms energy in the ions with d^3 electron configuration. The ground term energy is taken as 0.

Term	Energy
^4F	0
^4P	15B
^2P	9B + 3C
$^2D_{(1)}$, $^2D_{(2)}$	$20B + 5C \pm \sqrt{193B^2 + 8BC + 4C^2}$
^2F	24B + 3C
^2G	4B + 3C
^2H	9B + 3C

If we place a free ion in some crystalline matrix, the spherical symmetry will be reduced to the point group symmetry of the crystallographic site and the energy levels of a free ion will be split. This split can be analyzed with the group theory, which provides the number of energy levels in the crystal field and establishes the selection rules for the allowed and forbidden electronic transitions. Nevertheless, the relative positions of the levels on the energy diagram are unknown. This problem for the transition metal ions was solved by Y. Tanabe and S. Sugano[9–11]. In their approach along with the Racah parameters B and C, a new parameter, Dq, is used to describe crystal field strength. This parameter shows the strength of the free ion energy level splitting by the crystal field. As we can see, there are three independent parameters, yet two-dimensional diagrams were proposed by Tanabe and Sugano by plotting the E/B versus Dq/B while fixing the C/B ratio. The Tanabe-Sugano diagram for the ion with the d^3 electron configuration in the

octahedral crystal field is shown in Figure 1.9. The octahedral surrounding is typical for Mn^{4+} in solids.

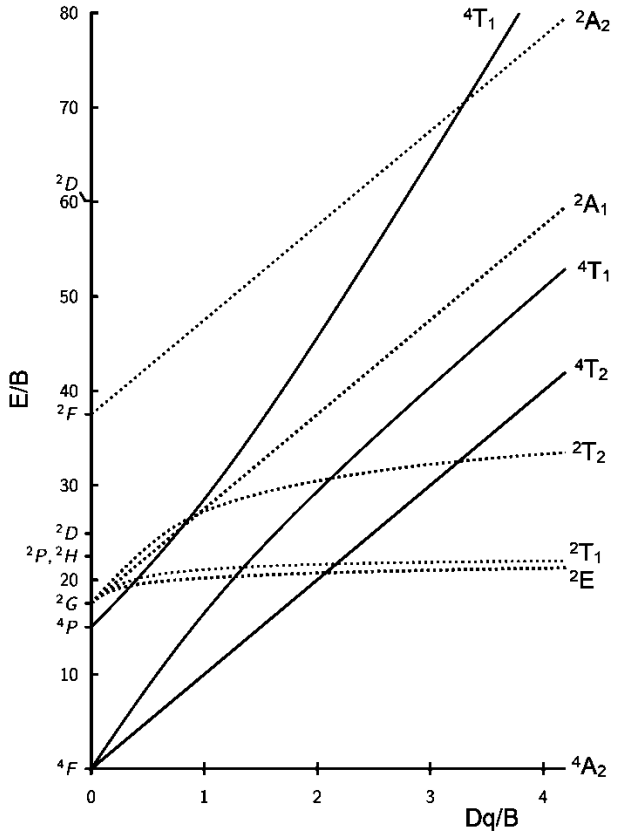

Figure 1.9. Tanabe–Sugano diagram for the ion with d^3 electron configuration in the octahedral crystal field. Solid lines are for spin quartets, dashed – for spin doublets.

The energy interval between the $^4A_2$ (ground state) and $^4T_2$ levels equals to 10 Dq and can be used to calculate the Dq value from the absorption data. The weak crystal field correspond to the left part from the crossover point of the $^4T_2$ and ^2E levels, the strong crystal field – to the right part from the crossover. The Dq/B value at the crossover is around 2.1. Note, that due to high electric charge and small ionic radius, Mn^{4+} is always in the strong crystal field part of diagram, meaning that the first excited state of Mn^{4+} is ^2E. This is important since the emission of the

tetravalent manganese is originated from the ^2E to $^4A_2$ transition. A key point here is that the energy of ^2E level is almost independent on the crystal field strength.

Note that transition between the electronic states of any d^n configuration are forbidden by parity selection rule. This selection rule can be partially lifted by admixture of the states with an opposite parity. The spin selection rule forbids the transition between the state with a different spin. The spin selection rule is partially relaxed via spin-orbit coupling of spin-quartet and spin-doublet states. The transitions between the states with the same spin will have much higher intensity.

Thus, in the absorption spectra of the Mn^{4+}-activated materials, we expect three dominating peaks originating from the following transitions: $^4A_2 \rightarrow {}^4T_2$ (energy is 10Dq), $^4A_2 \rightarrow {}^4T_1(^4F)$ and $^4A_2 \rightarrow {}^4T_1(^4P)$. The $^4A_2 \rightarrow {}^4T_2$ excitation happens in the visible light region of the spectra, while two other peaks are in the UV region. The absorption peak originating from the $^4A_2 \rightarrow {}^4T_1(^4P)$ transition usually overlaps with the ligand-to-Mn^{4+} charge-transfer absorption peak (charge transfer is illustrated with the molecular orbitals theory in the Appendix A1). Transitions to the spin doublet state ($^2T_2$, $^2A_1$, $^2A_2$), although forbidden by spin selection rule, can manifest in the spectrum as bands overlapped with the spin allowed ones. The emission of Mn^{4+} originates in the $^2E_2 \rightarrow {}^4A_2$ transition and lies in the red region of the spectra (Figure 1.10).

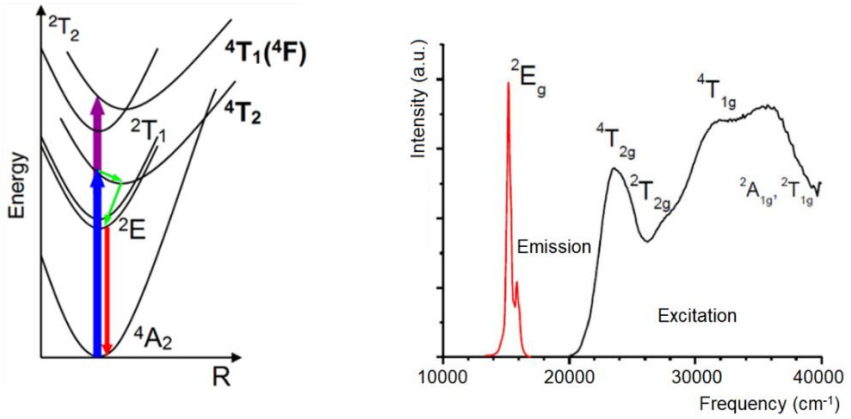

Figure 1.10. (left) Configurational coordinate diagram for Mn^{4+}. The $^4A_2 \rightarrow {}^4T_2$ transition shown as blue arrow, $^4A_2 \rightarrow {}^4T_1(^4F)$ transition – as purple arrow, $^2E_2 \rightarrow {}^4A_2$ transition – as red arrow. The nonradiative processes shown as green arrows. (right) Excitation and emission data for the Mn^{4+} doped magnesium oxofluoride with peak assignment (data from M. G. Brik and A. M. Srivastava[12]).

The B, C, and Dq values can be calculated from the experimental absorption and emission spectra as[2]:

$$D_q = E(^4T_2 \leftarrow {}^4A_2)\ /10 \tag{1.6}$$

$$\frac{D_q}{B} = \frac{15(x-8)}{x^2 - 10x} \tag{1.7}$$

$$x = \frac{E(^4T_1(^4F)) \leftarrow {}^4A_2) - E(^4T_2 \leftarrow {}^4A_2)}{D_q} \tag{1.8}$$

$$\frac{E(^2E_2 \rightarrow {}^4A_2)}{B} = \frac{3.05C}{B} + 7.9 - \frac{1.8B}{D_q} \tag{1.9}$$

The values of Racah parameters calculated from the experimental data are reduced compared to a free ion because of chemical bonds formation and the reduced electron repulsion in a host matrix (nephelauxetic effect).

1.2.2 Nephelauxetic effect

According to the Tanabe-Sugano diagram, the energy of the $^2E_2 \rightarrow {}^4A_2$ transition is almost independent on the Dq/B. However, the position of the Mn^{4+} emission peak arising from the $^2E_2 \rightarrow {}^4A_2$ varies significantly (around 100 nm) between different host matrixes. The position of the peak depends on the Mn^{4+} chemical bonding to its surrounding because of the nephelauxetic effect. As we mentioned earlier, the more covalent surrounding shifts the emission to a longer wavelength and more ionic one to a shorter wavelength. If shorter wavelengths are required for practical applications, fluoride host matrixes should be used for Mn^{4+} doping. On the other hand, Mn^{4+} doped oxides would produce longer emission wavelengths. The nephelauxetic effect and the position of the ^2E energy level was found to be in linear dependence: $E(^2E \rightarrow {}^4A_2) = -880.49 + 16261.92\beta_1$, where β_1 is a measure of the nephelauxetic effect and can be calculated as:

$$\beta_1 = \sqrt{(\frac{B}{B_0})^2 + (\frac{C}{C_0})^2} \qquad (1.10),$$

where B_0 and C_0 are parameters for a free ion[13].

1.2.3 Mn^{4+} phosphors for lighting

For decades the application of the Mn^{4+}-activated materials was quite specific. The phosphor prepared from magnesium oxide, magnesium fluoride and germanium oxide was almost exclusively used for the color correction of high-pressure mercury lamps.[14] However, progress in solid-state lighting brought a renaissance to research on Mn^{4+}-doped materials.

If we aim to create a light source for general application, we need a source of white light. An incandescent lamp creates white light by a resistive heating of a tungsten wire. In luminescent lighting, including solid-state lighting, the white light is usually created via the down-conversion of the UV light. Due to the Stokes shifts, phosphors are capable of this down-conversion. Thus,

by combination of the short wavelength source, such as light emitting diode (LED), and a few phosphors, a white light can be created through the mixing of colors. The approach is known as phosphor-converted LED (PC LEDs) and is successfully commercialized. On the other hand, the so-called fluorescent lamps are still widely used. These lamps rely on the luminescence as well. The source of the excitation there is a UV light produced by mercury vapor under electrical discharge.

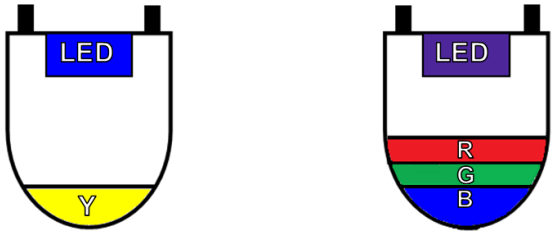

Figure 1.11. White light PC LED schemes: blue LED with yellow phosphor (left) and UV LED with RGB phosphors (right).

PC LED technology has already become the dominant one for general lighting. The excitation sources here are UV or blue LEDs and no toxic mercury is required. To create white light, a few color mixing schemes can be used. A simple two component scheme includes a blue LED and yellow phosphor, typically Ce^{3+} dopped garnet[15] (Figure 1.11). Higher quality lighting demands a red component, missing from a previous scheme. The “red-green-blue” scheme, widely used from the pioneering times of color television, is employed in many white PC LEDs. The UV chip (LED) in this scheme excites the combination of three phosphors resulting in white light (Figure 1.11). Alternatively, a combination of three red, green, and blue LEDs can be used, but such an approach is less efficient.

What are the requirements for the red phosphors used in general lighting? A good candidate converts the excitation light efficiently, does not absorb the emission of other components, does

not change the color, and keeps efficiency over the lifetime of the device. The red emission should be in the spectral region where human eye remains sensitive to it. Additionally, the preparation of the material should be cost efficient and reasonably ecologically friendly.

The number of host matrixes suitable for the Mn^{4+} doping is significant. Here we limit our descriptions to general considerations, while more details can be found in the various reviews on the topic[16–18]. There are a few important points important for the phosphor development:

- Mn^{4+} requires octahedral surrounding, thus the structure of a host matrix should be known to avoid unsuccessful doping attempts.
- In the fluoride matrices the emission of the Mn^{4+} is shifted to the shorter wavelength compared to the oxides.
- At the elevated temperatures many phosphors demonstrate quenching of their emission. The temperature dependent measurements are required.

1.2.4 Germanates as host matrices for Mn^{4+}

Tetravalent manganese has a similar ionic radius[19] and the same formal charge as tetravalent germanium. Therefore, compounds of tetravalent germanium, including oxides, are good candidates for the phosphor preparation via the partial substitution of Mn for Ge. On the other hand, the octahedral oxygen surrounding for Ge can be found in a limited number of compounds and the most common coordination is a tetrahedral one.[20]

The first commercial Mn^{4+} phosphors were germanates[21,22], initially referred as "$4MgO{\cdot}GeO_2$" and "$3.5MgO{\cdot}0.5MgF_2{\cdot}GeO_2$". The displayed compositions indicate the reagents ratios in the synthesis, but not to the actual composition of the phosphors. The actual compositions of two phases, $Mg_{28}Ge_{10}O_{48}$ and $Mg_{28}Ge_{7.5}O_{38}F_{10}$, and their crystal structures were reported much

later[23,24]. As expected, the presence of the octahedral oxygen surrounding was confirmed for germanium atoms.

As we mentioned before, the octahedral coordination of germanium is not common in oxygen surroundings. Before the preparation of a phosphor, we need to know the structure of the host material. In the Inorganic Crystal Structure Database (ICSD)[25] there are almost 450 entries on the ternary germanium-oxygen compounds and almost 900 entries on the quaternary ones. Among these compounds, polygermanates of the alkali and alkaline earth metals are well structurally characterized and have been tested as potential Mn^{4+} phosphors[21–26]. We can separate these germanates into few groups: 1) $R_2Ge_4O_9$ (R = Li-Rb) alkali tetragermanates; 2) RGe_4O_9 (R = Sr, Ba) alkaline earth tetragermanates; 3) $K_2BaGe_8O_{18}$ and $Li_3RbGe_8O_{18}$ octagermanates. The compositions of these compounds are quite similar; however, their structures are not the same.

More details on the structural features of the alkali and alkaline earth germanates and their phosphorescence are provided in the Chapters 5 and 6. Here we only mention some general information: the structures of all mentioned germanates are built from anionic frameworks with cations located in the channels of the frameworks. The anionic frameworks consist of vertex sharing GeO_n polyhedra (n = 4 or 6). The visual similarity of frameworks should not be considered as equal to the structural similarities.

1.2.5 Mn^{4+} phosphors, Eu^{3+} and Eu^{2+} phosphors

Beside the red phosphors based on Mn^{4+} doping of various oxides and fluorides, promising phosphors were found among the Eu^{2+}- and Eu^{3+}-containing phases. Based on the literature, the two common material families employed for the red emitting components of PC LEDs are Mn^{4+} and Eu^{2+} activated phases. Some features of the Eu^{n+} luminescence are provided below.

Phosphors containing europium ions as activators have been known for a very long time. For example, the cathode ray tube color television became possible thanks to red luminescence of the $Y_2O_2S:Eu^{3+}$. Not surprisingly many materials doped with europium were tested as red emitters for the luminescent lighting. Europium ($[Xe]4f^76s^2$ electron configuration) adopts two oxidation states in its compounds, +2 and +3. Both Eu^{2+} and Eu^{3+} display luminescence when doped into a proper matrix. The absorption and emission properties of these two species are quite different because they originate from the different electronic transitions.

Eu^{3+} ($4f^6$ configuration) is characterized by less than half-filled 4*f* shell. The 4*f* orbitals are shielded from the surrounding by $5s^2$ and $5p^6$ shells. Because of this shielding, the optical transitions within the 4*f* shell are not significantly influenced by the host lattice. Crystal field splitting of the energy levels in Eu^{3+} is significantly lower than in Mn^{4+}. Transitions within the 4*f* shell are strongly parity forbidden, but partial relaxation of the selection rule is possible via the admixture of the 5*d* states. Also, the optical transitions are characterized by sharp lines in the spectrum since the $\Delta R = 0$ (change in the configurational coordinate). Additionally, the absorption bands associated with allowed charge transfer transitions are observed for Eu^{3+}. Eu^{3+} is characterized by red emission, and this emission contains a few lines originating from the ^5D to ^7F_J (J = 0, 1…6) transitions (Figure 1.12). In contrast to Eu^{3+}, the optical transitions in Eu^{2+} are allowed $4f \leftrightarrow 5d$ ones. The absorption and emission bands can be manipulated significantly by host lattice via crystal field, since the 5*d* orbitals are larger and not shielded in contrast to 4*f* orbitals. Additionally, nephelauxetic effect can be employed for tuning of the Eu^{2+} optical properties. Also, the optical properties of the divalent europium depend considerably on the temperature.

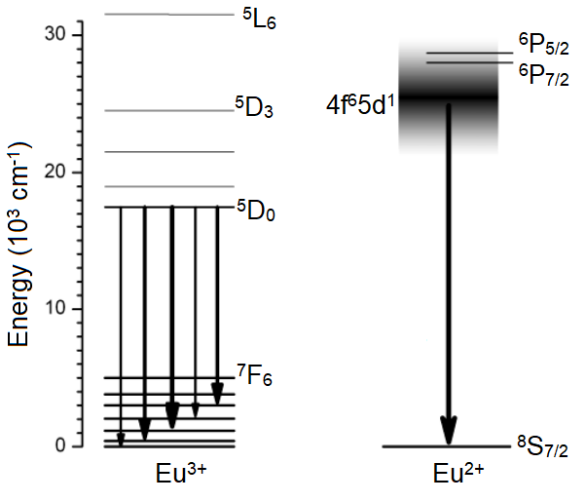

Figure 1.12. Energy levels of Eu^{3+} and Eu^{2+} in $Ca_3Y_2(SiO_4)_3$[26]

The host matrices are quite different in the Eu^{3+} and Eu^{2+} red phosphors: for Eu^{3+}, oxides are commonly used, while nitrides are typical hosts for Eu^{2+}. Nitrides provide more covalent surrounding compared to the oxides thus shifting the emission of the Eu^{2+} to the red part of the visible spectra.

All three activators, namely Mn^{4+}, Eu^{3+} and Eu^{2+}, have advantages and disadvantages when compared to each other. The advantage of the Mn^{4+} is the wide absorption band, which however does not overlap with the emission of the other components on the PC LEDs. Also, the preparation procedures for the host matrices are simple and solid-state reactions can be used in the air atmosphere. Eu^{3+} exhibits stable emission at the elevated temperatures, while optical properties of Eu^{2+}can be easily tuned.

The disadvantages for Mn^{4+} are thermal quenching of the phosphorescence and tendency to emit in a far-red region of the spectra in the oxide matrices. For Eu^{2+}, a serious disadvantage is the high cost of preparation of nitride host matrixes (prepared under high pressure of nitrogen and

at very high temperature). Eu^{3+} exhibits a line emission, which can be disadvantageous, but also in many cases the transitions within the 4*f* shell cannot be excited by UV LEDs.

As we can see, both Mn^{4+} and Eu^{n+} phosphors possess advantages and disadvantages. Currently, some rare-earth based phosphors are already used for the general lighting. If we aim to replace the scarce rare-earth metals in phosphors with transition metals, the rigorous study is required. The study on the new material should start with the structure characterization. As we demonstrated earlier, the structure and composition of the host matrix has significant impact on the luminescence of Mn^{4+}.

Chapter 2. Preparation and characterization methods for the new materials

2.1 Synthesis of the new materials

The main approaches for the synthesis of new materials in this work are solid state reactions, flux growth, and crystallization from melts. The choice of a method depends on the synthesis goals. The aim of a flux growth and crystallization from melts is to obtain crystals of the new phases suitable for the single crystal X-ray diffraction (XRD) experiments. Solid-state reactions are employed mostly for the synthesis of pure polycrystalline materials for the property measurements.

The study on a new material in this work typically starts with the characterization of its structure (see 2.2) with single crystal XRD, thus methods yielding single crystals are employed first. Once the composition is established, the preparation of a bulk material via the solid-state routine is pursued.

The starting materials in this research are various inorganic oxides, carbonates, and halides. Halides with lower melting points (compared to oxides) are commonly used as fluxes. During the flux growth, the initial reagents in the desired ratios are mixed with an excess of a compound with relatively low melting point (flux). The flux acts as a reaction medium and may also act as a reagent. There are many possible fluxes, but in this research, we employed alkali and alkaline earth halides. The mixture of reagents is placed in an inert crucible (we used Pt) and heated up above the melting point of a flux. After some dwelling at the certain temperature, a slow cooling (typically 5-10 °/ hour) starts and the reaction products solidify. Then the products are analyzed. Crystallization from a melt is similar to the flux growth in terms of the heating and cooling profiles, however no additional media is used.

Solid-state reactions, as the name suggests, are done at temperatures below the melting points of the reagents. The preparations include thorough mixing and grinding of the initial reagents with mortar and pestle or by ball milling followed by the pressing of the mixed powders into pellets. These pellets are annealed at certain temperatures for extended periods of time. A few regrinding steps may be required to achieve phase-pure samples.

2.2 X-ray diffraction for the materials characterization

Crystalline materials demonstrate three-dimensional periodicity of the atomic arrangement. Because of this periodicity, the structure of a crystal can be described within the small volume of a space (unit cell) which can be extended in three dimensions infinitely. Physical properties of the extended crystalline solids depend on the composition and structure. To study the structures and composition of new materials, various diffraction techniques, such as X-ray diffraction (XRD), neutron diffraction, and electron diffraction are used. XRD is the very common technique for structural and phase analyses. The laboratory based XRD instruments are called diffractometers. They consist of X-ray source, high-voltage generator, goniometer, optics for the incident and diffracted X-ray beams, detector, and control unit. More details on the X-ray generation and interactions of X rays with materials are provided below.

The direct observation of atoms in the crystalline materials is impossible with X-rays. Instead, we collect diffraction information in the so-called reciprocal space, and then this information is transformed into the one in the real space.

2.2.1 Generation of X-rays

X-rays are a form of the electromagnetic radiation, discovered by W.C. Röntgen, who was awarded the 1901 Nobel Prize in Physics for his discovery. The wavelength of the X rays lies in ≈0.1-100 Å region, but the wavelengths of 0.5-2.5 Å are usually employed to study the atomic structure.

In laboratory diffractometers, X-ray tubes are used as sources of the X-ray radiation. The vacuum sealed X-ray tube is schematically shown in Figure 2.1.

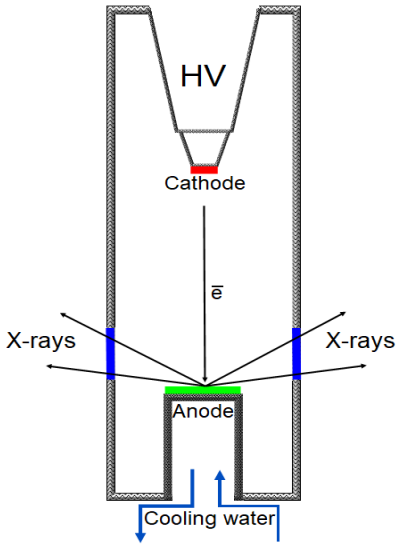

Figure 2.1. Scheme of the laboratory X-ray tube. Be windows are shown in blue.

The tube is sealed under ultra-high vacuum ($<10^{-9}$ mbar) and consists of a cathode (source of electrons, typically tungsten filament), water-cooled anode, and beryllium windows. Electrons generated by the emission from a hot cathode are accelerated toward the anode by means of a high electrostatic potential between cathode and anode (tens of kV of voltage). The collision of electrons with the metal anode generates X-rays and produce a lot of heat as well, thus the external water cooling is necessary. X-rays come out through the Be windows and can be further manipulated before reaching the sample. There are two or four Be windows located 90 ° apart at

the cross section of an X-ray tube. One or two opposite windows are for the point focused beam, used in single crystal XRD, another or other two windows are for the line focused beam, used in powder XRD. The point focused beam has a higher photon flux (i.e. brighter) than a line focused one.

X-rays of the tremendous brightness are created in cyclic particle accelerators known as synchrotrons (such as the Canadian Light Source). Here, the electrons travel in circular orbits and are accelerated by magnetic field. There are several beamlines for the outcoming X rays at each synchrotron facility, and they are geared towards different applications (spectroscopy, diffraction, imaging). Obviously, the construction and maintenance of a synchrotron requires great efforts and large budget, thus such facilities are shared by many users across the country (or between different countries), and they are created and supported by national governments.

2.2.2 X-ray tube emission spectrum

The schematic view of the X-ray spectrum from an X-ray tube is shown in Figure 2.2. It features several distinct peaks and a continuous “white radiation”. The continuous radiation is created by the decelerating electrons. Some electrons decelerate almost instantly, while other – over some period of time, thus producing the continuous X-ray spectrum. Generally, the white radiation is not used in the X-ray diffraction method.

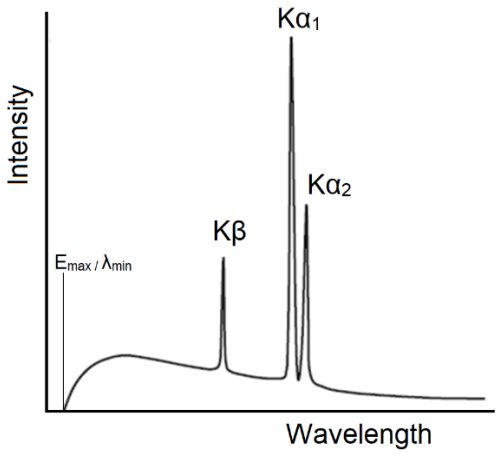

Figure 2.2. X-ray spectrum from a laboratory X-ray tube.

The minimum wavelength (and thus the maximum energy) of the X-rays depends on the accelerating voltage. If an electron stops instantly, all the kinetic energy is transferred to the emitted photon:

$$\frac{mv^2}{2} = eV = \frac{hc}{\lambda} \quad (2.1)$$

$$\text{so } \lambda_{min}\,(\text{Å}) = \frac{1.240\times10^4}{V} \quad (2.2),$$

where m is the rest mass of electron, v is the electron velocity, e is the charge of electron, V – acceleration voltage, h – Planck's constant, c – velocity of light in vacuum, λ_{min} – shortest X-ray wavelength.

Distinct peaks in the X-ray spectrum are known as characteristics lines and depends on the anode material. These lines originate in the electronic transitions from the upper levels of an atom to the lover levels, which become vacant after the impact of the accelerated electrons. In this work two types of anodes were used – copper and molybdenum. Their characteristic wavelengths are shown in Table 2.1.

Table 2.1. Characteristic wavelength of Cu and Mo anodes*

Anode	Wavelength, A°			
	Kα	$K\alpha_1$	$K\alpha_2$	Kβ
Cu	1.54187	1.5405929(5)	1.54441(2)	1.39225(1)
Mo	0.71075	0.7093171(4)	0.71361(1)	0.63230(1)

*$\lambda K\alpha = (2\lambda K\alpha_1 + \lambda K\alpha_2)/3$.

2.2.3 X-ray scattering

Various processes are possible when X-rays interact with a matter, but only the process of coherent scattering is meaningful for XRD. In coherent scattering, the wavelengths of the incident and scattered beams remain the same.

X-rays are scattered by the electron cloud of an atom (Figure 2.3). For the forward scattered X-rays, there is no path difference between the incident and diffracted beams ($\vec{k} = \vec{k}'$). If the beams are scattered at some angle, a path difference, δ, for the diffracted beam appears ($\vec{k} \neq \vec{k}''$), and thus the phase mismatch between the beams is introduced. Scattering power of an atom declines with an increasing scattered angle. For each element in the Periodic Table this decline can be illustrated by an atomic scattering factor *f* versus $\frac{\sin\theta}{\lambda}$ graph.

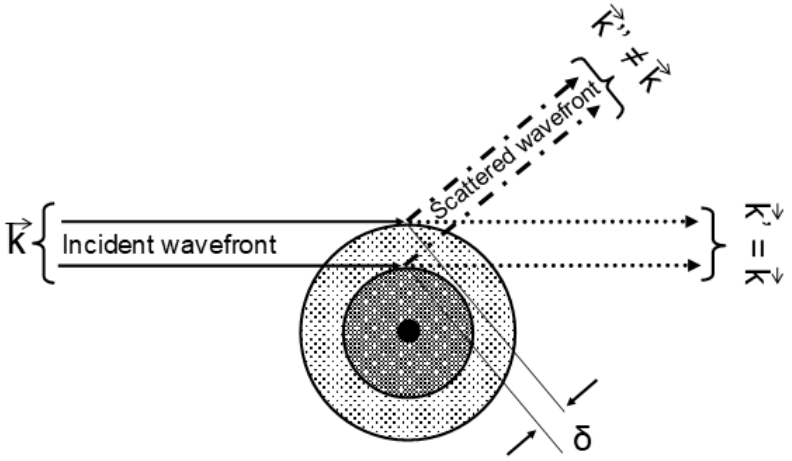

Figure 2.3. X-ray scattering from an atom.

The scattering from a regular array of atoms (a crystal lattice) can be described with Bragg's law, a fundamental relationship in X-ray crystallography. Bragg's law (after W.H. Bragg and W.L. Bragg, 1915 Nobel Prize laureates in Physics) establishes the relationship between the diffraction angle (Bragg angle), spacing between the crystallographic planes of a lattice, and the wavelength of the incident beam (Figure 2.4).

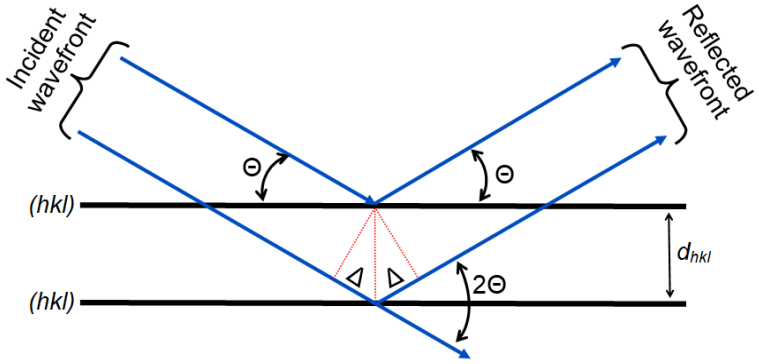

Figure 2.4. Illustration of Bragg's law.

In figure 2.4, the incident beams are reflected from the crystallographic family of planes with the *(hkl)* Miller indices and d_{hkl} interplanar distance. The angle between the incident beam and plane, the diffracted (reflected) beam and plane is Bragg's angle θ. Δ is a path difference between a pair of waves before and after reflection. The total path difference is $2\Delta = d_{hkl} \sin\theta$. For constructive interference, the path difference should be nλ, where n is an integer and λ is a wavelength of the incident wavefront. Thus, the Bragg's law is

$$2d_{hkl} \sin\theta = n\lambda \qquad (2.3),$$

where n is usually taken as unity (for n>1, $2d_{hkl} \sin\theta_{hkl} = n\lambda$ and $d_{hkl} = nd_{nh,nk,nl} \Rightarrow 2d_{nh,nk,nl} \sin\theta_{nh,nk,nl} = \lambda$). If Bragg's law is satisfied, the diffraction event is observed.

2.2.4 Reciprocal lattice. Ewald sphere

The description of the XRD diffraction phenomenon with Bragg's law is complicated in three-dimensional space created by crystallographic planes. The picture is simplified in the reciprocal lattice. The elementary translations of the reciprocal lattice are defined with translations of the real lattice as:

$$\vec{a}^* = \frac{\vec{b}\times\vec{c}}{V}, \vec{b}^* = \frac{\vec{c}\times\vec{a}}{V}, \vec{c}^* = \frac{\vec{a}\times\vec{b}}{V} \quad (2.4)$$

where V is the volume of the real unit cell. The reciprocal interplanar distance d^*_{hkl} is reversed of d_{hkl}:

$$d^*_{hkl} = \frac{1}{d_{hkl}} \quad (2.5),$$

with d^*_{hkl} vector perpendicular to the corresponding crystallographic plane. Now, the infinite set of the (*hkl*) planes in the real (direct) space is represented by a point, corresponding to the end of the d^*_{hkl} vector in the reciprocal space. The symmetry of the direct space is preserved in the reciprocal space.

To visualize the diffraction conditions in the reciprocal space, the construction known as Ewald's sphere is useful. This imaginary sphere has a radius of 1/λ (λ is an X-ray wavelength) and the origin of the reciprocal lattice is tangent to the surface of the sphere. We assume a crystal to be in the center of the sphere (Figure 2.5 left).

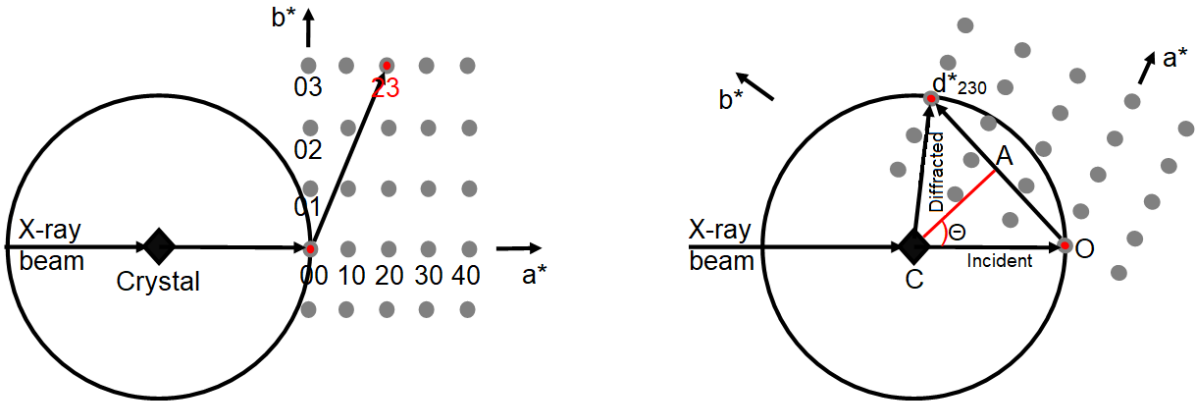

Figure 2.5. Ewald sphere with r =1/λ, a crystal at the center of the sphere, and the corresponding reciprocal lattice with a* and b* lattice vectors. For all reciprocal lattice points indices *l* assumed to be 0 so only *h* and *k* are given for the clarity. Incident and diffracted beam vectors are connected by d^*_{230} if diffraction happens from the 230 reciprocal point. $\overline{CA}$ is an altitude of a triangle formed by incident and diffracted beam vectors and d^*_{230} vector.

At the certain rotations of a crystal (and the corresponding rotation of the reciprocal lattice), the lattice point 230 intersects with a surface of the sphere. If C is the center of the sphere, $\overline{CO}$ = 1/λ and $\overline{OA}$ = $d^*_{230}/2$ (right part of the Figure 2.5). On the other hand, $\overline{OA} = \overline{CO}\sin\theta = (1/\lambda)\sin\theta$ and $d^*_{230} = 1/d_{230}$, thus $\frac{\sin\theta}{\lambda} = \frac{1}{2d_{230}}$ and so $2d_{230}\sin\theta = \lambda$, which is a Bragg's condition for the diffraction from the (*230*) planes. This derivation works for each point of the reciprocal lattice, meaning that diffraction is observed when the reciprocal lattice point is at the surface of the Ewald sphere. The corresponding diffracted beam is a vector from the center of the Ewald sphere to the intersection of the reciprocal lattice point with the sphere.

2.2.5 X-ray diffraction from a single crystal and a polycrystalline sample

If a crystal is fixed in space, the Bragg condition may be satisfied only for a few reciprocal lattice points, touching the Ewald sphere at this given orientation. This generates few diffracted X-ray beams at the corresponding 2θ angles to the incident beam. We can register the outcoming beams with some detector, placed after the sample and some number of spots (also called reflections) is expected (Figure 2.6).

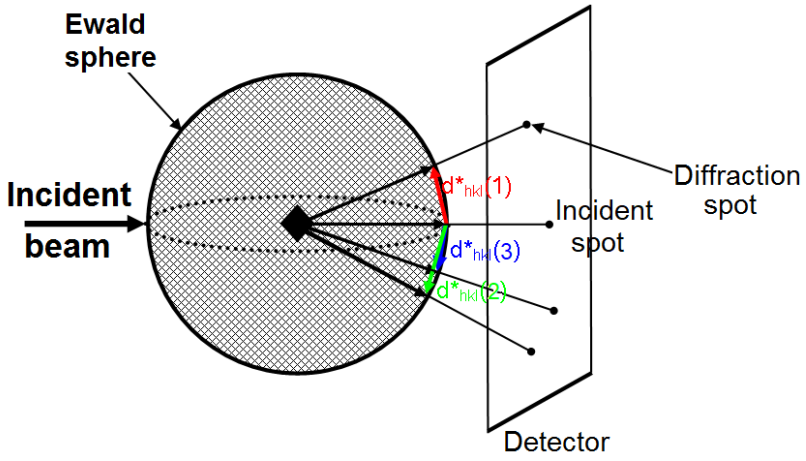

Figure 2.6. Diffraction from a single crystal. At the given moment of time, Bragg's condition is satisfied for a few d^*_{hkl} ($d^*_{hkl}(1)$ – $d^*_{hkl}(3)$, shown in red, green, and blue respectively). On the detector three spots are expected plus an incident beam spot.

Polycrystalline sample (powder) is assumed to consist of an infinite number of tiny crystals, oriented randomly in all possible directions. Thus, the orientation of the reciprocal lattice for each grain is also random. When some volume of a polycrystalline sample is exposed to the X-rays, Bragg's condition is satisfied in many grains and thus a multitude of the diffracted beams is generated. For a given d^*_{hkl} across many grains all the corresponding reciprocal lattice points are arranged as a circle perpendicular to an incident beam on the surface of the Ewald sphere. The scattered vectors form a cone with 4θ solid angle. The axis of the cone is an incident beam. If we

place a detector behind the sample, the diffraction pattern known as Debye rings is registered. Each ring corresponds to the certain d_{hkl} of a given sample (Figure 2.7).

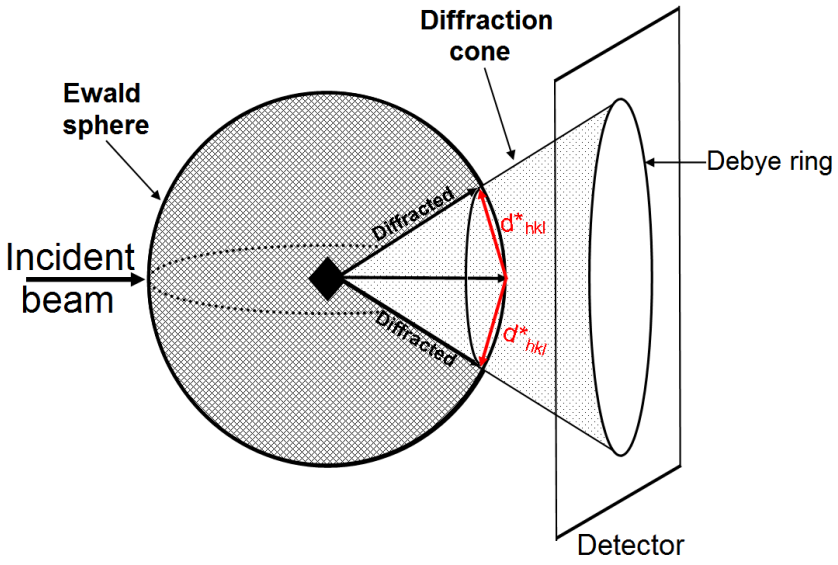

Figure 2.7. Diffraction from a polycrystalline sample. Bragg's condition is satisfied for d^*_{hkl} simultaneously in numerous grains generating a diffraction cone. The projection of the cone on the detector is a Debye ring. In a real sample Bragg's condition is satisfied for several d^*_{hkl} and thus a corresponding number of the concentric rings constitute the diffraction pattern.

2.2.4 Structure factor

Intensity of the diffracted beam depends on many factors, external and internal. The structure factor (or structure amplitude), F_{hkl}, is crucial for the structure determination from the experimental data. The experimental intensity of the diffracted X-ray beam is proportional to the square of the structure amplitude. F_{hkl} describes the amplitude of the X-ray scattered by a unit cell containing multiple atoms:

$$F(h) = \sum_{j=1}^{n} g^j t^j(s) f^j(s) \exp(2\pi i(hx^j + ky^j + lz^j)) \quad (2.6),$$

- where F(h) is a structure amplitude of a *hkl* Bragg reflection. The reflection is represented by a vector h. F(h) is a complex number and can be shown as a vector;
- n is a total number of atoms in the unit cell (including all symmetry equivalents);
- *s* is $\sin\theta_{hkl}/\lambda$;
- g^j is an occupancy factor of a *j*th atom;
- t^j is an atomic displacement parameter, describing displacement of a *j*th atom;
- f^j is an atomic scattering factor of a *j*th atom, a function describing an interaction of an incident X-ray beam with a certain type of atom (element) as a function of $\sin\theta/\lambda$;
- i is the imaginary unit.

From Euler's formula $e^{ix} = \cos(x) + i\sin(x)$ for (2.4) we have

$$F(h) = \sum_{j=1}^{n} g^j t^j(s) f^j(s) \cos(2\pi(hx^j + ky^j + lz^j) +$$

$$+ i \sum_{j=1}^{n} g^j t^j(s) f^j(s) \sin(2\pi(hx^j + ky^j + lz^j) \quad (2.7).$$

The structure amplitude includes the real (A) and imaginary (B) components, and (2.5) can be rewritten as:

$$F(h) = A(h) + iB(h) \quad (2.8).$$

F(h) can be visually represented as a vector in two dimensions with real and imaginary axes perpendicular to each other:

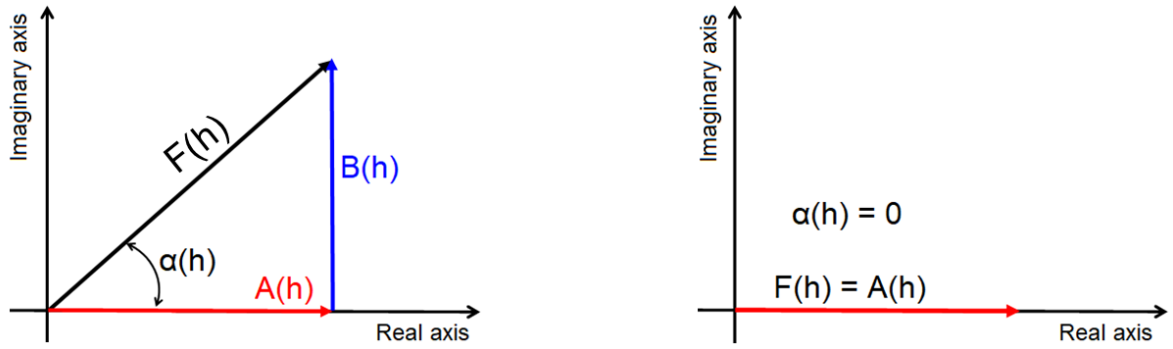

Figure 2.8. Vector representation of the structure amplitude F(h). Projection of F(h) on the real axis is A(h) (red), projection on the imaginary axis is B(h) (blue, shifted from the origin for clarity). In the acentric structure (*left*) $B(h) \neq 0$, in the centrosymmetric structure (*right*) $B(h) = 0$. The α(h) angle is a "phase angle".

F(h) can be represented by its magnitude |F(h)| and the phase angle α(h) varying from 0 to 2π. In the centrosymmetric structure each atom with the (x,y,z) coordinates has its symmetry equivalent with the (-x,-y,-z) coordinates. Since sin(-x) = -sin(x), the imaginary component in the (2.5) equation turns zero. The phase angle in that case is either 0 or π.

2.2.5 Fourier transformation and phase problem

The XRD pattern from a single crystal is not a direct view of the spatial distribution of atoms, but an image of the reciprocal space. To extract the information on the crystal structure, the experimental data should be transformed into the direct space physical characteristics. The transformation known as a Fourier transformation (forward or reverse) relates the real and reciprocal spaces. More specifically for the XRD, the transformation relates the electron density ρ(x) and structure amplitude F(h) (integrals substituted by sum):

$$F(h) = V \sum_x \rho(x) \exp\left[2\pi i (h \cdot x)\right] \qquad (2.9)$$

$$\text{and } \rho(x) = \frac{1}{V}\sum_h F(h)\exp\left[-2\pi i(h \cdot x)\right] \qquad (2.10)$$

where V is the volume of the real unit cell, x are coordinate vectors in the real unit cell, h – coordinate vectors in the reciprocal cell. The position of the atoms in the unit cell represented by the electron density can be found from the experimental structural amplitudes via Eq. (2.11):

$$\rho_{xyz} = \frac{1}{V}\sum_{h=-\infty}^{h=+\infty}\sum_{k=-\infty}^{k=+\infty}\sum_{l=-\infty}^{l=+\infty}|F_{hkl}^{obs}|cos[\,2\pi(hx+ky+lz)-\alpha_{hkl}] \quad (2.11)$$

where $|F_{hkl}^{obs}|$ is an absolute value of structure amplitude and α_{hkl} is a phase angle.

The absolute values of $|F_{hkl}^{obs}|$ can be extracted directly from the experimental intensity, however the phase angles are lost. This creates so-called phase problem since the phase angles are crucial for the Fourier transformation.

One approach to solve the phase problem is known as direct methods. In this approach the nonnegative electron density is postulated for any part of the unit cell, $\rho_{xyz} \geq 0$. The second postulate is that the structure consists of the nearly spherical atoms spread almost evenly in the unit cell. This generates a special relationship between phases of the triplets of reflections with arithmetically related indices, h, h′, and h-h′. General expression for the phase determination from triplets (tangent formula) was introduced by Karle and Hauptman[27] (awarded 1985 Nobel Prize in Chemistry).

$$\tan\alpha_h = \frac{\sum_h |E_{h'}||E_{h-h'}|\sin(\alpha_{h'}+\alpha_{h-h'})}{\sum_h |E_{h'}||E_{h-h'}|\cos(\alpha_{h'}+\alpha_{h-h'})} \quad (2.12),$$

with the sum over all triplets including the reflection in question, h. E_h is a normalized structure factor:

$$E_h = \frac{|F_{hkl}|}{\langle F_{exp}^2\rangle^{1/2}} \quad (2.13)$$

and

$$\langle F_{exp}^2 \rangle = \sum_{j=1}^{n} f_j^2(s) \quad (2.14)$$

is the expected average value of the structure factor. In Eq. (2.12) $f_j(s)$ is the atomic scattering factor of the jth atom, $s = \sin\theta/\lambda$.

If the phases are known, the electron density (E-map) can be calculated from Fourier transformation:

$$\rho_{xyz} = \frac{1}{V} \sum_{h=-\infty}^{h=+\infty} \sum_{k=-\infty}^{k=+\infty} \sum_{l=-\infty}^{l=+\infty} E_{hkl} \cos[\, 2\pi(hx + ky + lz - \alpha_{hkl}^{direct})] \quad (2.15).$$

Nowadays a powerful method known as "intrinsic phasing" (implemented in SHELXT[28] software) is commonly used for a structure solution. This method belongs to the "dual space" group of methods, with data refinement done in both real (electron density) and reciprocal (phases) spaces. The procedure starts with an assignment of the initial phases, $\Phi_{initial}$, from the Patterson superposition minimum function.[29] Then, Fourier transformation in used to calculate an electron density $\rho(r)$ from observed intensities I_{obs} and initial phases $\Phi_{initial}$. Among the calculated electron density maxima, 30% are omitted randomly in the next step (random omit procedure). From the maxima, the normalized mask $M(r)$ is calculated and a new electron density $\rho'(r) = \rho(r) \cdot M(r)$ is found (negative ρ set to 0). New phases are calculated from $\rho'(r)$ and refined with Eq. 2.12. These phases are used in the next cycle of the refinement. The dual-space refinement is performed in a *P*1 space group, while the correct space group is determined after from the symmetry of the phases and the systematic absences.

2.2.6. Single crystal XRD

In this work, the composition and the structures of the new phases were determined from single-crystal XRD data. In 2.2.5 it was shown that at the certain orientation of the crystal and an

X-ray source only a few reciprocal lattice points touch the Ewald sphere. To collect enough data, the crystal is rotated during the XRD experiment, thus more reciprocal lattice points have the Braggs conditions satisfied. A data collected at the certain orientation of a crystal constitute a single frame (Figure 2.9). A full data collection includes up to several hundred frames (with 1° increment for rotation, for example) depending on the crystal structure. The instrument used in this work is STOE IPDS II. It features Mo anode and image plate detector system. The rotation of the sample is possible along two axes, ϕ and ω. The details on the data collection, processing, structure determination and refinement given in Chapters 3-6.

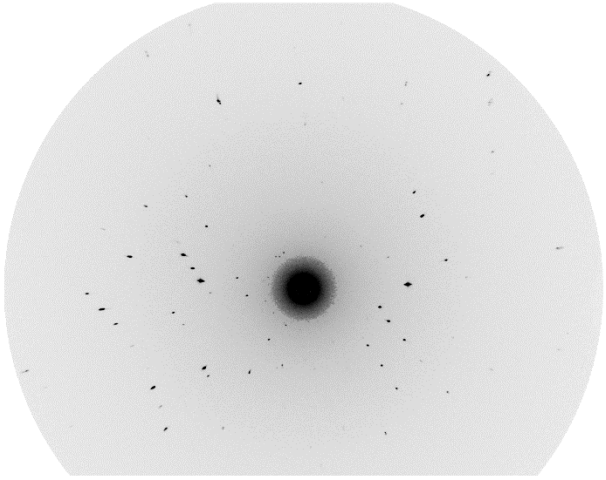

Figure 2.9. A single frame from the STOE IPDS II. The dark spots are the reflections, the big dark area in the middle is from a beam stop, preventing the detector damage.

As we mentioned in 2.2.5, the electron density map can be calculated from the experimental XRD data. The peaks on the map correspond to the atoms. The model obtained in the first step, referred as structure solution, needs to be verified and further refined. The least-square refinement

is used to validate the quality of the structural model. The most used refinement figures of merit, known as residual factors (R factors) are:

$$R_1 = \frac{\sum |F_{obs}| - |F_{calc}|}{\sum |F_{obs}|} \qquad (2.16)$$

$$wR_2 = \left[\frac{\sum w({F_{obs}}^2 - {F_{calc}}^2)^2}{\sum w({F_{obs}}^2)^2}\right]^{1/2} \qquad (2.17)$$

$$\text{GooF} = S = \left[\frac{\sum w({F_{obs}}^2 - {F_{calc}}^2)^2}{N-P}\right]^{1/2} \qquad (2.18)$$

where F_{obs} stands for the experimentally observed structure factors, F_{calc} – for the calculated structure factors; wR_2 includes weighting factors w, calculated form the weighting scheme and accounting for the different intensities of the observed reflections[30]; GooF stands for "goodness of fit"; N – is the total number of reflections, P – total number of the refined parameters.

Additionally, the residual electron density is also used to judge quality of the structural model. The good refinement should not have intensive residual density peaks (or holes). Overall, the model is expected to be reasonable from the crystallographic and chemical points of view.

2.2.7 Powder XRD

The physical principles behind the XRD from single crystal and polycrystalline samples (powder) are the same. However, since the three-dimensional nature is lost in powder diffraction, the more common application for powder XRD is phase analysis. If crystallographic data are available from single crystal XRD, powder diffraction can be used to refine the structural parameters.

The X-ray scattering from a given d^*_{hkl} of a polycrystalline sample manifest itself as a diffraction cone. However, the Bragg's condition is satisfied for many d^*_{hkl}simultaneously producing several cones at once (Figure 2.10). There is no need to register the entire Debye ring

as we assume the ring to be uniform. Instead, we can measure intensity over some area at the circumference of equatorial plane of the Ewald sphere (Figure 2.10).

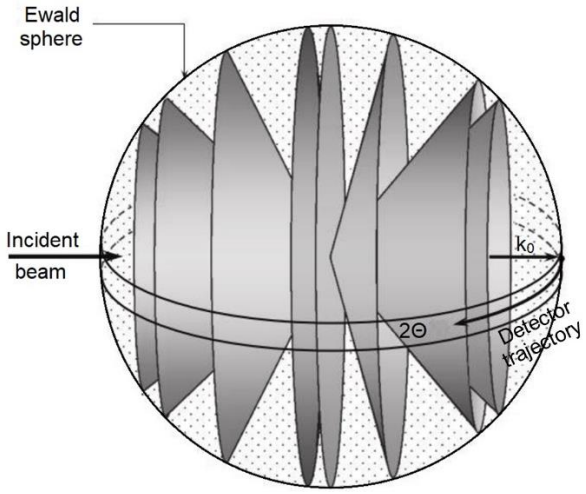

Figure 2.10. Coaxial diffraction cones from a polycrystalline sample[31].

The data collected on the powder diffractometer (powder diffraction pattern) is usually represented as a plot of intensity against Bragg's angle 2θ. The refinement of the structural parameters is done via the least-square Rietveld refinement[32,33] (known as full profile refinement). The Rietveld refinement is also used for the quantitative phase analysis of the diffraction data. The figures of merit for Rietveld refinement are:

$$\mathrm{Rp} = \frac{\sum_{i=1}^{n} |Y_i^{obs} - Y_i^{calc}|}{\sum_{i=1}^{n} |Y_i^{obs}|} \times 100\% \qquad (2.19),$$

$$\mathrm{R_{wp}} = \left[\frac{\sum_{i=1}^{n} w_i \left(Y_i^{obs} - Y_i^{calc}\right)^2}{\sum_{i=1}^{n} w_i \left(Y_i^{obs}\right)^2} \right]^{1/2} \times 100\% \qquad (2.20),$$

$$\chi^2 = \frac{\sum_{i=1}^{n} w_i \left(Y_i^{obs} - Y_i^{calc}\right)^2}{n-p} \qquad (2.21),$$

where Y_i^{obs} and Y_i^{calc} are observed and calculated intensity of the *i*th data point, w_i is weight of the *i*th data point ($w_i = 1/Y_i^{obs}$); *n* is the total number of the measured points, *p* is a number of free

least-square parameters. Rp is a profile residual, R_{wp} is a weighted residual, χ^2 is a goodness of fit. The details on the powder XRD data refinement are given in Chapters 3-6.

In this work, powder XRD data were collected on a PANalytical X'pert PRO diffractometer. It features copper anode, germanium monochromator, and 1D detector. The wavelength used for the data collection is Cu $K\alpha_1$ (Table 2.1), while $K\alpha_2$ is eliminated with the monochromator. Ground samples are placed on the silicon zero background wafer. During the data collection the sample is constantly rotated for the better averaging of a signal.

2.3 Neutron diffraction

Study of crystal structures by means of the diffraction is not limited to X-rays. Electrons and neutrons can be also scattered by crystal lattices due to the wave–particle duality. The wavelength corresponding to the beam of particles can be calculated from the de Broglie equation:

$$\lambda = \frac{h}{mv} \quad (2.22),$$

where h is a Planck's constant ($h = 6.626 \cdot 10^{-34}$ Js), m is a rest mass of a particle, *v* is its velocity (in this work neutrons with wavelength of 2.2095 Å were used, meaning their velocity was around 1.8 km/s).

Neutron diffraction experiments cannot be carried out in a regular laboratory since neutrons are produced in nuclear reactors. The interaction of neutrons with matter is insignificant, thus much more sample is required compared to the XRD experiment. The features of neutron scattering differentiating it from X-ray diffraction are: 1) neutrons are scattered by nuclei and magnetic moments, but not by electron density; 2) the scattering factor of a given nucleus is fixed and does not depend on the scattering angle; 3) the atomic number has no connection to the scattering factor so different isotopes scatter differently.

In this work neutron diffraction was employed to test a bulk MgF_2 sample for the presence of water molecules or OH^- groups. In the XRD experiment, it is hard to find the position of hydrogen atoms since they only have one electron. Thus, we could not differentiate between OH^- and F^- groups in some specific cases, since the charge of both groups is the same and the X-ray scattering powers of O and F are very close.

In a neutron diffraction experiment, the absence of hydrogen atoms in a MgF_2 sample can be proven convincingly. Hydrogen has a large incoherent scattering cross-section (orders of magnitude larger than magnesium or fluorine). Thus, the presence of hydrogen in MgF_2 sample would result in a significant increase of the angle-independent background. Comparison between neutron scattering data from an empty aluminum container and the same container filled with MgF_2 sample did not reveal any significant increase in the background, and thus the absence of hydrogen atoms in MgF_2 was confirmed.

2.4 Nuclear magnetic resonance

The crystal structures obtained from single crystal XRD shows the averaged atomic positions. The movement of some ions, molecules or groups is treated as a disorder during the structure solution and refinement, therefore some fine structural details can be lost. On the other hand, the nuclear magnetic resonance (NMR) techniques allow to probe for the local environment, disorder, and dynamics effects.

Nuclei with non-zero spin I are characterized by magnetic moment μ:

$$\mu = \gamma \hbar I \quad (2.23),$$

where γ is gyromagnetic ratio. In the absence of the external magnetic field, the nuclear magnetic moments are distributed randomly. In a strong external field B_0, however, the nuclei start to align.

This alignment is not perfect and nuclear spins precess around B_0 with a certain frequency. For the simplest case of I = ± ½, the nucleus can be depicted as magnetic dipole with two possible orientations of the μ_z projection on the external field direction *z*: parallel and antiparallel. Two orientations create two different energy levels (μ_z parallel to B_0 goes down in energy, antiparallel – goes up) with energy difference proportional to the external field:

$$\Delta E = 2\mu_z B_0 \quad (2.24).$$

The transition between two states can be stimulated by an external electromagnetic radiation at frequency $\nu = (\gamma/2\pi)B_0$, which is usually in a radio wave frequency range. Through the application of the external radio frequency, a signal associated with energy absorption by nucleus can be registered.

In the NMR experiment, the so-called chemical shift is used to describe the nuclei in the compound under study. Chemical shift characterizes the change of the NMR peak position of a certain nucleus caused by the shielding effects, compared to the signal from a standard material. Additional information is provided by NMR peak splitting, which arises from the spin-spin coupling. Chemical shifts and peak splitting provide the information on the local environment.

The solid-state NMR is operated under the rotation of the sample at the certain angle to the external field (Figure 2.11). The magic angle spinning (MAS, magic angle is $\theta = 54.74°$, so $3\cos^2\theta = 1$) technique allows to mitigate the negative effects arising from the strong anisotropy of the solid materials (compared to typical liquid NMR sample), so the peaks can be resolved properly.

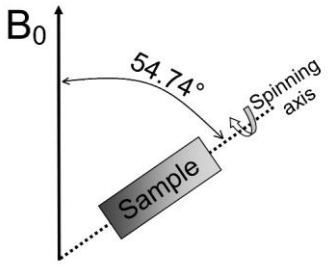

Figure 2.11. MAS solid state NMR scheme.

2.5 Optical properties measurements

Photoluminescence excitation (PLE) and emission (PL) spectra for the new phosphors in this work were registered on a Varian Carry Eclipse spectrometer. The three basis components of a spectrometer are an excitation source, a sample holder, and a detector.

The excitation source on the Varian instrument is a xenon flash lamp capable of the continuum output of light in the UV-vis region of the spectrum. To control the excitation wavelength the Agilent instrument utilizes the diffraction gratings monochromator. The second monochromator is used for the emission wavelength. The monochromator slit can be changed depending on the sample.

The photomultiplier tube sensitive up to 900 nm is used as a detector of the emitted light. Photomultiplier tube is operated on the secondary emission of electrons. The detector multiplies the current produced by the emitted light by many orders of magnitude (up to 10^8 times) so even a weak flux of photons can be detected. The signal from the detector is further amplified and displayed on a read-out device (computer display). The sample holder used in this work is a quartz wafer placed in a quartz cuvette and inclined to the incident beam (Figure 2.12).

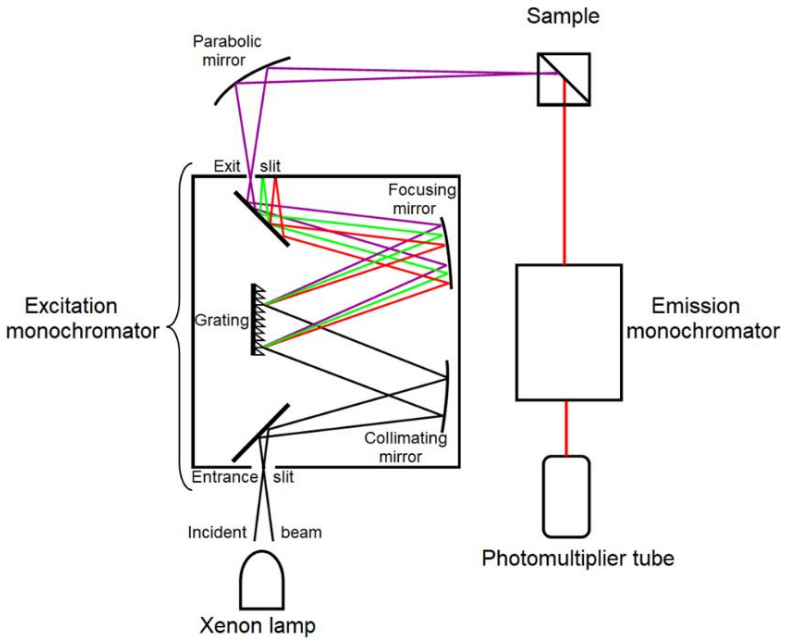

Figure 2.12. Scheme of the UV-vis-NIR spectrometer (not to scale). The monochromator scheme is shown only for the excitation light for charity. Emission monochromator is operated on the same principles.

Chapter 3. Two new magnesium and magnesium-lead fluorogermanates and revision of the $Mg_{28}Ge_{7.5}O_{38}F_{10}$ phase

The following chapter was published as "Two new magnesium and magnesium-lead fluorogermanates and revision of the $Mg_{28}Ge_{7.5}O_{38}F_{10}$ phase" article in Journal of Solid State Chemistry (*J. Solid State Chem.* **2021**, *293*, 121741). Based on the initial study by Dr. R. Bagum, the candidate synthesized the new materials, characterized them with XRD, and prepared the manuscript for publication. Dr. Z.B. Yan conducted NMR study. Dr. J.P. Clancy conducted neutron diffraction experiments.

A new compound, $Mg_3Ge_{1-\delta}O_{4(1-\delta)}F_{2(1+2\delta)}$ was obtained by high temperature solid state reactions and flux method and its structure was characterized by single crystal X-ray diffraction. The structure relates to the silicate mineral norbergite, $Mg_3SiO_4(OH)F$, a member of the humite mineral group. The diffraction experiment revealed a deficiency of the Ge site in the new structure, which can be compensated by the substitution of either OH^- groups or F^- anions for O^{2-} anions. The combination of the NMR, neutron scattering, and IR spectroscopy experiments suggest that the F^- substitution is most likely; thus, the $Mg_3Ge_{1-\delta}O_{4(1-\delta)}F_{2(1+2\delta)}$ formula is suggested. The F^- substitution is present for the side product of the $Mg_3Ge_{1-\delta}O_{4(1-\delta)}F_{2(1+2\delta)}$ synthesis, the compound known as $Mg_{28}Ge_{7.5}O_{38}F_{10}$. Refinement of the twined $Mg_{28}Ge_{7.5}O_{38}F_{10}$ crystal showed a slightly higher Ge content and the final composition was assigned as $Mg_{28}Ge_8O_{40}F_8$. The PbF_2 flux method yielded a new compound, $Mg_2Pb_2Ge_2O_7F_2$. The structure of this digermanate is related to the group of naturally occurring and synthetic silicates containing R^{3+} cations. High-temperature powder XRD experiments showed that the $Mg_3Ge_{1-\delta}O_{4(1-\delta)}F_{2(1+2\delta)}$ phase cannot be synthesized from Mg_2GeO_4 and MgF_2 in air due to the transformation of magnesium fluoride into MgO.

3.1 Introduction

Magnesium germanates and fluorogermanates doped with tetravalent manganese are highly efficient red-emitting phosphors that are used for a lamp color correction[14,22], improvements of the lamp color rendering index[34,35], and thermometry. The first attempt to utilize Mn^{4+}-activated magnesium germanates as phosphors was made by Leverenz[36] in 1936. However, the stoichiometric meta- and orthogermanates ($MgGeO_3$ and Mg_2GeO_4, respectively) showed impractically low efficiency. The compositional modification made by Williams[21] increased the efficiency of the new magnesium germanate phosphor significantly, making it practically valuable.

Williams[21] established that doubling the amount of magnesium oxide compared to the Mg_2GeO_4 stoichiometry improves the optical properties: the optimal MgO : GeO_2 ratio for the synthesis was found to be 4:1. The compositing of this phosphor was wrongly assigned as Mg_4GeO_6. The next vital step was made by Thorington[22], who was able to push the overall efficiency of material even higher by a partial replacement of magnesium oxide with magnesium fluoride.

While the synthetic methodology to obtain a highly efficient germanate phosphor was developed, the structural data were incomplete. Robbins and Levin explored the MgO–GeO_2 phase diagram[37], but they did not establish the structure of Mg_4GeO_6. Von Dreele et al.[23] were able to grow suitable crystals from the PbO flux and reformulated the Mg_4GeO_6 ($4MgO{\cdot}GeO_2$) phase as $Mg_{14}Ge_5O_{24}$. The same group also established the structure and composition of the magnesium fluorogermanate, $Mg_{28}Ge_{7.5}O_{38}F_{10}$[24] by growing crystals from the PbF_2 flux. This phase is isomorphous with $Mg_{14}Ge_5O_{24}$ ($Mg_{28}Ge_{10}O_{48}$) but has a significant Ge deficiency and a substantial fluorine-oxygen substitution. $Mg_{28}Ge_{7.5}O_{38}F_{10}$ is the only verified magnesium fluorogermanate structure to date. Lyon and Ehlers proposed the existence of a series of $n Mg_2GeO_4 \cdot MgF_2$ fluorogermanate (n = 1, 2, 3, or 4)[38] analogous to the silicates from the humite mineral family. The authors described the synthetic routes for all phases, however no other reports on the structures of the $n Mg_2GeO_4 \cdot MgF_2$ compounds could be found.

During our research targeted to clarify the structure and composition of the $Mg_{28}Ge_{7.5}O_{38}F_{10}$ phosphor, we were able to grow crystals and establish the structure of the first member of the $n Mg_2GeO_4{\cdot}MgF_2$ family with n = 1, $Mg_3GeO_4F_2$ (the actual composition is $Mg_3Ge_{1-\delta}O_{4(1-\delta)}F_{2(1+2\delta)}$). Compared to the silicate analogue, the $Mg_3GeO_4F_2$ structure has a pronounced deficiency on the Ge site. Additionally, the structural refinement of the $Mg_{14}Ge_4O_{20}F_4$ (or $Mg_{28}Ge_8O_{40}F_8$) crystals yielded a lower Ge deficiency than in $Mg_{28}Ge_{7.5}O_{38}F_{10}$ [24]. Also, the

crystals of the magnesium-lead fluorogermanate $Mg_2Pb_2Ge_2O_7F_2$ were grown from the PbF_2 flux. This paper discusses the synthesis, structure, and composition of these three fluorogermanate.

3.2 Experimental

3.2.1 Reagents

Crystals of $Mg_3Ge_{1-\delta}O_{4(1-\delta)}F_{2(1+2\delta)}$, $Mg_2Pb_2Ge_2O_7F_2$, and $Mg_{14}Ge_4O_{20}F_4$ were obtained by a flux method and solid-state reactions. The initial reagents for all syntheses were powders of MgF_2 (Alfa Aesar, 99.99 wt. %), MgO (Alfa Aesar, 99.995 wt. %) GeO_2 (Alfa Aesar, 99.999 wt. %), and PbF_2 (Alfa Aesar, 99.9 wt. %). Magnesium orthogermanate, Mg_2GeO_4, also was used as a starting material; it was prepared through the solid state route proposed by Lyon and Ehlers[9].

3.2.2 Synthesis

*Solid state synthesis of $Mg_3Ge_{1-\delta}O_{4(1-\delta)}F_{2(1+2\delta)}$ **(1)** and $Mg_{14}Ge_4O_{20}F_4$ **(2)***

The mixtures of Mg_2GeO_4 and MgF_2 in the 1:1 and 2:1 molar ratios were ground thoroughly in an agate mortar. Acetone was added during mixing to achieve a better homogenization. After acetone removal the powders were pressed into an 8 mm pellets under 2 metric tons of pressure. The pellets were broken into pieces and placed in stainless steel tubes (1/4″ or 6.35 mm inner diameter, 35-40 mm length). Stainless steel tubes were found to be less reactive compared to the initially tested Ta tubes. The tubes were sealed by arc welding under argon. The stainless steel tubes were placed into silica tubes and sealed under high vacuum. The samples were annealed in a box furnace at 1100 °C either for 25 hours (1:1 molar ratio) or 36 hours (2:1 molar ratio). The products of both reactions were mixtures of $Mg_3Ge_{1-\delta}O_{4(1-\delta)}F_{2(1+2\delta)}$, $Mg_{14}Ge_4O_{20}F_4$, and MgF_2.

*Synthesis of $Mg_3Ge_{1-\delta}O_{4(1-\delta)}F_{2(1+2\delta)}$ (**1**) and $Mg_2Pb_2Ge_2O_7F_2$ (**3**) crystals from PbF_2 flux*

The mixture of MgO, MgF_2, and GeO_2 in the 3.5:0.5:1 molar ratio was well homogenized using agate mortar and pestle, and then annealed at 1200 °C for 16 hours in an alumina crucible in air. The pre-reacted sample was mixed with PbF_2 in the 1:3 ratio (by weight). The mixture was placed into a Pt crucible inside an alumina crucible with a cap. A cap was sealed with high-temperature cement. After cement solidified, the setup was heated in a box furnace to 1100°C at 100°C/h, kept for 4 h, then cooled down to 800°C at 4°C/h. The reaction yielded crystals of $Mg_3Ge_{1-\delta}O_{4(1-\delta)}F_{2(1+2\delta)}$ and $Mg_{14}Ge_4O_{20}F_4$.

The mixture of MgO, MgF_2, and GeO_2 in the 2:1:1 molar ratio was homogenized, pressed into a pellet and annealed at 1200°C for 16 hours. After annealing, the sample was grinded and mixed with PbF_2 in the 1:3 ratio by weight. The sample was placed in a box furnace at 500°C and heated up to 920°C at 100°C/h. After 8 hours a furnace cooled down to 800°C at 9°C/h. The solidified product contained $Mg_2Pb_2Ge_2O_7F_2$ crystals.

3.2.3 X-ray diffraction

Single crystal X-ray diffraction experiments (Mo Kα radiation) were carried out on STOE IPDS II and Bruker APEX II diffractometers. The absorption correction was performed using X-shape software [39] (STOE) and SADABS[40] program (Bruker). The structures were solved by direct methods (SHELXL97-2014[41], Olex2[42]) and refined by full-matrix least squares[43] method against F^2 in an anisotropic approximation. The structure of $Mg_{14}Ge_4O_{20}F_4$ was refined from a twin crystal using the HKL5 data file.

Powder X-ray diffraction was performed on a PANalytical X'Pert PRO diffractometer (Cu $K\alpha_1$ radiation) equipped with the Ge monochromator. The high temperature diffraction data were

collected using an Anton Paar high temperature chamber HTK 2000 N with a Pt heating strip. The data were collected in the 20-80° 2θ range. Rietveld refinements were done with the Rietica software[44].

3.2.4 Solid-state nuclear magnetic resonance (NMR) spectroscopy

Solid-state magic-angle spinning (MAS) NMR experiments were performed on a Bruker Widebore-300 MHz Avance III system using a 1.3 mm outer diameter rotor with a double resonance probe. The MAS frequency in all experiments was 60 kHz. For both ^{1}H and ^{19}F NMR measurements the spin echo pulse sequence was employed, where an 86.2 kHz radiofrequency (RF) field was applied in the ^{1}H experiments and a 142.8 kHz RF field was used in the ^{19}F experiments. All the chemical shift assignments in the ^{1}H and ^{19}F NMR analyses were referenced using water (H_2O, $\delta = 4.78$ ppm) and trichlorofluoromethane ($CFCl_3$, $\delta = 0$ ppm) respectively.

3.2.5 Neutron powder diffraction and IR spectroscopy

Neutron powder diffraction was carried out on the MgF_2 reactant at McMaster University nuclear reactor. The data were collected for the empty container (as a reference) and the sample. The wavelength used in these measurements was determined to be 2.2095 Å (Y_2O_3 standard reference sample). The data were collected in the 10-80° 2θ range and refined with the Rietica software[44] (Figure 3.5).

Infrared (IR) absorption spectroscopy was performed on the MgF_2 reactant and the product of the solid state reaction on the Thermo Scientific Nicolet iS 5 FTIR Spectrometer (Figure 3.6).

3.3 Results and Discussion

3.3.1 Structure of $Mg_3Ge_{1-\delta}O_{4(1-\delta)}F_{2(1+2\delta)}$ (1)

The structural solution for the $Mg_3Ge_{1-\delta}O_{4(1-\delta)}F_{2(1+2\delta)}$ (**1**) crystals ($Mg_3GeO_4F_2$ for simplicity) obtained either by a flux or a solid state synthesis was straightforward and all sites were assigned to the corresponding atoms. The F and O atoms were easily identified, and they occupied independent sites. The F and O displacement parameters did not suggest any deficiencies or disorder. The $Mg_3GeO_4F_2$ structure is shown in Figure 3.1. The Ge atoms occupy the oxygen tetrahedra, while the Mg atoms fill in the O_4F_2 octadedra. The $Mg_3GeO_4F_2$ structure can be seen as consisting of infinite 2D layers within the *ab* plane (Figure 3.1). Within a layer, the MgO_4F_2 octahedra form infinite zigzag chains by sharing the O-O or F-F edges, and the chains are joined via the GeO_4 tetrahedra through the O corners. Two neighboring layers, that are mirror images of each other, are offset by $\frac{1}{2}\vec{a}$ and stacked along the *c* direction. The layers are joined by sharing the F atoms between the MgO_4F_2 octahedra as well as the O atoms between the MgO_4F_2 octahedra or MgO_4F_2 octahedra and GeO_4 tetrahedra from different layers. Each O atom is shared between three MgO_4F_2 octahedra and one GeO_4 tetrahedron and, thus, is surrounded by three Mg and one Ge atoms in a tetrahedral fashion. Each F atom is shared only between three MgO_4F_2 octahedra, and its coordination environment is a distorted trigonal planar one. Bond lengths in $Mg_3GeO_4F_2$ structure are in good agreement with the average literature values[20,45] of 1.75 Å and 2.09 Å for GeO_4 and MgO_6 polyhedra respectively. The Mg-F bonds in the structure are slightly shorter (2.00–2.03 Å) than Mg-O bonds. This agrees with the data for $Mg_3SiO_4F_2$ [46].

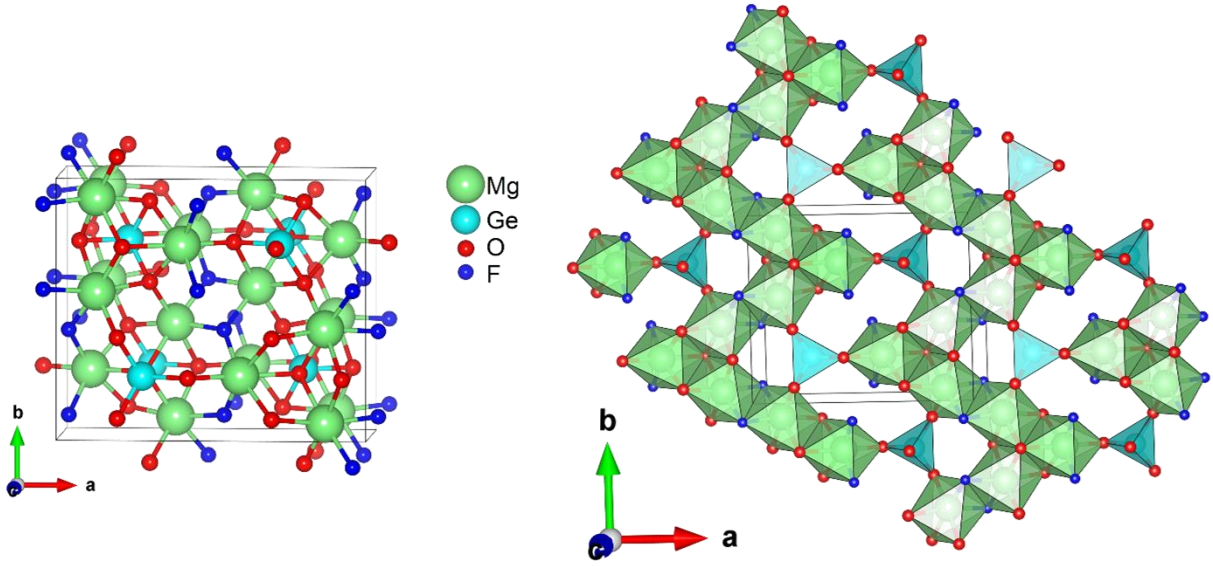

Figure 3.1. (left) Ball and stick representation of the $Mg_3GeO_4F_2$ unit cell. (right) Infinite polyhedral layer parallel to the *ab* plane in $Mg_3GeO_4F_2$.

The single crystal refinement was done for solid state and flux growth crystals (Table 3.1). During the refinement, the occupancy of the sole Ge site was found to be lower than a unity and was set free. The overall structure for both crystals is the same while the level of the Ge deficiency is slightly higher for the solid-state sample (Table 3.1). The unit cell volumes agree with each other for the two refinements (434.0(2) $Å^3$ and 434.6(2) $Å^3$ for $\delta = 0.14$ and 0.11 respectively). The Ge deficiency and accompanying O/F substitution are discussed in more details below.

Table 3.1. Selected crystallographic data and parameters of XRD experiments for structures **1-3**

Compound	$Mg_3Ge_{1-\delta}O_{4(1-\delta)}F_{2(1+2\delta)}$ (**1**)		$Mg_{14}Ge_4O_{20}F_4$ (**2**)	$Mg_2Pb_2Ge_2O_7F_2$ (**3**)
	solid state $\delta = 0.140(3)$	**flux** $\delta = 0.110(3)$		
Instrument	STOE IPDS II	STOE IPDS II	Bruker Apex II	STOE IPDS II
Temperature, K	293	293	100	293
Formula weight	237.36	238.45	1026.70	758.18
Space group	*Pnma*		*Pbam*	*Pbcn*
a (Å)	10.299(2)	10.304(2)	10.2142(5)	7.2258(15)
b (Å)	8.753(2)	8.747(2)	14.4213(6)	11.139(2)
c (Å)	4.814(1)	4.822(1)	5.9275(3)	10.262(2)
V (Å^3)	434.0(2)	434.6(2)	873.13(7)	826.0(3)
Z	4		2	4
D_{calcd}/g cm^{-3}	3.633	3.644	3.905	6.097
μ (mm^{-1})	6.521	6.613	7.487	48.048
F(000)	454	456	984	1304
θ max (°)	34.88	29.16	46.56	32.50
Refl. collected / independent	4870 / 990	4448 / 321	5646 / n/a	11934 / 1493
R_{int}	0.0456	0.0517	0.1298	0.0933
R_1 ($I > 2\sigma(I)$)	0.0301	0.0214	0.0367	0.0325
Largest peak/hole (e/Å^3)	0.78/- 0.80	0.60/- 0.90	1.50 / -1.40	1.61 / -1.50

3.3.2 Refinement of the twined $Mg_{14}Ge_4O_{20}F_4$ (2) crystal

The crystal of $Mg_{14}Ge_4O_{20}F_4$ was a pseudomerohedral twin with the two twin components related by the following relationship in the reciprocal space: $\begin{pmatrix} \vec{a}^{*''} \\ \vec{b}^{*''} \\ c'' \end{pmatrix} = \begin{pmatrix} -1/2 & 3/2 & 0 \\ -1/2 & -1/2 & 0 \\ 0 & 0 & 1 \end{pmatrix} \begin{pmatrix} \vec{a}^{*'} \\ \vec{b}^{*'} \\ \vec{c}^{*'} \end{pmatrix}$.

The twining stems from the fact that the a^*b^* face diagonal is approximately equals $2b^*$. Such twinning creates an illusion of the hexagonal symmetry. Without accounting for the twinning, the structure cannot be refined satisfactorily. Additionally, the data were collected till $2\theta = 93^o$ and at 100 K to achieve the reliable results.

The refinement of $Mg_{14}Ge_4O_{20}F_4$ had similar issues as reported previously [24], namely one tetrahedrally coordinated Ge site (Ge3) was deficient and there was O/F mixtures on three O sites connected to this Ge. The occupancy of the deficient Ge3 site in the structure was refined freely and it converged to 50.8(2) %. The oxygen sites (O7, O8, and O9 in the Supplementary Information) showed occupancies higher than one and had notable thermal ellipsoids. These sites were refined as split O/F sites with the following restrains: the total occupancy of each site is 100% and the displacement parameters for the O and F atoms on the same site are identical. The atomic coordinates of O and F were not coupled. The refinement yielded the following O/F ratios: 62/38(2)%, 54/46(2)% and 50/50(4)% for the O7, O8, O9 sites, respectively. The ca. 50% occupancy of the Ge3 site commands a 50% substitution by F for the O7, O8, O9 atoms to maintain the charge balance. While the O8 and O9 sites displayed the expected 50/50% mixture, the O7 site was significantly richer in O. We believe that the O7 site is equally occupied by O and F, but due to the similar atomic scattering factors of O and F and significant correlations, the refinement did not yield the correct occupancy for the O7 site.

The 50% occupancy of the Ge3 site and 50/50% O/F mixtures may suggest a lower symmetry structure or a superstructure with a full occupancy of the Ge site and a separation of O and F on the individual sites. There was no indication of a superstructure in the reciprocal space. Thus, structural solutions and refinements with lower symmetries (subgroups of *Pbam*) were explored. The idea was to separate the half-occupied Ge3 site in two independent ones, then make one site fully occupied and remove the other one to keep the overall composition. A similar approach was applied to the mixed oxygen and fluorine sites. For example, the *Pbam* symmetry was lowered to the $P2_1am$ subgroup with the same axis orientation. However, the refinement in the new $P2_1am$ space group produced a heavy electron density peak on the previously removed Ge site, and thus the lower symmetry approach was eventually abandoned.

3.3.3 Ge deficiency and environment in $Mg_3Ge_{1-\delta}O_{4(1-\delta)}F_{2(1+2\delta)}$ (1) and $Mg_{14}Ge_4O_{20}F_4$ (2)

The deficiency of the germanium sites in **2** is associated with the fluorine incorporation on the oxygen positions. As mentioned above, there is solid experimental evidence for this; there is an extra electron density next to the O atoms, which stems from the different coordination requirements of the F atoms in structure **2**. The Ge-F distances in the $Mg_{14}Ge_4O_{20}F_4$ structure notably exceed the corresponding Ge-O distances, thus the shift of the fluorine atoms from the original oxygen positions can be detected. In contrast, the refinement of the structure **1** gave only an under-occupied Ge site, and the oxygen atoms did not display unusual occupational or displacement parameters. The reasons for different behaviors for the O atoms surrounding the deficient Ge sites may stem from the Ge deficiency levels; in the $Mg_3Ge_{1-\delta}O_{4(1-\delta)}F_{2(1+2\delta)}$ (**1**) structure, the sole crystallographic Ge site is 14 % underoccupied; on the other hand, the deficiency of the Ge3 site in $Mg_{14}Ge_4O_{20}F_4$ (**2**) is 50 % (the other two Ge sites are fully occupied).

The deficiency appears to be correlated to the level of the distortion of the GeO_4 tetrahedra in **1** and **2**. To describe the degree of this distortion we can use the distance between the Ge atom and the centroid built from its surrounding oxygen atoms. A larger distance corresponds to a more pronounce distortion of the GeO_4 tetrahedra. For Ge in the $Mg_3Ge_{1-\delta}O_{4(1-\delta)}F_{2(1+2\delta)}$ (**1**) structure, this distance is equal to 0.17 Å. For the tetrahedrally coordinated Ge2 and Ge3 in $Mg_{14}Ge_4O_{20}F_4$ (**2**), the distances are 0.02 and 0.25 Å, respectively. The Ge3 site with a more distorted surrounding is the deficient one in $Mg_{14}Ge_4O_{20}F_4$ (**2**).

We would like to emphasize that the discussed Ge deficiencies and distortions of the GeO_4 tetrahedra originate from the changes in the chemical composition due to the F substitution. The charge balance dictates that for one Ge atom removed, four O atoms are replaced by the equivalent number of F atoms. For structure **1**, this yields the $Mg_3Ge_{1-\delta}O_{4(1-\delta)}F_{2(1+2\delta)}$ formula.

It must be stated that incorporation OH^- groups on the O^{2-} sites in **1** would yield an identical Ge deficiency. From the perspective of the single crystal XRD refinement, the O^{2-} and OH^- are often indistinguishable. The possible source of hydroxyl groups are water molecules from one of the initial reagents, namely MgF_2, as suggested by other researchers[38]. In case of the F^- substitution, it may be also difficult to differentiate F^- from O^{2-} via the XRD techniques, if the substitution levels are relatively small. To establish the substituting species, NMR, neutron diffraction and IR spectroscopy studies were performed, and the results are discussed below.

3.3.4 NMR study of $Mg_3Ge_{1-\delta}O_{4(1-\delta)}F_{2(1+2\delta)}$ (1)

To explore the possibility of OH^- or F^- incorporation on the O^{2-} site, we conducted ^1H and ^{19}F NMR study for MgF_2 and the product of the solid-state reaction between Mg_2GeO_4 and MgF_2. From the powder XRD data, the product is a mixture of $Mg_3GeO_4F_2$ (89.9(7) wt. %), MgF_2 (6.4(1)

wt. %) and $Mg_{14}Ge_4O_{20}F_4$ (4.6(1) wt. %). The ^1H NMR suggests absence of protons in the MgF_2 starting material and product. Thus, the presence of OH^- groups in $Mg_3GeO_4F_2$ can be ruled out. It is worth mentioning that the single crystal X-ray analysis performed by us on MgF_2 did not reveal water molecules in the MgF_2 structure. For this XRD experiment we used crystals of the MgF_2 reagent directly, as MgF_2 is sold in the crystalline form.

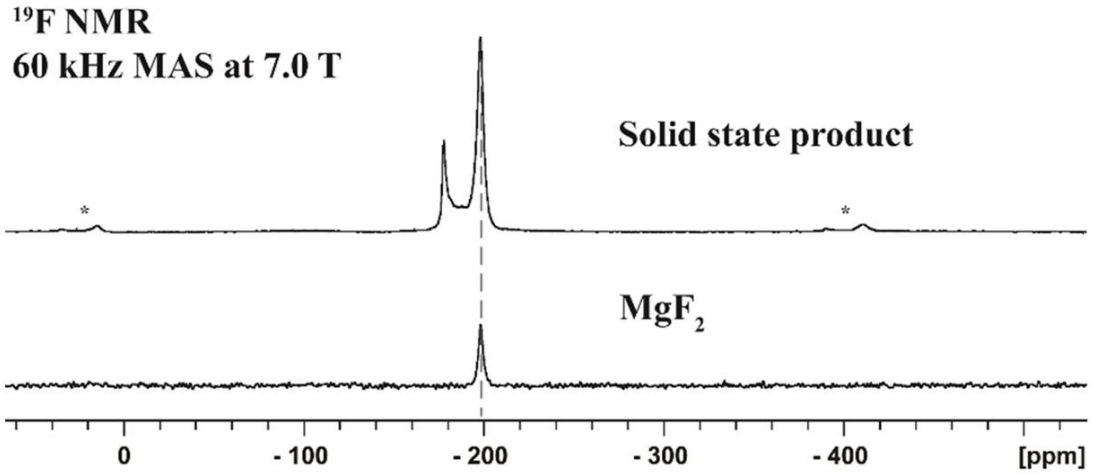

Figure 3.2. The ^{19}F NMR spectral comparison of MgF_2 and the $Mg_3Ge_{1-\delta}O_{4(1-\delta)}F_{2(1+2\delta)}$ (**1**) sample, where * represents MAS spinning side bands.

The ^{19}F NMR study confirmed the presence of MgF_2 impurity in $Mg_3GeO_4F_2$ sample (Figure 3.2). The peak at -177 ppm in the $Mg_3GeO_4F_2$ sample can be associated with the F^- site in the $Mg_3GeO_4F_2$ (**1**) structure. The spectrum contains a small, extra peak at -187 ppm suggesting an additional F^- site. These additional F^- site may stem from the F^- substitution on the O^{2-} sites[47].

3.3.5 Neutron scattering study of MgF_2 and IR spectroscopy

The comparative neutron diffraction experiments on the MgF_2 reagent and empty container showed no increase in the incoherent scattering for the MgF_2 sample. Thus, the MgF_2 reagent is

unlikely to contain any water molecules, which would suggest that presence of OH^- groups in the $Mg_3GeO_4F_2$ structure is also unlikely.

The IR spectra for the MgF_2 reagent and product of the solid-state reaction ($Mg_3GeO_4F_2$, MgF_2 and some $Mg_{14}Ge_4O_{20}F_4$) did not contain absorption peaks in the characteristic region[48] of the $\nu(H_2O)$ vibrations. Thus, these data also support the conclusion that OH^- groups are not present in the $Mg_3GeO_4F_2$ structure.

3.3.6 Structure of $Mg_2Pb_2Ge_2O_7F_2$ (3)

Two independent magnesium atoms in the $Mg_2Pb_2Ge_2O_7F_2$ (**3**) structure occupy positions with the C_i and C_2 symmetry and both have coordination numbers of 6. Their coordination polyhedra are MgO_4F_2 octahedra with two short (Mg–F), two intermediate, and two long bonds. Each MgO_4F_2 polyhedron shares two OF edges with the neighboring ones forming an infinite chain parallel to the *c* direction (Figure 3.3, right). The sole independent Ge atom in the structure **3** forms GeO_4 tetrahedron. Two neighboring GeO_4 tetrahedra share one oxygen atom and form digermanate anion $Ge_2O_7^{6-}$ with Ge1-O3-Ge1 angle equal to 127.9°. These anions connect the chains of the MgO_4F_2 polyhedra creating a 3D framework (Figure 3.3). The sole independent lead atom occupies the *8d* position (*C*1 symmetry) in the voids of the framework and coordinates six oxygen atoms and one fluorine atom. The $PbFO_6$ polyhedra are significantly distorted due to the effect of the $6s^2$ Pb^{2+} lone-pair. All oxygen atoms in **3** are tetrahedrally coordinated by Ge, Mg, and Pb, while the sole fluorine atom have a trigonal coordination by two Mg and one Pb atoms.

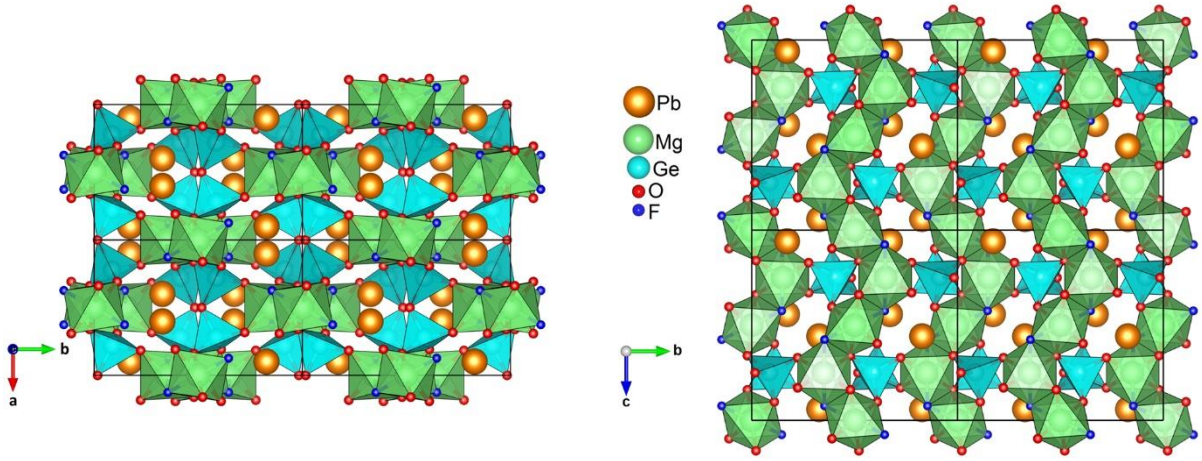

Figure 3.3. Polyhedral representation of the $Mg_2Pb_2Ge_2O_7F_2$ (**3**) structure (2×2×2 unit cells fragment) in two projections. Lead atoms are orange with bonds omitted for clarity.

The $Mg_2Pb_2Ge_2O_7F_2$ (**3**) phase is structurally related to the R^{3+} – Pb disilicate series: two naturally occurring minerals $Fe_2Pb_2Si_2O_9$ (melanotekite) and $Mn_2Pb_2Si_2O_9$ (kentrolite), and synthetic $Al_2Pb_2Si_2O_9$ phase[49–51]. $Mg_2Pb_2Ge_2O_7F_2$ (**3**), melanotekite, and $Al_2Pb_2Si_2O_9$ crystallize with the same *Pbcn* space group[51], while kentrolite – with the $P2_122_1$ group with the *Pbcn* pseudo-symmetry[51]. The R^{3+} cations are six-coordinated and form RO_6 octahedra, which share edges in the same manner as the MgO_4F_2 polyhedra in **3** (i.e. they also form infinite chains). The Si–O–Si angles for the $Si_2O_7^{6-}$ anions are slightly higher[51] than Ge–O–Ge for $Ge_2O_7^{6-}$ in **3**. The disilicate phases contain trivalent R^{3+} cations, which demand the presence of O^{2-} (instead of F^- in **3**) in the structures for the charge balance. The F^- anion in **3** and the O^{2-} anions in the $R_2Pb_2Si_2O_9$ structures have a different coordination. In **3** fluorine has a trigonal coordination by two Mg and one Pb atoms, while the corresponding O^{2-} anions in $R_2Pb_2Si_2O_9$ are tetrahedrally coordinated by two R and two Pb atoms.

3.3.7 High-temperature (HT) powder XRD

Solid-state reaction in open Pt crucibles, aimed to simplify the synthesis of the $Mg_3GeO_4F_2$ (**1**) phase, did not give the desired product, leaving unreacted Mg_2GeO_4 behind. The possible reason for this is the side reaction between MgF_2 and the atmospheric water. To verity this assumption we performed the HT diffraction experiment on the Mg_2GeO_4 and MgF_2 mixture. Mg_2GeO_4 and MgF_2 in the 1:1 molar ratio were mixed in an agate mortar with acetone. The acetone suspension was placed on the Pt heating strip of the HTK 2000 N high temperature chamber. The measurements were done in the 50-1200 °C range with 100° C increments in air.

Analysis of the HT powder data showed that Mg_2GeO_4 did not react with MgF_2 in air and no $Mg_3GeO_4F_2$ formed (Figure 3.4). The diffraction patterns confirmed the decomposition of MgF_2 and the formation of MgO likely due to the following reaction:

$$MgF_2 + H_2O \text{ (atmospheric)} \rightarrow MgO + 2HF \text{ (above 600 °C)} \quad (1).$$

Thus, the synthesis of new magnesium fluorogeramantes requires completely sealed system preventing this undesirable side reaction.

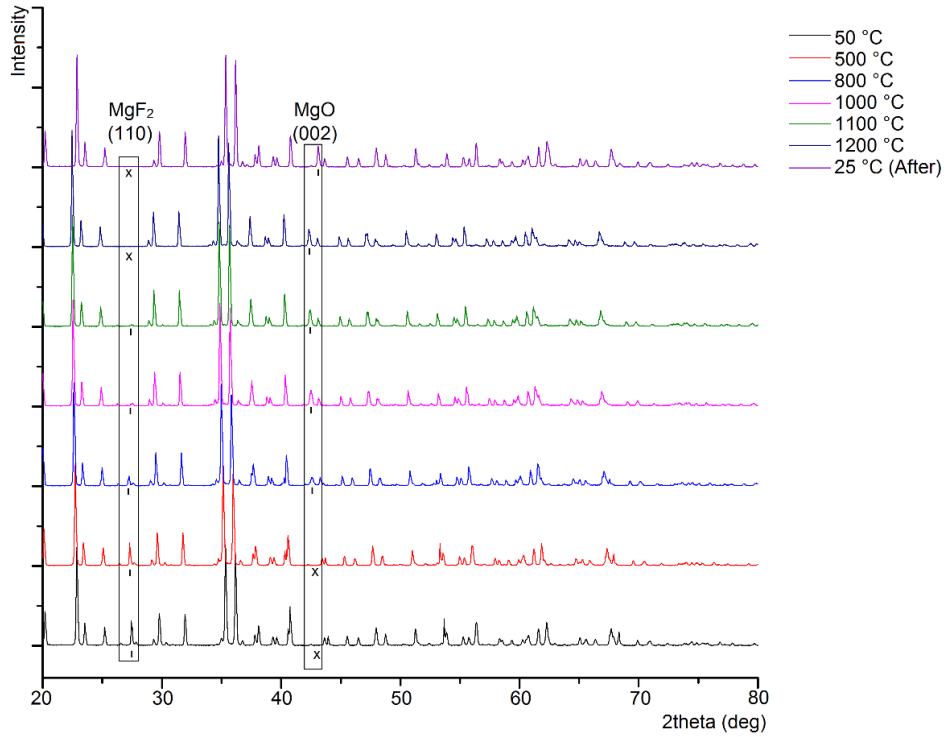

Figure 3.4. The diffraction data from the heating of Mg_2GeO_4 and MgF_2 in the 1:1 molar ratio on the Pt strip in air. The decomposition of MgF_2 and the formation of MgO can be seen. The 25 °C measurement (top) was done after the system cooled down from 1200 °C.

3.4. Conclusions

The structures of new magnesium fluorogermanates, $Mg_3Ge_{1-\delta}O_{4(1-\delta)}F_{2(1+2\delta)}$ (**1**) and $Mg_2Pb_2Ge_2O_7F_2$ (**3**), were determined from the crystalline products of solid-state reaction and flux growth. These structures relate to the two different groups of silicate minerals. The refinement of the twined $Mg_{14}Ge_4O_{40}F_4$ (**2**) crystal showed the Ge deficiency driven by the substitution of F for O atoms. A similar deficiency is observed in $Mg_3Ge_{1-\delta}O_{4(1-\delta)}F_{2(1+2\delta)}$ (**1**). HT XRD diffraction data confirmed the conversion of MgF_2 into MgO in air at high temperatures and, thus, clarified our inability to prepare $Mg_3Ge_{1-\delta}O_{4(1-\delta)}F_{2(1+2\delta)}$ (**1**) from Mg_2GeO_4 and MgF_2 in open crucibles.

3.5 Supplementary information

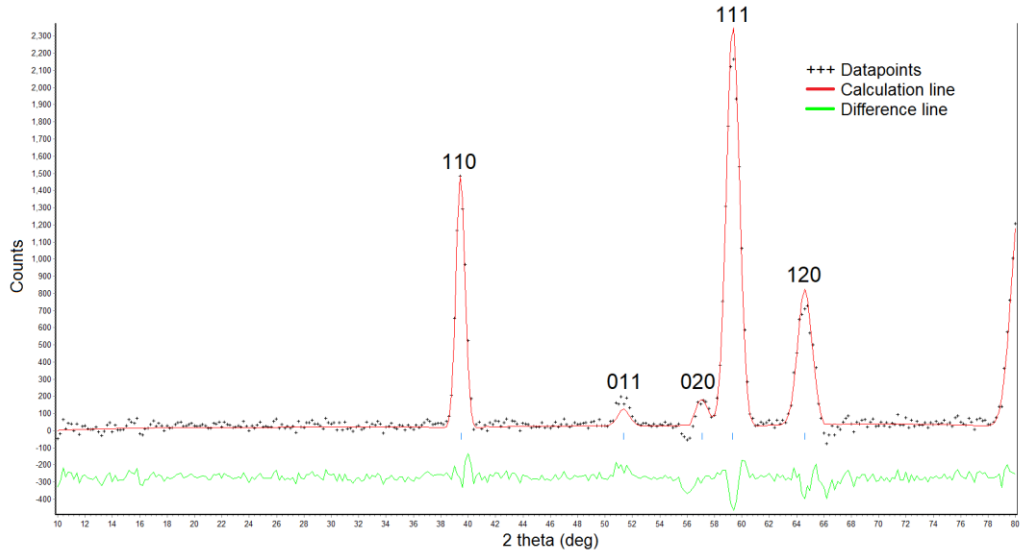

Figure 3.5. The Rietveld refinement of the MgF_2 neutron scattering data. R_p = 15.4 %

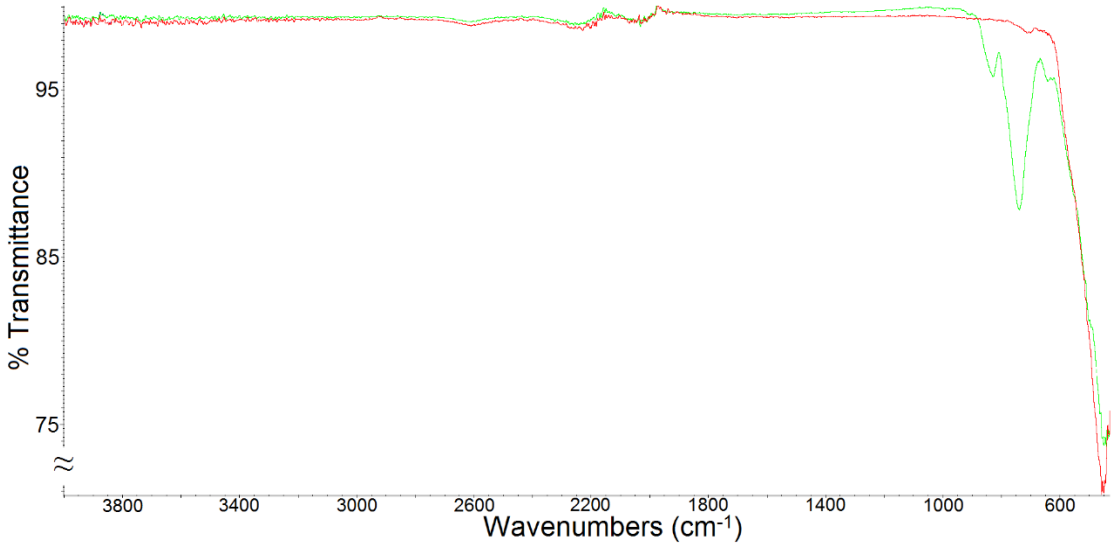

Figure 3.6. The IR spectra of MgF_2 (red) and the solid state reaction product (green). The product contains $Mg_3GeO_4F_2$ (89.9(7) wt. %), MgF_2 (6.4(1) wt. %) and $Mg_{14}Ge_4O_{20}F_4$ (4.6(1) wt. %). Absence of peaks in the characteristic region of the $\nu(H_2O)$ vibrations (at ~ 3615, 4350, and 1640 cm^{-1} for $\nu3$, $\nu1$, and $\nu2$ respectively) indicates the absence of the OH^- group in the structure.

Table 3.2. Fractional atomic coordinates and equivalent isotropic displacement parameters for $Mg_3Ge_{1-\delta}O_{4(1-\delta)}F_{2(1+2\delta)}$ prepared by the solid state route. U_{eq} is defined as 1/3 of the trace of the orthogonalised U_{ij} tensor. The O and F sites were assumed to be occupied only by O and F atoms, respectively.

Atom	**Occupancy**	***x***	***y***	***z***	**U_{eq}**
Ge	0.860(3)	0.72082(3)	1/4	0.07047(7)	0.00538(9)
Mg1	1	0.63136(6)	0.43013(8)	0.5054(1)	0.0077(2)
Mg2	1	0.40608(9)	1/4	0.9930(2)	0.0072(2)
F1	1	0.4664(1)	0.4132(1)	0.7217(3)	0.0105(2)
O1	1	0.7943(1)	0.4039(2)	0.2407(3)	0.0093(3)
O2	1	0.5682(2)	1/4	0.2276(4)	0.0089(4)
O3	1	0.7213(2)	1/4	0.7156(4)	0.0087(3)

Table 3.3. Interatomic distances for the Ge3 surrounding in $Mg_{14}Ge_4O_{20}F_4$.

Atom	**Distance, Å**	**Atom**	**Distance, Å**
O7	1.76(2)	F7	1.91(2)
O8	1.77(1)	F8	2.01(1)
O9	1.70(4)	F9	1.78(3)

Table 3.4. Bond lengths for $Mg_2Pb_2Ge_2O_7F_2$.

Bond	**d, Å**	**Bond**	**d, Å**	**Bond**	**d, Å**
Pb–O1	2.262(5)	Ge–O2	1.769(3)	Mg1–F3	2.018(3)
–O3	2.288(5)	–O3	1.742(4)	–O3(×2)	2.100(5)
–F3	2.455(3)	–O1	1.737(4)	–F3	2.018(3)
–O4	2.625(4)	–O4	1.723(4)	–O4(×2)	2.026(4)
–O2	2.975(4)			Mg2–F3(×2)	2.008(3)
–O1	3.173(5)			–O1(×2)	2.090(5)
–O3	3.246(5)			–O4(×2)	2.075(4)

Chapter 4. New halogen-germanates of Sr and Ba

The following chapter was published as “New halogen-germanates of Sr and Ba” article in Journal of Solid State Chemistry (*J. Solid State Chem.* **2020**, *282*, 121075). The candidate synthesized and characterized new materials, prepared the manuscript for the publication.

Crystals of four novel compounds, $Sr_3GeO_4Cl_2$, $Ba_3GeO_4Br_2$, $Sr_6Ge_2O_7Cl_6$, and $Ba_5GeO_4Br_6$, were obtained through solid state sintering and flux growth. Single crystal X-ray diffraction revealed that $Sr_3GeO_4Cl_2$ and $Ba_3GeO_4Br_2$ are structurally related to $Mg_3SiO_4(F,OH)$ (but not isostructural due to the significant difference in ionic radii). Application of the $RHal_2$ (*R* = Sr, Ba; *Hal*= Cl, Br) fluxes for the crystal growth yielded the $Sr_6Ge_2O_7Cl_6$ and $Ba_5GeO_4Br_6$ phases with higher Ge : *Hal* ratios. Presence of the additional Hal^- anions accounts for the formation of 3D units built from Ba^{2+} and Br^- in $Ba_5GeO_4Br_6$, while in the other germanates the highest dimensionality of the R^{2+} - Hal^- units is 2.

4.1 Introduction

The red part of the visible spectrum is necessary for the production of warm white light in the LEDs. Some of the common red phosphors, based on the Eu^{2+} doped nitrides[52,53], may display performance losses due to their wide excitation regions and broad emission bands. The disadvantages include photon re-absorption, lowering of color purity, and decrease in luminous efficiency[54–58]. The nitride phases also require sophisticated synthesis procedures, such as very high temperatures (above 1500°C) and high pressures of nitrogen[54–58]. Because of this, Mn^{4+}doped materials can be considered as a potential replacement for the rare-earth based red phosphors. These oxides, fluorides, and oxosalts show excellent optical properties and can be prepared by routine synthetic methods[59–65].

Mn^{4+} prefers octahedral sites in a crystal structure and can be doped into the Ge^{4+} sites due to the same charges and ionic radii of both cations (0.67 Å)[19]. However, the octahedral sites are much less common for the tetravalent germanium, compared to the tetrahedral ones[20]. Thus, preparation of new germanate phosphors is based on the prior knowledge of crystal structures. While crystal structures of germanates with GeO_6 polyhedra known for some time, their potential

as Mn^{4+} hosts was investigated only recently. For example, two Mn^{4+}-doped $R^{I}_2Ge_4O_9$ (R^{I} = Li, K, or Rb[66–70]) and $R^{II}Ge_4O_9$ (R^{II} = Sr, Ba[71]) series were characterized lately, and likely, more of the existing germanates can act as red phosphors. On the other hand, the discovery of new Ge^{4+} phases with octahedral sites is a challenging approach. An example of the later approach is the synthesis of $Li_3RbGe_8O_{18}$[63] that features new structural and notable optical luminescent properties.

While predominance of the tetrahedral coordination for Ge limits the number of the phases suitable for the Mn^{4+} doping, it may provide opportunities for doping with other activators. The study on the $Ba_5SiO_4Cl_6$[72] and $Ba_5SiO_4Br_6$[73,74] halogen silicates, showed that both smaller Si tetrahedral sites and larger alkaline-earth sites can serve as activator hosts. The Ba sites can be activated with Eu^{2+}, which produced red emitting phosphor materials sensitive to the UV and X-ray exitation[72,73]. The doping of the silicon sites in $Ba_5SiO_4Br_6$ with Nb yields a photostimulable X-ray storage phosphor[74]. It is worth mentioning that the crystal structures of $Ba_5SiO_4Cl_6$[75] and $Ba_5SiO_4Br_6$[76] were determined after their optical properties were reported. Germanates are often isostructural with silicates, thus the Ge analogues of $Ba_5SiO_4Cl_6$ and $Ba_5SiO_4Br_6$ can display interesting optical properties as well. The Sr halogen germanates can be also be of interest, since the Sr sites are frequently utilized for the rare earth dopants[77–79].

This paper reports on the synthesis and structure of the Sr and Ba halogen germanates. This research originates from our work on the $Mg_{28}Ge_{7.5}O_{38}F_{10}$ material[24]. By using the flux growth method, we obtained crystals of $Mg_3GeO_4F_2$ (to be reported in a separate paper). Motivated by our discovery, we continued the investigation of the $R^{II}CO_3$ – $R^{II}Hal_2$ – GeO_2 (R = Sr, Ba; Hal = Cl, Br) systems and obtained four new phases, $Sr_3GeO_4Cl_2$ (**1**), $Ba_3GeO_4Br_2$ (**2**), $Sr_6Ge_2O_7Cl_6$ (**3**), and $Ba_5GeO_4Br_6$ (**4**).

4.2 Experimental

4.2.1 Synthesis

Powders of GeO_2 (Alfa Aesar, 99.999 wt.%), $SrCO_3$ (Sigma-Aldrich, ≥99.9 wt.%), $SrCl_2$ (Alfa Aesar, 99.5 wt.%), $BaCO_3$ (Alfa Aesar, 99 wt.%), $BaBr_2 \cdot 2H_2O$ (Alfa Aesar, 99.3 wt.%) were used as received. Crystals of $Sr_3GeO_4Cl_2$ (**1**) were obtained by a solid state reaction between $SrCO_3$ (0.2924 g), GeO_2 (0.1036 g), and $SrCl_2$ (0.1570 g) in the 2 : 1 : 1 molar ratio. Reagents were mixed in an agate mortar and placed in a Pt crucible. Then, the crucible with reagent was placed in programmable box furnace at room temperature and heated at 150 °/h to 1000 °C. After 14 hours, the furnace was cooled down to 800 °C at 6 °/h rate. The cooling to room temperature was done by switching off the furnace at 800 °C.

Crystals of $Ba_3GeO_4Br_2$ (**2**) and $Ba_5GeO_4Br_6$ (**4**) formed as a mixture during the reaction between $BaCO_3$ (0.4044 g), GeO_2 (0.1072 g), and $BaBr_2 \cdot 2H_2O$ (0.3414 g) with the 2 : 1 : 1 molar ratio, which was heated at 150°/h to 950°C. After 12 hours at 950°C, the furnace was cooled down to 800 °C at 6 °/h rate and then switched off.

$Sr_6Ge_2O_7Cl_6$ (**3**) was obtained from the reaction between $SrCO_3$ (0.2878 g) and GeO_2 (0.1020 g) with the 2:1 molar ratio. $SrCl_2$ (0.9850 g) was used as a flux. A crucible with the reagents was kept at 200 °C for 6 hours, then heated at 150 °/h rate to 1000 °C and annealed for 30 hours. After this the furnace was cooled down to 800 °C at 6 °/h, and then to room temperature by switching off.

4.2.2 Crystal structure determination

Single crystal X-ray diffraction was employed for the structure determination. The data for **1-4** were collected on a STOE IPDS II diffractometer (Mo Kα radiation) at room temperature. Structures of new germanates were solved by direct methods[41] and refined by full-matrix least

squares calculations against F^2 in an anisotropic approximation[42,43]. Numerical absorption correction was based on the crystals shapes. The shapes were determined optically from face indexing followed by optimization against equivalent reflections using the X-Shape software[39]. The crystal of $Ba_3GeO_4Br_2$ (**2**) was a twin, with two components related by the [-1 0 0, 0 -1 0, 0 0 1] law. The fractions of twin components were 68 and 32%. The crystal of $Sr_6Ge_2O_7Cl_6$ (**3**) had a second, randomly oriented component; as a result the refinement of **3** gave larger residual values. Relevant crystallographic information for **1-4** is summarized in Table 4.1.

Table 4.1. Selected crystallographic data and parameters of XRD experiments for $Sr_3GeO_4Cl_2$ (**1**), $Ba_3GeO_4Br_2$ (**2**), $Sr_6Ge_2O_7Cl_6$ (**3**), and $Ba_5GeO_4Br_6$ (**4**)

Compound	$Sr_3GeO_4Cl_2$ (**1**)	$Ba_3GeO_4Br_2$ (**2**)	$Sr_6Ge_2O_7Cl_6$ (**3**)	$Ba_5GeO_4Br_6$ (**4**)
Formula weight	470.35	708.43	995.60	1302.75
Space group	*Pnma*	$P2_1/c$	*Pbcm*	$C2/c$
a (Å)	12.279(3)	6.6992(13)	8.0348(16)	9.792(2)
b (Å)	10.997(2)	11.544(2)	22.731(5)	15.214(3)
c (Å)	5.8489(12)	12.003(2)	9.3876(19)	12.153(2)
β, (°)	-	90.26(3)	-	104.60(3)
V (Å^3)	789.8(3)	928.3(3)	1714.5(6)	1752.0(6)
Z	4	4	4	4
D_{calcd}/g cm^{-3}	3.956	5.069	3.857	4.939
μ (mm^{-1})	24.547	24.330	22.923	26.429
F(000)	848	1208	1800	2216
θ range (°)	3.32- 34.71	3.04-33.49	2.69-32.50	3.19-34.76
Reflections collected/ independent	8612 / 1770	13608 / 3640	16003 / 3261	10180 / 3770
R_{int}	0.1210	0.0848	0.1321	0.0621
R_1 ($I > 2\sigma(I)$)	0.0621	0.0488	0.0802	0.0348
Largest difference peak/hole (e/Å^3)	1.707/- 2.244	1.920 / -2.040	3.240 / -3.290	1.634/-1.496

4.2.3 Powder X-ray diffraction

Powder data for **1-4** were collected on a PANalytical X'Pert PRO diffractometer in the 20-

80° 2θ range and with the CuKα_1 radiation (see Supplementary Information). The Rietveld refinement was done with the Rietica software[44]. For **1**, the product was a mixture of well crystallized $Sr_3GeO_4Cl_2$ (**1**) (55.1(4) wt. %) and Sr_2GeO_4 (44.9(4) wt. %). For **2**, the reaction contains mostly $Ba_3GeO_4Br_2$ (**2**) (80.1(2) wt. %) with some $Ba_5GeO_4Br_6$ (**4**) (4.40(1) wt. %) and Ba_2GeO_4 (15.5(3) wt. %). Note, that the ICSD does not have any entries for the Ba_2GeO_4 structure. The crystals of Ba_2GeO_4 were obtained as a side product. The structural data for Ba_2GeO_4 is included in the Supplementary Information.

For **3**, the powder XRD showed the presence of $Sr_6Ge_2O_7Cl_6$ (**3**), Sr_2GeO_4, and some unknown impurity. This sample is characterized by the low intensity of diffraction peaks making the refinement somewhat unreliable. The refinement gave the following composition: 76(2) wt. % of $Sr_6Ge_2O_7Cl_6$ (**3**) and 23(1) wt. % of Sr_2GeO_4.

4.3. Results and Discussion

4.3.1 Crystal structures

*$Sr_3GeO_4Cl_2$ (**1**) and $Ba_3GeO_4Br_2$ (**2**)*

The $Sr_3GeO_4Cl_2$ (**1**) structure contains two independent Sr atoms: Sr1 in the 4*c* position and Sr2 in the general 8*d* position. Coordination polyhedra for Sr are trigonal prisms $Sr1O_4Cl_2$ and capped trigonal prisms $Sr2O_4Cl_3$. The prisms are distorted due to the differences in the Sr-O and Sr-Cl bond lengths. The sole germanium atom in **1** occupies the 4*c* position and forms GeO_4 tetrahedra. Each of these tetrahedra connects eight Sr atoms. The 3D structure of **1** is formed by the corner and edge-sharing of $Sr1O_4Cl_2$, $Sr2O_4Cl_3$, and GeO_4 polyhedra. We can imagine the formation of this framework as following: $(Sr2Cl)_\infty$ layers parallel to the *ac* plane are linked by GeO_4 tetrahedra in the *b* direction giving a 3D unit, and Sr1 atoms are embedded into the residual voids (Figure 4.1).

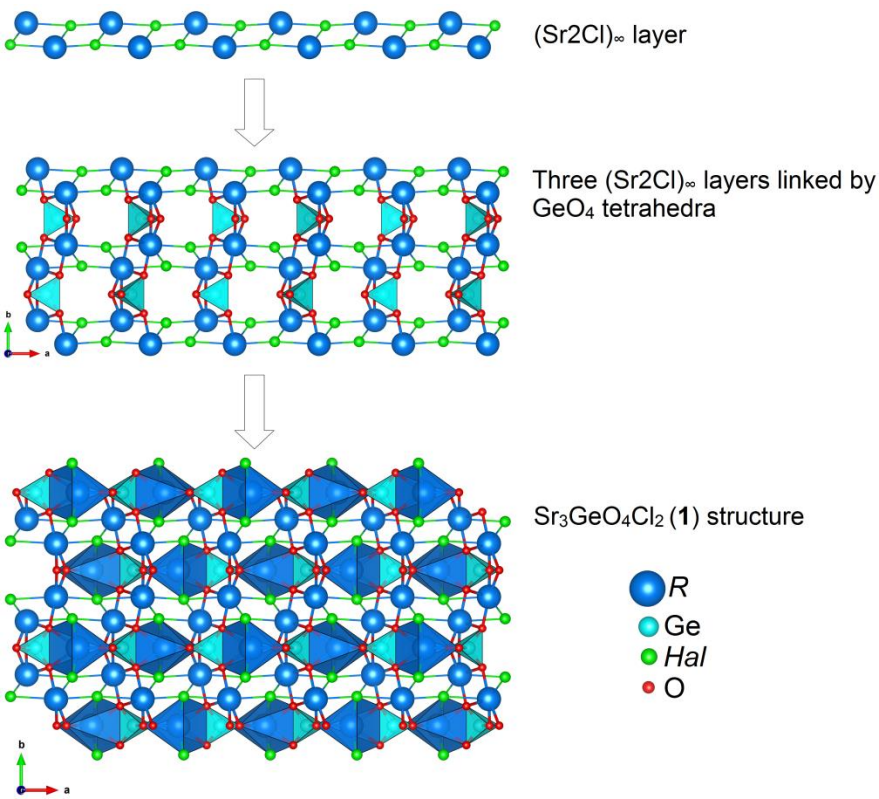

Figure 4.1. Schematic representation of $Sr_3GeO_4Cl_2$ (**1**) framework formation: $(Sr2Cl)_\infty$ layers (top) are connected in 3D unit (middle) by GeO_4, and then the residual volume is filled by Sr1 (bottom). Hereinafter, alkaline earth atoms and their polyhedra are blue, Ge polyhedra are cyan, oxygen atoms are red, and halogen atoms are green.

The $Ba_3GeO_4Br_2$ (**2**) structure contains the following coordination polyhedra: $Ba1O_4Br_5$, $Ba2O_4Br_5$, $Ba3O_4Br_3$, and $Ge1O_4$. The formation of **2** can be described in a similar manner as **1**, however the lower symmetry of **2** makes this description more complex. In **2**, Ba1 atoms and both Br atoms form infinite layers parallel to *bc*. The other two Ba atoms are connected by bromine into chains running along *a*. The intersection of these layers and chains creates a 3D framework, additionally connected by GeO_4 polyhedra (Figure 4.2).

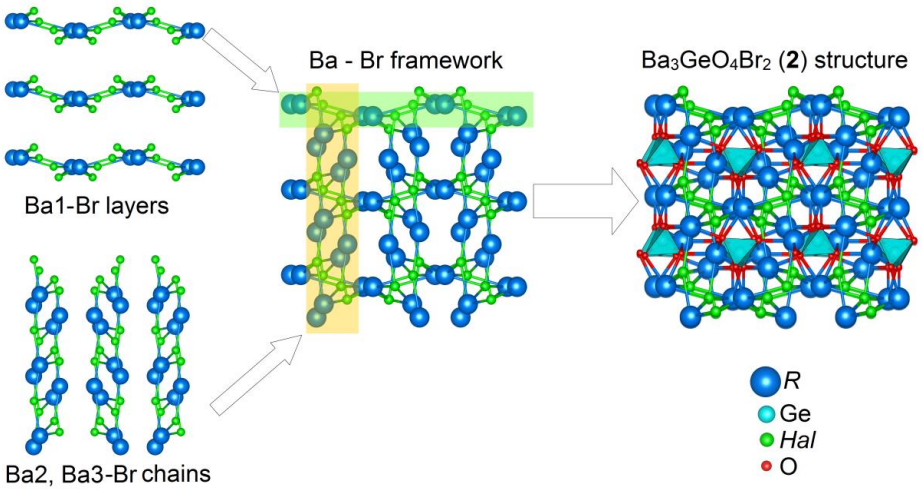

Figure 4.2. Schematic representation of the $Ba_3GeO_4Br_2$ (**2**) formation (*ab* projection): 2D and 1D Ba-Br units form a 3D framework, with further connections by GeO_4 tetrahedra.

Compounds **1** and **2** are structurally related to the magnesium silicate mineral, norbergite, $Mg_3SiO_4(F,OH)$[80]. Along with the $Ca_3GeO_4Cl_2$[81] structure, **1** and **2** form a family of the $R_3GeO_4Hal_2$ halogen germanates. However, an increase in ionic radii leads to the inability of the structures to adopt the $Mg_3SiO_4(F,OH)$ atomic arrangement. The coordination numbers of the R^{2+} cations increase from 6 in $Mg_3SiO_4(F,OH)$ to 9 in $Ba_3GeO_4Br_2$. Moreover, $Ba_3GeO_4Br_2$ (**5**) crystals are monoclinic, while the rest in the series are orthorhombic.

*$Sr_6Ge_2O_7Cl_6$ (**3**)*

There are four independent Sr atoms in the structure. Their coordination polyhedra are $Sr1O_2Cl_6$, $Sr2O_3Cl_5$, $Sr3O_4Cl_3$, and $Sr4O_4Cl_5$. Phase **3** is a digermanate: two GeO_4 tetrahedra share one vertex to form Ge_2O_7 units. Connectivity with Cl atoms differs drastically between the four Sr atoms (Figure 4.3). The Sr1 atoms are linked by chlorine into infinite chains parallel to *c*, Sr2 atoms form 0D units with Cl, Sr3 atoms - linked into layers parallel to the *bc* plane, and Sr4 - into layers parallel to the *ac* plane. Together these various 0D-2D units form an infinite framework completed by digermanate anions (Figure 4.3).

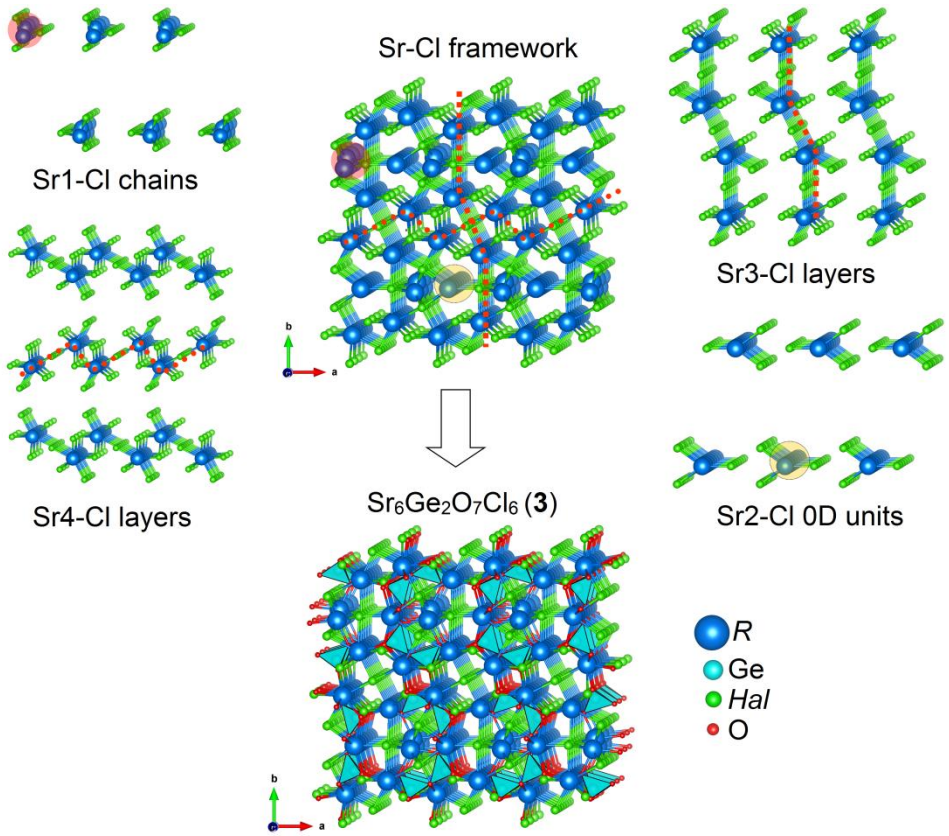

Figure 4.3. 0D - 2D units Sr-Cl units forming a 3D framework in $Sr_6Ge_2O_7Cl_6$ (**3**). (bottom) The fragment (3×1×3 unit cells) of the $Sr_6Ge_2O_7Cl_6$ (**3**) crystal structure (*ab* projection).

*$Ba_5GeO_4Br_6$ (**4**)*

There are three independent Ba atoms in the structure: Ba1 and Ba3 in the *8f* general positions, and Ba2 in the *4e* position. Their coordination polyhedra are $Ba1O_2Br_7$, $Ba2O_2Br_6$, and $Ba3O_3Br_6$. Here, Br atoms link the Ba2 atoms into chains parallel to the [101] direction, while both Ba1 and Ba3 are linked into infinite frameworks (Figure 4.4). The interlacement of these 0D and 3D units generates a complex Ba-Br framework (Figure 4.5).

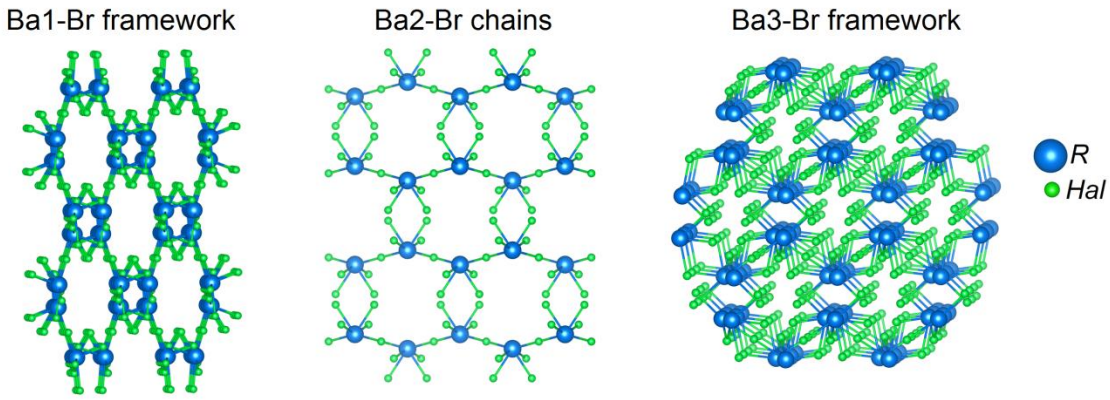

Figure 4.4. 1D and 3D Ba-Br units in $Ba_5GeO_4Br_6$ (**4**).

The *Hal* : Ge ratio in **4** is the highest among the four new compounds and the GeO_4 polyheda are separated from each other in this structure (Figure 4.5). $Ba_5GeO_4Br_6$ (**4**) is isostructural with $Ba_5SiO_4Cl_6$[72] and $Ba_5SiO_4Br_6$[73,74]

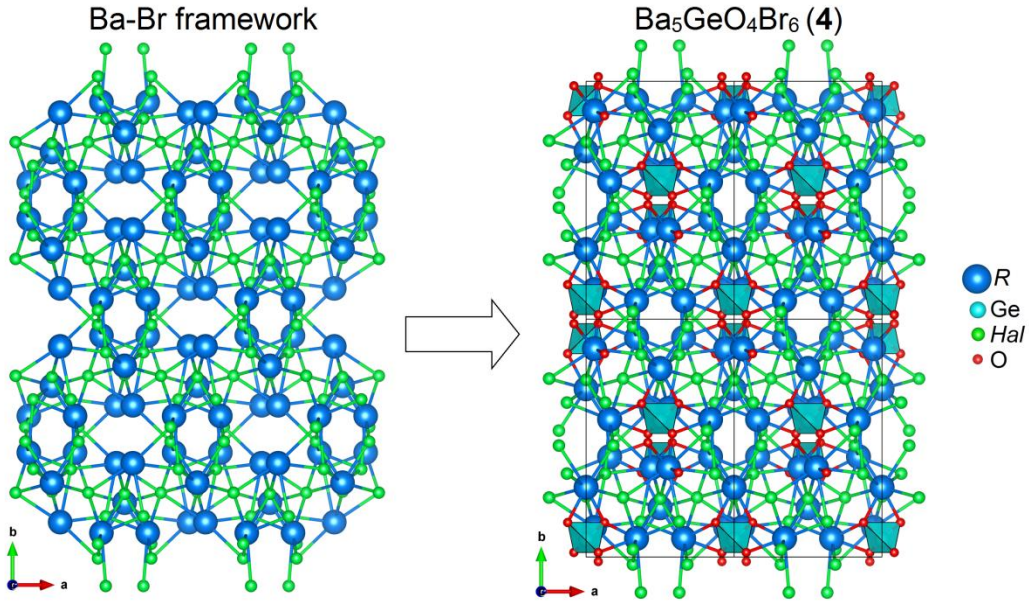

Figure 4.5. (left) Ba-Br framework in $Ba_5GeO_4Br_6$ (**4**). (right) $Ba_5GeO_4Br_6$ (**4**) structure (2×2×1 unit cells) projected on *ab* plane (right).

4.3.2 Topology of R^{2+}- Hal (R^{2+} = Ca-Ba, Hal = F-Br) nets in halogen germanates

A number of the 2D units built from the R^{2+} cations and Hal^{-} anions can be found in $Ca_3GeO_4Cl_2$[81], $Sr_3GeO_4Cl_2$ (**1**), and $Ba_3GeO_4Br_2$ (**2**) structures. These units can be considered as building blocks of the halogen germanate structures. However, the *R-Hal* 2D units, or layers, have different compositions and levels of distortion, and thus the comparison of the corresponding structures may be difficult. To overcome this challenge, we can focus on the topology of units, rather than their geometry or stoichiometry. For the topological analysis presented below, we used the ToposPro[82] program package. Briefly, the algorithm allows the calculations of the connectivity between central cations (R^{2+} in our case) and ligands (Hal^{-}) of 2D or 3D units (nets). Typically, cations become the nodes of the net. The bonds between the nodes represent the connectivity between cations by anions. The representation of anions depends on their coordination in the R^{2+}-*Hal* units. The crucial cases for the R^{2+}- *Hal* nets are shown in Figure 4.6. It has to be mentioned that the chemical compositions of the structures under consideration may be different as only the *R-Hal* bonds are taken into account while the *R*-O bonds are omitted.

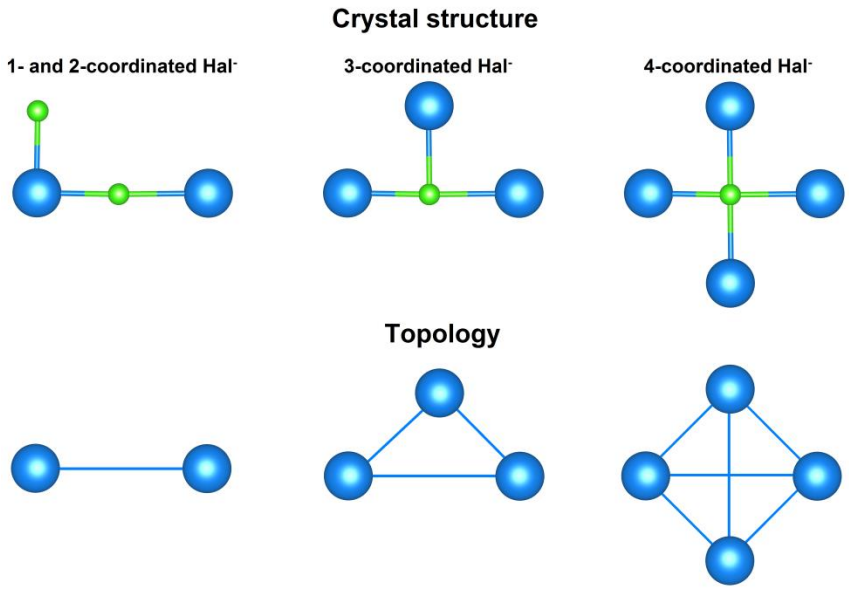

Figure 4.6. The transformation of two-, three-, and four coordinated Hal^{-} ligands in the topological analysis of R^{2+}- *Hal* nets.

All three structures, $Ca_3GeO_4Cl_2$[81], $Sr_3GeO_4Cl_2$ (**1**), and $Ba_3GeO_4Br_2$ (**2**) contain infinite R^{2+}-*Hal* layers with the topology of the *tts* net (Figure 4.7). Hereinafter, the three letter symbols[83] are used as net names. In the $R_3GeO_4Hal_2$ series, these *tts* nets are connected into 3D units by germanate anions as described above. Note that for $Ba_3GeO_4Br_2$ (**2**) the stoichiometry of the *R-Hal* net is different due to higher coordination numbers of Ba atoms, however the topology remains the same.

Other types of the R^{2+}-*Hal* layers can be found in $Sr_6Ge_2O_7Cl_6$ (**3**): for Sr3, a *hcb* (honeycomb or brick wall) net is formed (Figure 4.7), while Sr4 atoms are linked into a *sql* (square lattice) net by chlorine. In the crystal structure the *hcb* and *sql* nets share chlorine atoms. This yields a 3D framework from the 2D nets.

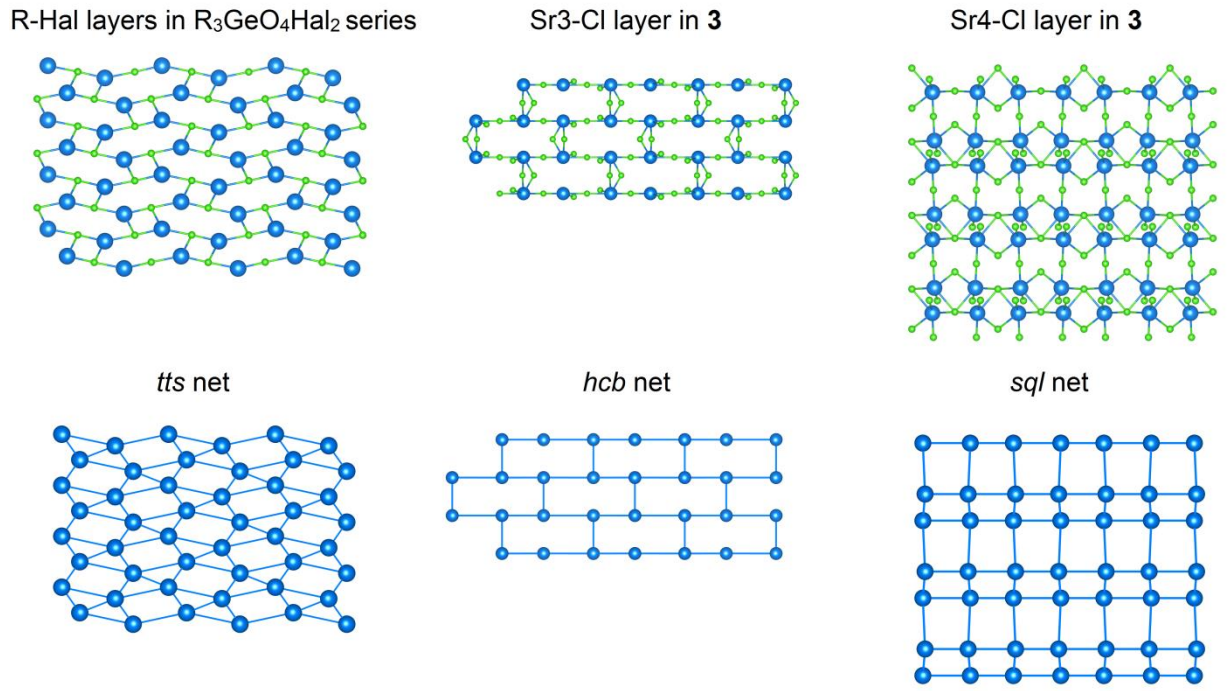

Figure 4.7. The topology of 2D R^{2+}-*Hal* nets in the halogen germanates.

The same approach can be applied for 3D units as well. For example, Ba1 atoms in $Ba_5GeO_4Br_6$ (**4**) form a *sra* ($SrAl_2$) net with Br, while Ba3 – a *lon* (lonsdaleite, 'hexagonal

diamond') net (Figure 4.8). Two frameworks are embedded into each other, but due to the presence of the shared Br anions in $Ba_5GeO_4Br_6$ (**4**), their combination cannot be considered as an interpenetration. The arrangement of two frameworks is shown in Figure 4.8.

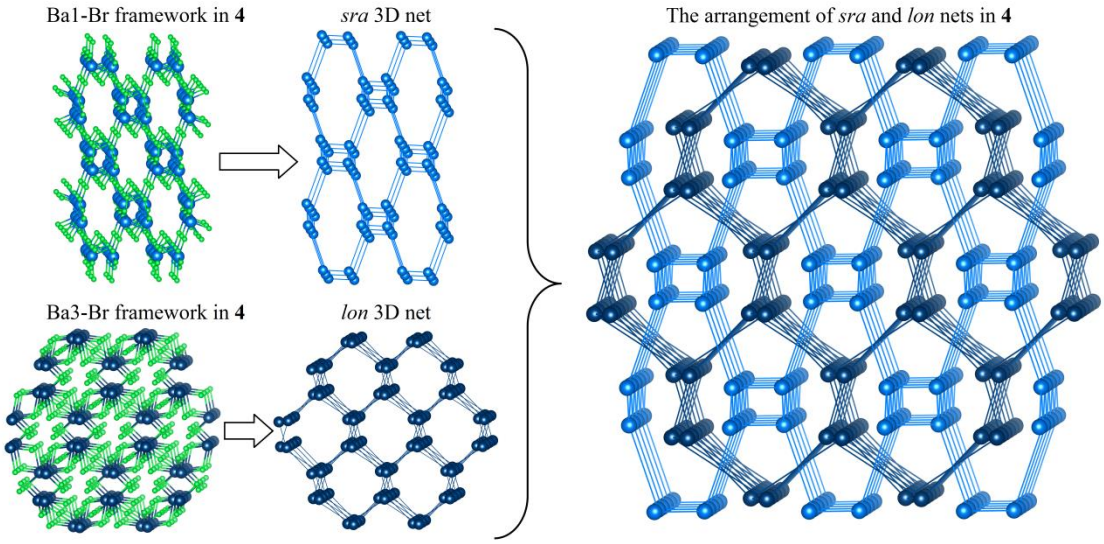

Figure 4.8. The topology of 3D R^{2+}-*Hal* nets in the $Ba_5GeO_4Br_6$ (**4**). Ba3 atoms are shown in dark blue. The bonds between *sra* and *lon nets* are omitted for clarity.

The topological analysis revealed significant structural difference between new halogen-germanates. The increase in the *Hal* content in **1-4** accounts for the increase in the variety and dimensionality of the *R-Hal* units in their structures. For **1** and **2**, only a *tts* type of 2D nets is presented; while more complex structures **3** and **4** contain 2 types of 2D (*hcb* + *sql*) and 3D (*sra* + *lon*) nets, respectively. As we can see, simple ions can be connected in sophisticated ways; and the topological analysis provides a comparative and sufficient description of the corresponding structures.

4.4 Conclusions

Four new halogen germanates of Sr and Ba were successfully synthesized and characterized by single crystal and powder X-ray diffraction. The structures of this new series

feature high R^{2+} : Ge ratios (3:1 and 5:1). Potentially, more representatives of the series can be obtained by varying the GeO_2 : $RHal_2$ ratio during the synthesis. Unfortunately, the tetrahedral coordination of Ge atoms makes these new compounds unsuitable for the Mn^{4+} doping and phosphor applications. Additionally, the phosphors are usually found among the compounds with the R^{2+} : Ge ratios being lower than one.

Chapter 5. Synthesis and structure of the Na-Ba and Rb-Ba octagermanates and phosphorescence of the $Rb_2BaGe_{8-x}O_{18}:xMn^{4+}$ series

The following chapter was published as "Synthesis and structure of the Na-Ba and Rb-Ba octagermanates and phosphorescence of the $Rb_2BaGe_{8-x}O_{18}:xMn^{4+}$ series" article in Journal of Solid State Chemistry (*J. Solid State Chem.* **2021**, *304*, 122607). The candidate synthesized and characterized new materials and prepared the manuscript for the publication.

Structures of two new phases, $Na_2BaGe_8O_{18}$ (**1**) and $Rb_2BaGe_8O_{18}$ (**2**), were determined by single crystal X-ray diffraction. The phases are isostructural and crystallize with the $P\bar{3}c1$ space group. The new octagermanates are built from the 3D anionic germanate frameworks, with alkali and alkaline earth cations located in their channels. The frameworks are made by corner-sharing GeO_4 and GeO_6 polyhedra. The way the GeO_n polyhedra are connected in $Na_2BaGe_8O_{18}$ (**1**) and $Rb_2BaGe_8O_{18}$ (**2**) demonstrates a specific topology different from the related compounds. The partial doping of the octahedral Ge sites in $Rb_2BaGe_8O_{18}$ (**2**) with Mn^{4+} yielded a series of red-emitting phosphors. The photoluminescent data for these phosphors were collected and the highest phosphorescence intensity was found in the $Rb_2BaGe_{7.995}O_{18}$: $0.005Mn^{4+}$ sample.

5.1 Introduction

Light-emitting diodes (LEDs) are a better alternative to incandescent and fluorescent lamps for the household and industrial applications. LEDs require less energy to operate, possess longer lifetimes, and are more environmentally friendly[84,85]. In 2001, Bergh et al. reported "20 % of electricity is used for lighting"[86] and predicted a significant decrease of that number by 2020 due to the development of the solid-state light sources. As we can see, in 2020 the lighting contributed only 4.1 % to the total energy consumption in the United States[87], thus the prediction was correct.

One of the ongoing challenges for the LED technology is a production of a white light (w-LED). White light can be achieved either by a combination of a few LEDs (for example, red, green, and blue ones) or down conversion of a short wavelength light by a few phosphors in one device, known as phosphor-converted (PC) LED[84]. The very common commercial phosphor-converted scheme for w-LED is based on the blue emitting indium-gallium nitride chip[88] and the Ce^{3+}-doped yttrium aluminium garnet yellow phosphor[15]. This highly efficient scheme suffers from a poor

color rendering index and a high correlated color temperature, since the red component is completely missing[89,90]. In exchange of some efficiency losses, the w-LED performance can be improved by an addition of a red phosphor. Such phosphors can be based on the Eu^{2+} doped materials – nitrides and oxonitrides[52–54,56,57]. On the other hand, the complex preparation procedures and unsatisfactory properties of many Eu^{2+}-based phosphors encouraged the search for rare-earth-free alternatives. For example, red luminescent materials containing Mn^{4+} were studied extensively in the past decade[91,92,65]. These phases can be divided in two large groups – oxides and fluorides. The red emission peak originating from a spin and parity-forbidden $^2E_{2g} \rightarrow {}^4A_{2g}$ electron transition of Mn^{4+} typically lies in a shorter wavelength region for the fluoride materials compared to the oxide ones. It is related to the covalency of the corresponding Mn^{4+} bonds in the host structure – a more ionic fluoride surrounding accounts for the larger energy difference between the exited and ground states[65,91]. The detailed description of the Mn^{4+} optical properties can be found elsewhere[2,91,93,94].

To prepare a red-emitting phosphor, Mn^{4+} activator cations are doped into the host structure. Mn^{4+} ions with a d^3 electron configuration require an octahedral surrounding, so the knowledge of the host structure is crucial for the successful synthesis. Octahedral coordination is very common in inorganic solids, and octahedrally-coordinated atoms such as Al, Ge, Sn, Ti, Zr, etc. can be partially replaced by Mn^{4+}. In particular, the doping of the germanate phases is favorable due to the same formal charge of Ge^{4+} and Mn^{4+} and the same ionic radii [19]. Historically, the first attempts to produce Mn^{4+} red phosphors can be traced to the $MgO – GeO_2$ system[36]. Two efficient phosphors, commonly (yet inaccurately) referred to as $4MgO–GeO_2 : Mn^{4+}$ and $3.5MgO–0.5MgF_2–GeO_2 : Mn^{4+}$ [21,22], were prepared. However, their properties could not be fully explained until their structures were solved a few decades later[23,24,95].

Since the octahedral coordination for germanium is not very common in the oxides [20], the choice of the suitable host structures is rather narrow. Red phosphors were prepared from the alkali and alkaline-earth tetragermanates, $R_2Ge_4O_9$ (R = Li – K)[66,67,96,97] and MGe_4O_9 (M = Sr, Ba)[71], where both octahedral and tetrahedral coordination of Ge occurs. Another series of the $R^{(I)}{}_2M^{(II)}Ge_8O_{18}$ germanates, containing alkali and alkaline earth cations was reported [98]. Single crystal X-ray diffraction data were obtained for one compound in the series – $K_2BaGe_8O_{18}$ – and the octahedral oxygen coordination was confirmed for Ge[98]. In the current paper, we report on the crystal structures of two more compounds in the series – $Na_2BaGe_8O_{18}$ (**1**) and $Rb_2BaGe_8O_{18}$ (**2**). These phases demonstrate a unique way of the GeO_4 and GeO_6 polyhedra connection. The octahedral Ge sites in $Rb_2BaGe_8O_{18}$ (**2**) were used to prepare Mn^{4+}-based phosphors. The photoluminescent data were collected and the Mn doping level was optimised.

5.2 Experimental

5.2.1 Single crystal growth

$Na_2BaGe_8O_{18}$ (**1**) crystals were obtained through the reaction of Na_2CO_3 (98 wt.%), $BaCO_3$ (98 wt. %), and GeO_2 (99.999 wt.%) in 1:1:8 molar ratio. The starting materials were ground with agate mortar and pestle, pressed into a pellet, and placed in a platinum crucible. The crucible was placed into a box furnace preheated to 700 °C and heated immediately to 1150 °C at 200 °/h rate. After two hours at 1150 °C furnace was cooled down to 950 °C at 6 °/h rate and further cooling was done by taking a crucible out. $Na_2BaGe_8O_{18}$ (**1**) crystals for X-ray diffraction (XRD) measurements were picked manually from the final product.

Crystals of the $Rb_2BaGe_8O_{18}$ (**2**) phase were obtained from Rb_2CO_3 (99.9 wt.%), $BaCO_3$ (98 wt.%), and GeO_2 (99.999 wt.%) in 1:1:8 molar ratio. The sample pellet was heated in a box

furnace from 700 °C to 1150 °C at 200 °/h rate, kept for 1 h, then cooled down at 10 °/h rate to 1050 °C. Further cooling to 700 °C was done at 200 °/h rate, after which the sample was taken out. After complete cooling, crystals of $Rb_2BaGe_8O_{18}$ (**2**) were picked for the XRD analysis.

5.2.2. Determination of crystal structure by X-ray diffraction

Single crystal XRD data for $Na_2BaGe_8O_{18}$ (**1**) and $Rb_2BaGe_8O_{18}$ (**2**) were collected on a STOE IPDS II diffractometer (MoKα radiation) equipped with an image plate detector at room temperature. The numerical absorption correction was based on the optimization of the crystal shape against equivalent reflections and was performed with the X-Shape software[39]. The structure solutions (SHELXT[28]) and least-square refinements (SHELXL[43]) were run via the OLEX2 interface[42]. The experimental data and refinement results are summarized in Table 5.1.

Table 5.1. Selected crystallographic data and refinement results for $Na_2BaGe_8O_{18}$ (**1**) and $Rb_2BaGe_8O_{18}$ (**2**).

Compound	**1**	**2**
Formula	$Na_2BaGe_8O_{18}$	$Rb_2BaGe_8O_{18}$
Formula weight	1052.04	1177.00
Crystal system	*trigonal*	
Space group	$P\bar{3}c1$	
a, Å	11.4837(16)	11.8400(17)
c, Å	19.162(4)	19.276(4)
Volume, Å^3	2188.4(7)	2340.2(8)
Z	6	
ρ_{calcg}, cm^3	4.79	5.01
μ/mm^{-1}	19.057	23.966
F(000)	2868	3180
θ range, °	2.952 – 32.498	2.113 – 32.495
Index ranges	$-14 \le h \le 17$, $-17 \le k \le 17$, $-24 \le l \le 28$	$-17 \le h \le 17$, $-14 \le k \le 17$, $-29 \le l \le 29$
Reflections collected	20812	32486
Data/restraints/ parameters	134	

GOOF	1.142	1.002
R_1 (I>2σ (I))	0.0617	0.0433
Largest diff. peak/hole, e/Å^3	1.823 / -1.666	1.678 / -1.741

5.2.3 Preparation of the $Rb_2BaGe_8O_{18}$: Mn^{4+} phosphors

The series of the $Rb_2BaGe_{8-x}O_{18}$: xMn^{4+} (x = 0.001, 0.003, 0.005, 0.010) phosphors was prepared through a solid state reaction between the pristine $Rb_2Ge_4O_9$ and Mn^{4+}-doped $BaGe_4O_9$. Manganese acetate, $Mn(CH_3COO)_2(H_2O)_4$ (99.999 wt.%), was used as a Mn^{4+} source. The tetragermanate precursors were prepared from the corresponding carbonates and germanium dioxide. Rubidium and barium tetragermanates in the 1 : 1 molar ratio were mixed in an agate mortar, pressed in a pellet, and annealed in a platinum crucible for 12 h at 900 °C. Arter the first annealing, the powder XRD data showed the presence of the unreacted $BaGe_4O_9$ (≈2 % by mass), so extra $Rb_2Ge_4O_9$ was added and two more rounds of annealing at 900 °C for 12 h were done. After the third annealing, the high purity (> 99%) of the $Rb_2BaGe_8O_{18}$ phase was confirmed by powder XRD on a PANalytical X'Pert PRO diffractometer. The Rietveld refinement[44] results are presented in the Supplementary Information.

We have also attempted to prepare $Rb_2BaGe_{8-x}O_{18}$: xMn^{4+} directly from Rb_2CO_3, $BaCO_3$, GeO_2 and $Mn(CH_3COO)_2(H_2O)_4$. However, two attempts gave poor yields, as witnessed from the Rietveld refinements of the products in the Supplementary Information (Table 5.2, Figure 5.5). Thus, we proceeded with the reaction between $Rb_2Ge_4O_9$ and $BaGe_4O_9$ as it led to the formation of pure $Rb_2BaGe_8O_{18}$ phase.

The preparation of the $Na_2BaGe_8O_{18}$:Mn^{4+} phosphors whether through the reaction between the corresponding carbonates or through the germanates is complicated by the formation of the $Na_4Ge_9O_{20}$ phase with the Na:Ge ratio close to $Na_2Ge_4O_9$. According to the literature[99], the

$Na_2Ge_4O_9$ phase is metastable, thus the attempts to obtain pure $Na_2BaGe_8O_{18}$ and the corresponding phosphors were abandoned.

5.2.4 Phosphorescence measurements

The photoluminescent excitation (PL) and emission (PLE) spectra for the $Rb_2BaGe_{8-x}O_{18}$: xMn^{4+} series were collected on an Agilent Cary Eclipse fluorescence spectrophotometer at room temperature.

5.3 Results and Discussion

5.3.1 Crystal structures of Na-Ba and Rb-Ba octagermanates

$Na_2BaGe_8O_{18}$ (**1**) and $Rb_2BaGe_8O_{18}$ (**2**) are isostructural and crystallize with the same $P\bar{3}c1$ space group. In both compounds, germanium atoms are in the octahedral and tetrahedral oxygen environments. There are four independent, octahedrally coordinated germanium sites in the structure: 2*a*, 2*b* and two 4*d* Wyckoff positions. The site symmetries of these positions are D_3, C_{3i}, and C_3, and they represent the different distortions of the GeO_6 octahedra. Three independent, tetrahedrally-coordinated germanium sites are on the 12*g* general positions. One independent alkali metal atom is in a general position as well, while the alkaline-earth metal occupies the 6*f* site.

GeO_4 polyhedra form Ge_3O_9 rings through corner sharing. The rings are stacked along the *c* axis in the structure. These rings are connected to the GeO_6 units by corner sharing. Each GeO_6 polyhedron connects six Ge_3O_9 rings forming $Ge^oGe^t_{18}O_{54}$ cluster ('o' – octahedral, 't' – tetrahedral, Figure 5.1). In total, the anionic germanate framework contains 20 GeO_6 and 36 GeO_4

polyhedra per unit cell. The voids of the framework are occupied by the alkali and alkaline-earth cations, which compensate for the negative charge of the framework (Figure 5.1).

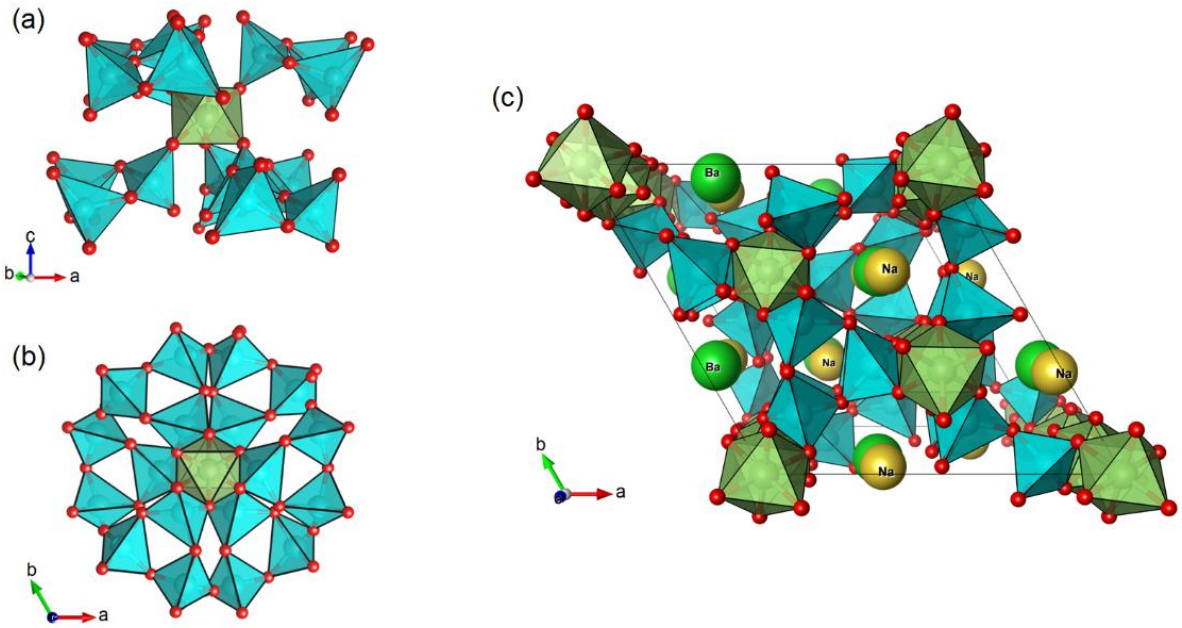

Figure 5.1. (a), (b) A $Ge^{o}Ge^{t}_{18}O_{54}$ cluster in the $Na_2BaGe_8O_{18}$ structure in two projections; (c) the $Na_2BaGe_8O_{18}$ unit cell viewed along the *c* direction. GeO_4 polyhedra are cyan, GeO_6 polyhedra are green, Na atoms are yellow, Ba atoms are green, O atoms are red. Na–O and Ba–O bonds are omitted for clarity.

The crystal structures of $Na_2BaGe_8O_{18}$ (**1**) and $Rb_2BaGe_8O_{18}$ (**2**) display some similarities to those of $Na_2Ge_4O_9$ (or $Rb_2Ge_4O_9$) [100] and $BaGe_4O_9$ [101]. In the octagermanates as well as in the tetragermanates, GeO_4 units are connected in Ge_3O_9 rings and the linkage of these rings by the octahedral GeO_6 units yields a 3D germanate framework. However, a connection of the GeO_4 – GeO_6 polyhedra in the tetra- and ocagermanates is topologically different. The topological analysis was performed with the ToposPro software [82]. The anionic frameworks nets in $Na_2Ge_4O_9$ and $BaGe_4O_9$ belong to the known topological types – *cat* (after mineral catapleiite, $Na_2ZrSi_3O_9{\cdot}2H_2O$

[102], RCSR notation [83]) and *ben* (after mineral benitoite, $BaTiSi_3O_9$[103]), respectively. Interestingly, in the nature the Zr and Ti atoms take on the octahedral Ge sites, while Si the tetrahedral Ge sites of the synthetic tetragermanates. For both Na and Rb octagermante, another topology of the anionic framework net was found (no corresponding RCSR code). The difference in the germanium polyhedra connectivity between *cat*, *ben*, and the $Na_2BaGe_8O_{18}$ (**1**) net types can be seen from the coordination sequences [104] for the Ge^t nodes of the net. For the first five coordination spheres, the sequences are {4, 12, 30, 44, 80} for the *cat* net, {4, 12, 30, 50, 76} for the *ben* net, and {4, 12, 30, 47, 78} for the octagermanate net. Curiously, the coordination sequence for all the octahedral Ge^o nodes is the same in $Na_2Ge_4O_9$, $BaGe_4O_9$, and octagermanates. This sequence – {6, 14, 24, 62, 78} – indicates the formation of the $Ge^oGe^t_{18}O_{54}$ clusters in all structures under consideration (since the first digit in the sequence is 6, and the GeO_6 units do not share corners with each other).

According to the ICSD[25], there are only two compounds isostructural to $Na_2BaGe_8O_{18}$ (**1**) and $Rb_2BaGe_8O_{18}$ (**2**) – $K_2BaGe_8O_{18}$, the first-reported octagermanate [98], and $Cs_3UGe_7O_{18}$ [105]. In $Cs_3UGe_7O_{18}$ [105] two independent pentavalent uranium atoms are in the octahedral coordination and play the same structural role as the octahedrally coordinated Ge atoms in the octagermanates. Another octagermanate compound known to date is $Li_3RbGe_8O_{18}$ – a recently reported Mn^{4+} phosphor [63]. Like in **1** and **2**, there is an anionic framework built from GeO_6 and GeO_4 units in the $Li_3RbGe_8O_{18}$ structure. However, the Li-Rb phase demonstrates significant divergence from the R^+-R^{2+} octagermanate family. It crystallizes with a different space group – $P\bar{3}1m$. The connectivity of the GeO_n polyhedra in $Li_3RbGe_8O_{18}$ is also different from **1** and **2** – GeO_4 units form Ge_6O_{18} rings through a corner sharing. Each GeO_6 octahedron connects six Ge_6O_{18} rings into $Ge^oGe^t_{36}O_{108}$ cluster (Figure 5.2). The corner sharing GeO_n polyhedra in $Li_3RbGe_8O_{18}$ yield an infinite anionic

framework with the *fsb* type of the underlying net. The coordination sequences for the Ge^{o} and Ge^{t} nodes here are {6, 14, 27, 50, 81} and {4, 14, 29, 50, 75}, respectively.

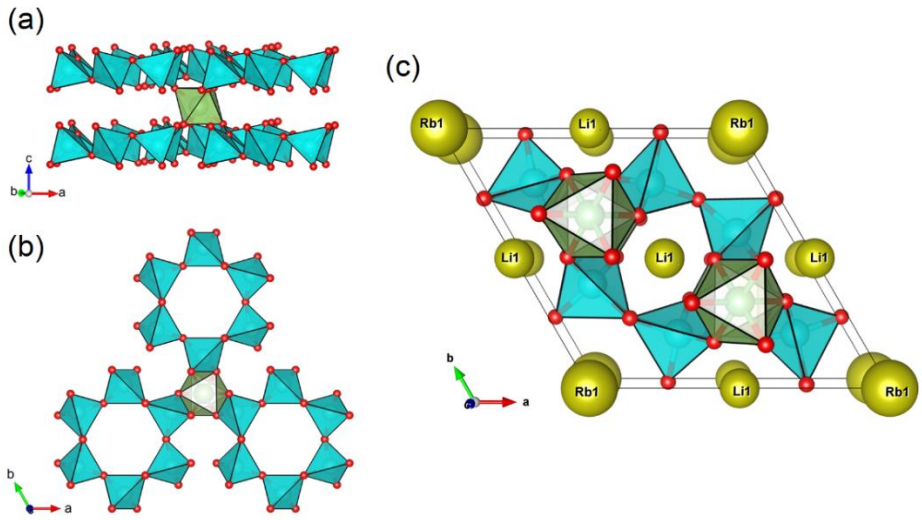

Figure 5.2. (a), (b) A $Ge^{o}Ge^{t}_{36}O_{108}$ cluster in the $Li_3RbGe_8O_{18}$ structure in two projections; (c) the $Li_3RbGe_8O_{18}$ unit cell viewed along the *c* direction. GeO_4 polyhedra are cyan, GeO_6 polyhedra are green, Rb and Li atoms are yellow, O atoms are red. Li–O and Rb–O bonds are omitted for clarity.

As we can see, the stoichiometric resemblance between Na-Ba, Rb-Ba and Li-Rb octagermanates or Na and Ba tetragermanates does not yield the same connectivity of the GeO_n polyhedra. Three types of the nets in the previously reported germanates (*cat* in $Na_2Ge_4O_9$, *ben* in $BaGe_4O_9$, *fsb* in $Li_3RbGe_8O_{18}$) have two unique nodes each (2-nodal net), and the correspondence between the number of the unique nodes and the number of the germanium atoms in the octahedral and tetrahedral oxygen surrounding is apparent. In the simplest case of $Li_3RbGe_8O_{18}$, there is one independent Ge^{t} and one Ge^{o}. For $Na_2Ge_4O_9$ and $BaGe_4O_9$ there are two independent Ge^{o} and two Ge^{t} sites. However, in $Na_2BaGe_8O_{18}$ (**1**), $Rb_2BaGe_8O_{18}$ (**2**), $K_2BaGe_8O_{18}$ and $Cs_3UGe_7O_{18}$ the number of octahedral and tetrahedral sites does not match. The o : t ratio is 4 : 3 in the compounds. The anionic frameworks nets are no longer 2-nodal since an additional unique node appears

(Figure 5.3). The presence of the 3rd node indicates a higher complexity of the anionic frameworks and should account for the larger unit cells in the R^{+}-R^{2+} octagermanates and $Cs_3UGe_7O_{18}$.

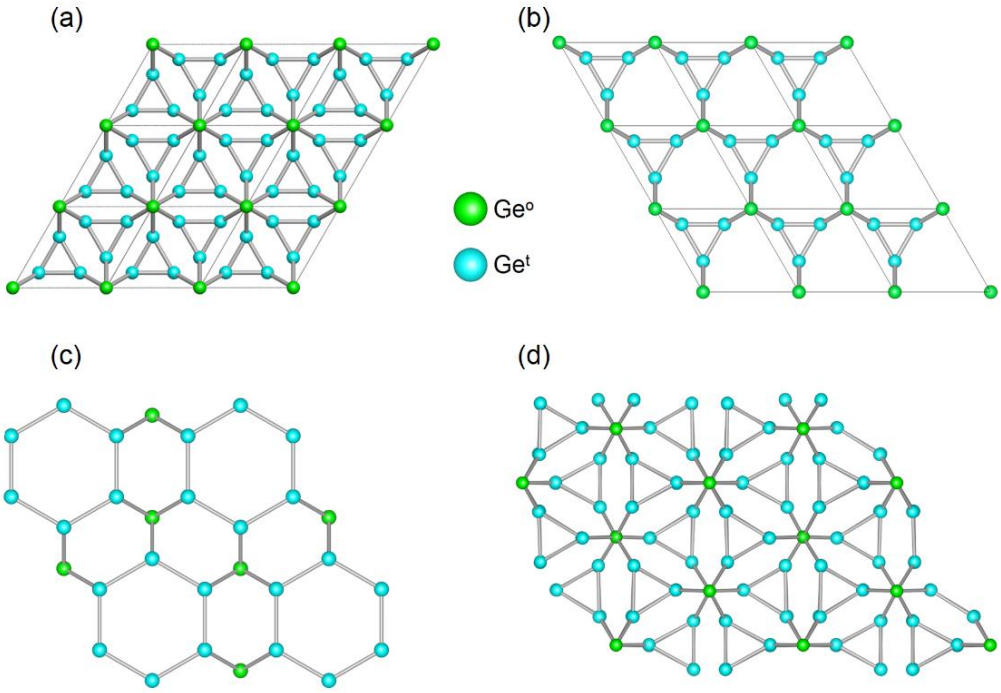

Figure 5.3. The underlying nets of the anionic frameworks in germanates (projections on the *ab* plane): (a) *cat* net in $Na_2Ge_4O_9$; (b) *ben* net in $BaGe_4O_9$; (c) *fsb* net in $Li_3RbGe_8O_{18}$; (d) a new net in $Na_2BaGe_8O_{18}$ and $Rb_2BaGe_8O_{18}$.

5.3.2 Photoluminescent properties of the $Rb_2BaGe_8O_{18}$: Mn^{4+} phosphors

A series of the red emitting $Rb_2BaGe_{8-x}O_{18}$: xMn^{4+} phosphors was prepared by doping the octahedral germanium sites. The PL and PLE spectra of the $Rb_2BaGe_{7.995}O_{18}$: 0.005 Mn^{4+} are shown in Figure 5.4a. The absorption spectrum features two distinguished regions typical for Mn^{4+}. The wide asymmetric peak in the UV region (≈ 300 nm) originates from the 'ligand to metal' charge-transfer band and the spin allowed transitions of the Mn^{4+} cation [106,1,107]. The charge transfer transition has the highest energy (the lowest wavelength). Then the lower energy $^4T_1 \leftarrow {}^4A_2$

(^{4}P) and $^4T_1 \leftarrow {}^4A_2$ (^{4}F) transition follows (all states are 'g') [107]. The exact positions of the peaks are hard to determine due to the overlap. The third spin allowed $^4T_2 \leftarrow {}^4A_2$ transition accounts for the wide absorption peak in the blue region. The position of the peak (470 nm) can be used to estimate the crystal field strength D_q, since $E(^4T_2) = 10Dq$, so $Dq = 2128\ cm^{-1}$ [2].

Under the UV excitation, the emission of the red light with a maximum intensity in the 660-670 nm region occurs. To optimize the Mn^{4+} doping level of the $Rb_2BaGe_8O_{18}$ phase, a $Rb_2BaGe_{8-x}O_{18} : xMn^{4+}$ series (x = 0.001, 0.003, 0.005, 0.010) of phosphors was prepared and their PLE data were collected (Figure 5.4b). Among the samples, the highest intensity of the red emission was found for x = 0.005. The red emission is associated with the spin and parity forbidden $^2E_{2g} \rightarrow {}^4A_{2g}$ relaxation of the Mn^{4+} ion in the octahedral crystal field. As we mentioned above, there are four octahedral sites suitable for the Mn^{4+} doping in the $Rb_2BaGe_8O_{18}$ structure. The presence of the multiple sites with different degrees of distortion complicates the emission spectra. We can see two peaks at 664 and 670 nm persisting through the series (Figure 5.4a). The positions of the peaks (above 645 nm) imply high covalency of the Mn-ligand bonds, which is typical for the oxide hosts[65,94]. The emission of a deep red light limits the application of the oxide based Mn^{4+} phosphors, since a human eye is not sensitive to such long wavelengths. However, the PC LEDs based on these phosphors can be used for the green house plants cultivation.[108,109]

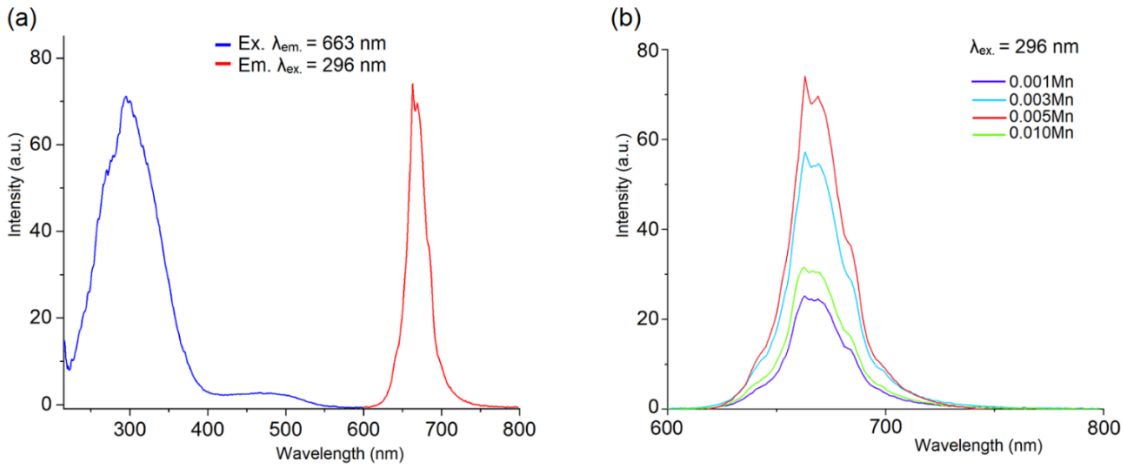

Figure 5.4. (a) PL and PLE spectra of the $Rb_2BaGe_{7.995}O_{18}$: $0.005Mn^{4+}$ sample at room temperature; (b) PLE spectra of the $Rb_2BaGe_{8-x}O_{18}$: xMn^{4+} samples.

The luminescence decays were measured at room temperature and a single exponential fit of the decays was used to determine the decay time (Figure A3.1). The phosphorescence lifetime does not change significantly between the samples, and for the $Rb_2BaGe_{8-x}O_{18}$: xMn^{4+} series the lifetime values are 0.960, 0.953, 0.921 and 1.06 ms for the x = 0.001, 0.003, 0.005, and 0.010, respectively.

5.4 Conclusion

Two new octagermanates – $Na_2BaGe_8O_{18}$ (**1**) and $Rb_2BaGe_8O_{18}$ (**2**) – were synthesized and their structures were characterized with X-ray diffraction. The new phases and the previously reported Na, Rb and Ba tetragermanates share some structural similarities: a trigonal symmetry, the presence of the GeO_4 and GeO_6 polyhedra, the formation of the Ge_3O_9 rings by corner-sharing the GeO_4 units, and the formation of the anionic germanate frameworks. However, the topological analysis revealed a new and more complex way of the GeO_n polyhedra connection in the new phases: the anionic framework net in **1** and **2** has 3 unique vertices (nodes) in contrast to the 2-

nodal nets in $Na_2Ge_4O_9$, $Rb_2Ge_4O_9$ or $BaGe_4O_9$. The higher complexity of the nets in **1** and **2** also distinguish them from other octagermanate – $Li_3RbGe_8O_{18}$.

We produced and studied a series of the red emitting phosphors by the Mn^{4+} doping of the $Rb_2BaGe_8O_{18}$ phase. Typically for the oxide host, the red emission of the Mn^{4+} activator lies in the deep red region (660-670 nm) of the spectra. If the compounds of the R^+-R^{2+} octagermanate family are to be used for the PC LED devises, the choice of the R^+ and R^{2+} should be narrowed to K^+, Sr^+, and Ba^+, since the synthesis of the Na^+ phases is complicated by the formation of a side product, and the Rb^+ derivates would be expensive. The further decrease of a price can be achieved through the synthesis of the zirconate-silicate and titanate-silicate phases isostructural to **1** and **2**.

5.5 Supplementary information

Table 5.2. Two examples of the $Rb_2BaGe_8O_{18}$ synthesis attempts from Rb_2CO_3, $BaCO_3$ and GeO_2.

	Trial 1	Trial 2
Molar ratio of reagents	Rb_2CO_3 : $BaCO_3$: GeO_2. 1 : 1 : 8	Rb_2CO_3 : $BaCO_3$: GeO_2. 2 : 1 : 8
Sample preparation	Powders were mixed in an agate mortar, pressed into pellets, and annealed in a platinum crucible.	
Heating trend	From room temperature to 1050 °C at 100 °/h rate. Dwell for 2 hours. Cool down to 800 °C at 6 °/h rate.	From room temperature to 1000 °C at 100°/h rate. Dwell for 12 hours. Switch off the furnace.
Rietveld refinement data	A mixture of $BaGe_4O_9$ (22.9(4) wt. %) and $Rb_2BaGe_8O_{18}$ (72.9(8) wt. %), traces of $Rb_2Ge_4O_9$ and unknown impurity. Figure S4 (top).	A mixture of $Rb_2Ge_4O_9$ (47.4(7) wt. %) and $Rb_2BaGe_8O_{18}$ (48.6(8) wt. %), traces of GeO_2, $BaGe_4O_9$ and unknown amorphous phase. Figure S4 (bottom).

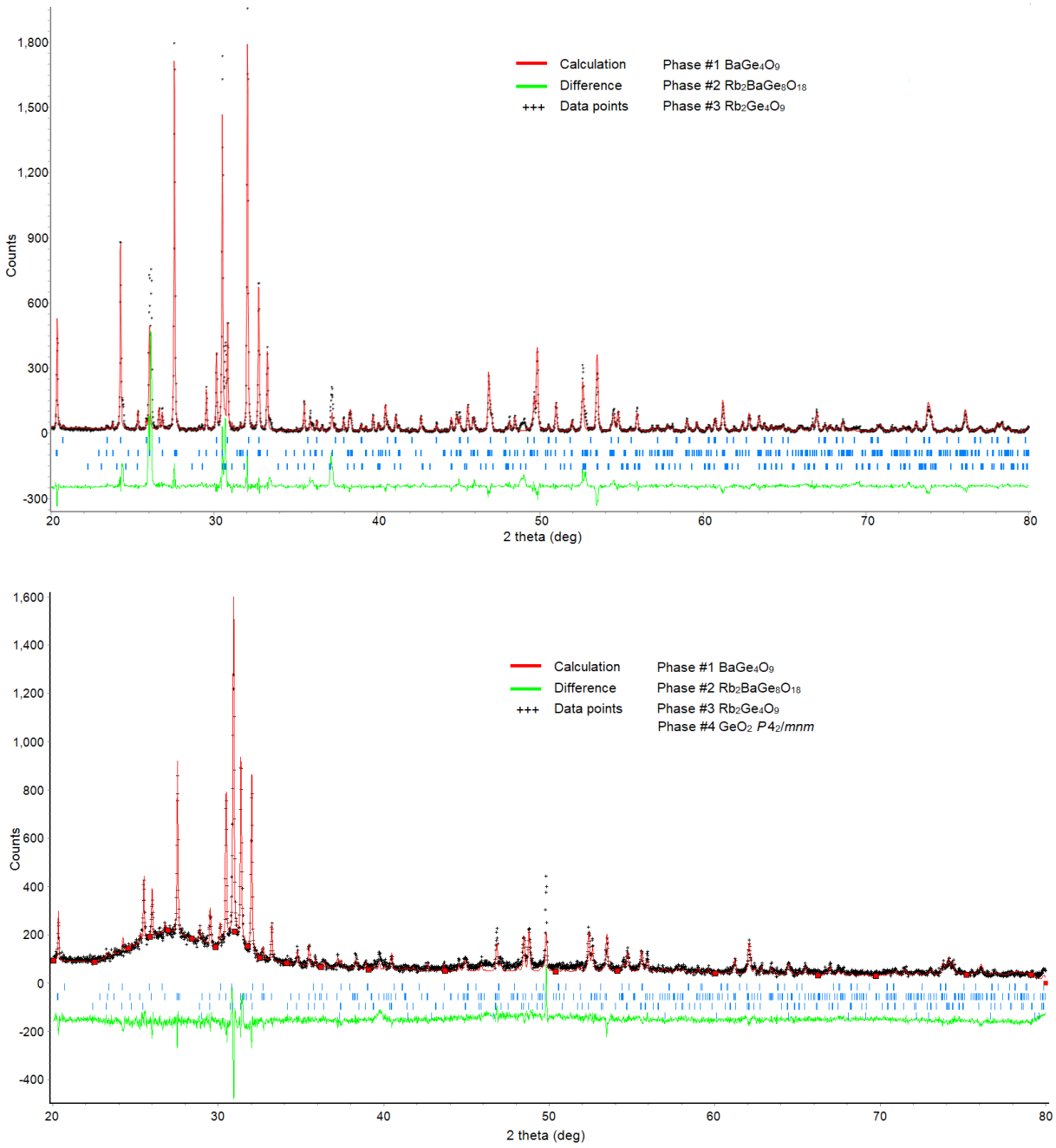

Figure 5.5. Rietveld refinement for the unsuccessful $Rb_2BaGe_8O_{18}$ synthesis directly from carbonates.

Chapter 6. Phosphorescence in Mn^{4+}-doped R^+ / R^{2+} germanates ($R^+ = Na^+$ or K^+, $R^{2+} = Sr^{2+}$)

The following chapter was published as "Phosphorescence in Mn^{4+}-doped R^+ / R^{2+} germanates ($R^+ = Na^+$ or K^+, $R^{2+} = Sr^{2+}$)" article in *Inorganic Chemistry* (*Inorg. Chem.* **2022**, *61* (24), 9364–9374). The candidate synthesized and characterized new materials by XRD, room temperature luminescence measurements, and prepared the manuscript for the publication. Dr. W. Zhang and Prof. P. S. Halasyamani provided DRS and SHG measurements. S. Hariyani and Prof. J. Brgoch measured temperature dependent luminescence. Dr. V.V. Klepov, and Prof. H.-C zur Loye performed DFT calculations.

Single crystals of three new compounds, $Na_{0.36}Sr_{0.82}Ge_4O_9$ (**1,** proposed composition), $Na_2SrGe_6O_{14}$ (**2**), and $K_2SrGe_8O_{18}$ (**3**), were obtained and characterized using single crystal X-ray diffraction. Their structures contain 3*D* anionic frameworks built from GeO_4 and GeO_6 polyhedra. Presence of the octahedral Ge^{4+} sites makes the new phases suitable for Mn^{4+} substitution to obtain red-emitting phosphors with a potential application for light conversion. Photoluminescent properties of the Mn^{4+}-substituted $Na_2SrGe_6O_{14}$ (**2**) and $K_2SrGe_8O_{18}$ (**3**) samples were studied over a range of temperatures, and red-light photoluminescence associated with the electronic transitions of tetravalent manganese was observed. The $Na_2SrGe_6O_{14}$ (**2**) phase was also substituted with Pr^{3+} on the mixed Na-Sr site similar to the previously studied $Na_2CaGe_6O_{14}$:Pr^{3+}. The red emission peak of the Pr^{3+} activator occurs at a shorter wavelength (610 nm) compared to Mn^{4+} (662-663 nm). Additionally, second harmonic generation (SHG) data were collected for the non-centrosymmetric $Na_2SrGe_6O_{14}$ (**2**) phase indicating weak SHG activity. Diffuse reflectance spectroscopy and density of states calculations were performed to estimate the band gap values for the pristine $Na_2SrGe_6O_{14}$ (**2**) and $K_2SrGe_8O_{18}$ (**3**) phases.

6.1 Introduction

New compounds featuring unique germanate frameworks in their structures exhibit important physical properties[110–113]. More specifically, germanates with simultaneous tetrahedral and octahedral coordination of Ge^{4+} are of interest both from the fundamental and practical aspects. These compounds can be used to mimic some high pressure silicates, in which silicon atoms can adopt an octahedral coordination as well[114]. From the application perspective, the octahedrally coordinated Ge^{4+} sites are attractive due to their potential phosphorescence upon the transition metal substitution[71,67,66,97,63,96,115,69], nonlinear optical[116] and piezoelectric properties[117]. In

particular, the similar size[19] and oxidation state of Mn^{4+} and Ge^{4+} enable substituting the octahedral Ge^{4+} sites with Mn^{4+}, often yielding red emitting phosphors[22,63,66,67,96,97] which can be suitable for phosphor-converted LED devices[118,92,16]. There are several advantages of Mn^{4+}, such as a strong absorption in the UV-blue region, an intense emission band in the red region of the visible spectrum, and in the case of the oxides, relatively simple preparation.[67,66,97,63,96,22] The known drawbacks of the Mn^{4+} phosphors are thermal and concentration quenching of the luminescence.[69,97] The latter, however, can be employed for the thermal sensing applications.[119–121]

Substituting in the germanate phases is not limited to Mn^{4+} since the larger cationic sites can accommodate lanthanides[122–124] or Bi^{3+}.[125] For example, langasite[126] type $Na_2CaGe_6O_{14}$ shows thermal-sensitizing phosphorescence when doped with Pr^{3+}.[122] Non-centrosymmetric $Na_2CaGe_6O_{14}$, which crystallizes with the *P*321 space group, is also interesting due to its piezoelectric properties.[117] Non-linear optical properties of the related phase, $Na_2SrGe_6O_{14}$, were also investigated[116] but no structural data have been deposited in the ICSD.[25]

Among germanate-based Mn^{4+} phosphors, tetragermanates containing alkali ($R_2Ge_4O_9$, *R* = Li-Rb) and the alkaline-earth (RGe_4O_9, *R* = Sr, Ba) metals are well-studied, both structurally[101,127,99,100,128] and optically[71,67,66,97,96,69]. The anionic frameworks of these tetragermanates are built from GeO_4 and GeO_6 polyhedra. Despite the same stoichiometry of these anionic frameworks, the structures of $R_nGe_4O_9$ (*n* = 1 or 2) compounds are different. For example, the compounds in the Na–Rb series are trigonal and centrosymmetric ($P\bar{3}c1$ space group), whereas Sr and Ba phases are non-centrosymmetric (*P*321 space group). In contrast, the Li phase exhibits a lower symmetry crystallizing with the acentric orthorhombic space group $P2_1ca$[128]. Such variations are associated with the different radii and charges of the R^+ and R^{2+} cations.

Interestingly, $Na_2Ge_4O_9$ forms a metastable phase, while the lack of the reliable structural data on *R* = Mg and Ca tetragermantates may indicate their lower thermodynamic stability as compared to the other phases[99].

In this report we describe the synthesis, structure, and optical properties of three new compounds based on germanate frameworks: a tetragermanate $Na_{0.36}Sr_{0.82}Ge_4O_9$ (**1**), a langasite-type $Na_2SrGe_6O_{14}$ (**2**), and an octagermanate $K_2SrGe_8O_{18}$ (**3**), isostructural to $K_2BaGe_8O_{18}$ [98]. The new phases were successfully doped with Mn^{4+} (phases **2** and **3**) and Pr^{3+} (phase **2**) to explore their photoluminescence properties. As $Na_2SrGe_6O_{14}$ (**2**) crystallizes in a non-centrosymmetric space group, its second harmonic generation (SHG) response was measured.

6.2 Experimental

Powders of GeO_2 (99.999 wt. %), $KHCO_3$ (99 wt. %), NaCl (99 wt. %), Na_2CO_3 (99.5 wt. %), $SrCl_2$ (99 wt. %), $SrCO_3$ (99 wt. %) $MnCO_3$ (99.9 wt.%), $Mn(CH_3COO)_2{\cdot}4H_2O$ (99.999 wt.%), and Pr_6O_{11} (99.9 wt.%) were used as received.

6.2.1 Synthesis of the new phases as single crystals

The reagents in the calculated ratios were thoroughly ground in an agate mortar and pressed into pellets. The pellets were placed into a platinum crucible and thermally treated as described below. Note that the use of alumina or silica reaction vessels results in Al or Si admixtures on the Ge sites, thus the use of platinum crucibles in these reactions was essential to obtain pure Ge phases.

$Na_{0.36}Sr_{0.82}Ge_4O_9$ (**1**) crystals were obtained while targeting $Na_{2x}Sr_{1-x}Ge_4O_9$ phases. When carbonate precursors were used during synthesis instead of chloride precursors, $Na_2SrGe_6O_{14}$ (**2**) crystals were obtained. Attempts to obtain the hypothetical $K_2SrGe_6O_{14}$ phase yielded the

octagermanate phase, $K_2SrGe_8O_{18}$ (**3**). The synthetic conditions and molar ratios shown below yielded single crystals of the new phases suitable for the single crystal X-ray diffraction (yet not the target phases).

$Na_{0.36}Sr_{0.82}Ge_4O_9$ (**1**) crystals were obtained in a reaction between NaCl (0.0094 g), $SrCl_2$ (0.0383 g), and GeO_2 (0.1348 g) in a 0.50:0.75:4.0 molar ratio. A pellet of the starting materials was heated to 1050 °C at a rate of 200 °C/h and dwelled at this temperature for 18 h, after which the furnace was cooled to 700°C at a rate of 6°C/h and switched off.

Single crystals of $Na_2SrGe_6O_{14}$ (**2**) were obtained by reacting Na_2CO_3 (0.0492 g) with $SrCO_3$ (0.0086 g) and GeO_2 (0.1214 g) in a 1.6:0.20:4.0 molar ratio. The sample pellet was heated to 1050 °C at a rate of 200 °C/h and dwelled for 2 h at this temperature. The reaction was cooled to 900 °C at a rate of 100 °C/h and then to 800 °C at 10 °C/h rate. Further cooling to room temperature was done by switching the furnace off.

Single crystals of $K_2SrGe_8O_{18}$ (**3**) were obtained in a reaction between $KHCO_3$ (0.0392 g), $SrCO_3$ (0.0289 g), and GeO_2 (0.1228 g) in a 2:1:6 molar ratio. The sample pellet was heated to 1050°C at a rate of 200 °C/h. After 2 h the furnace was cooled down to 950°C at a rate of 50 °C/h, and then to 850 °C at 10 °C/h rate. Further cooling to room temperature was done by switching the furnace off.

6.2.2 Single crystal X-ray diffraction

The single crystals of **1-3** that were suitable for X-ray diffraction (XRD) were picked manually. The experimental data for **1-3** were collected at room temperature on a STOE IPDS II diffractometer (MoKα radiation) equipped with an image-plate type detector. The numerical absorption correction was performed by optimizing the crystal shape against equivalent reflections

with the X-Shape software[39]. Initial structure solution was done with the SHELXT[28] software and refined using the SHELXL software by full-matrix least square refinements[43]. The solution and refinement programs were run via the OLEX2 interface[42]. The crystallographic data and refinement results are summarized in Table 1. Compositions of the single crystals were determined based on the single crystal diffraction. In $Na_{0.36}Sr_{0.82}Ge_4O_9$ (**1**), the composition of the mixed Na/Sr site was determined based on the two constrains: (1) the density of the Na/Sr site equals the refined electron density; (2) the charge of the Na/Sr site balances the charge of the $Ge_4O_9^{2-}$ framework (more details are in the footnote of Table 6.1)

Table 6.1. Selected crystallographic data and refinement results for **1-3**

Compound	**1**	**2**	**3**
Formula	$Na_{0.36}Sr_{0.82}Ge_4O_9$*	$Na_2SrGe_6O_{14}$	$K_2SrGe_8O_{18}$
Formula weight	514.47	793.12	1034.54
Crystal system	*trigonal*		
Space group	*R*32	*P*321	$P\bar{3}c1$
a, Å	11.3584(13)	8.2322(12)	11.5937(16)
c, Å	4.6701(15)	4.8677(10)	19.225(4)
Flack parameter	0.01(2)	-0.054(19)	-
Volume, Å^3	521.8(2)	285.68(8)	2237.9(6)
Z	3	1	6
ρ_{calcg}, cm^3	4.946	4.610	4.606
μ/mm^{-1}	24.730	20.361	20.088
F(000)	705	364	2856
2θ range, °	7.18-69.64	5.72-69.66	5.87-69.88
Index ranges	$-14 \le h \le 15$, $-18 \le k \le 18$, $-7 \le l \le 3$	$-13 \le h \le 13$, $-13 \le k \le 13$, $-7 \le l \le 7$	$-18 \le h \le 18$, $-18 \le k \le 13$, $-30 \le l \le 30$
Reflections collected	1922	5196	25219
Data/restraints/ parameters	507/0/30	846/0/38	3273/0/134
GOOF	1.073	1.203	1.044
R_1 (I>2σ (I))	0.0160	0.0194	0.0653

Largest diff. peak/hole, e/Å^3	0.54/-0.96	0.88/-0.68	3.01/-2.40

*Electron density from the experiment was ≈ 5.86 e^- (or 0.154 of the Sr atom). If x is the Na occupancy and y is the Sr occupancy, then $11x + 38y = 5.86$. The total charge from Na and Sr is +2 to balance $Ge_4O_9^{2-}$. Considering the symmetry of the structure, the total charge on the mixed Na^+ / Sr^{2+} site should be +⅓. Thus $x + 2y = ⅓$. From those two equations, x and y were found to be ≈ 0.060 and ≈ 0.137, respectively, giving the $Na_{0.36}Sr_{0.82}Ge_4O_9$ formula.

6.2.3 Synthesis of the new germanate phosphors by solid-state reaction

The $Na_2SrGe_{6-x}O_{14}$:$x$$Mn^{4+}$ (**2**) samples were prepared through a solid-state reaction between Na_2CO_3, $SrCO_3$, GeO_2, and $MnCO_3$ in the 2:1:(6-x):x ratios, where x = 0.002, 0.008, and 0.016. The reagents were ground, pressed into a pellet, and annealed at 950 °C for 12 hours. The $Na_2Sr_{1-x}Ge_6O_{14}$: $x$$Pr^{3+}$ sample was prepared in a similar way with a molar ratio of 2:0.994:6:0.001 for Na_2CO_3, $SrCO_3$, GeO_2 and Pr_6O_{11}, respectively. Note that a 4:1 Na : Sr molar ratio was initially proposed for the solid state synthesis of $Na_2SrGe_6O_{14}$ (*i.e.*, two times Na excess based on the stoichiometry) because the exact 2:1 ratio resulted in the formation of the significant amount of the $SrGe_4O_9$ phase. We found, however, that the purest $Na_2SrGe_6O_{14}$ product can be obtained with a slight excess of sodium (Na_2CO_3 : $SrCO_3$ = 1.2:1).

Samples of $K_2SrGe_{8-x}O_{18}$: $x$$Mn^{4+}$ were synthesized by solid-state reactions between $SrCO_3$, $KHCO_3$, GeO_2, $MnCO_3$ or $Mn(CH_3COO)_2{\cdot}4H_2O$ in a 2: 1: (8-x): x ratios, where x = 0.003, 0.005, 0.016, and 0.032. The mixtures were ground, pressed into a pellet, and annealed at 950 °C for 8 hours. A second annealing for another 8 hours at 950 °C was done for each sample after regrinding and pressing it into a pellet. To avoid the formation of side products, such as $SrGe_4O_9$, a very thorough grinding is required before each annealing. Alternatively, the $K_2SrGe_8O_{18}$ phase can be prepared by the solid-state reaction between $K_2Ge_4O_9$ and $SrGe_4O_9$ in a 1:1 molar ratio. This route is much slower and takes 3 to 4 annealing steps for 24 hours each.

The powder X-ray diffraction data of $Na_2SrGe_6O_{14}$ (**2**) and $K_2SrGe_8O_{18}$ (**3**) prepared via the solid-state route were collected on a PANalytical X'Pert PRO diffractometer equipped with a germanium monochromator (Cu $K\alpha_1$ radiation) in the 20-80° 2θ range. The Rietveld refinement[44] results are provided in the Supplementary Information (Figure 6.11, 6.12).

6.2.4 Photoluminescence measurements

Absorption and emission spectra of the prepared $Na_2SrGe_6O_{14}$ (**2**)- and $K_2SrGe_8O_{18}$ (**3**)-based phosphors were collected on an Agilent Cary Eclipse fluorescence spectrophotometer at room temperature.

For the temperature-dependent photoluminescence measurements, polycrystalline samples of $Na_2SrGe_6O_{14}$: Mn^{4+} and $K_2SrGe_8O_{18}$: Mn^{4+} were combined with an optically transparent resin (United Adhesives) and deposited onto a quartz slide (Chemglass). Temperature-dependent emission spectra from 80 K to 500 K were obtained using a Janis cryostat (VPF-100) and a PTI fluorescence spectrophotometer with a 75 W xenon arc lamp for excitation.

6.2.5 Second harmonic generation (SHG) measurements

SHG measurements were performed on powders using a pulsed Nd:YAG laser (Quantel Ultra 50) with a wavelength of 1064 nm. Ground crystalline α-SiO_2 was used a reference SHG material. For $Na_2SrGe_6O_{14}$, the SHG intensity is roughly 0.9 of α-SiO_2. The sample was slightly impure. The impurity phase was $SrGe_4O_9$ (< 1 wt. %), which is also non-centrosymmetric. A pure sample of $SrGe_4O_9$ was obtained and its activity was measured for a comparison. The SHG activity of the $SrGe_4O_9$ phase was found to be much lower than $Na_2SrGe_6O_{14}$ (0.4 of α-SiO_2), and thus, should not significantly impact the $Na_2SrGe_6O_{14}$ SHG measurement.

6.2.6 Band gap calculations and experimental measurement

UV-visible reflectance data were collected on a Varian Cary 5000 scan UV-vis-NIR spectrophotometer over the 200–2000 nm spectral range at room temperature. Polytetrafluoroethylene was used as a reference material. The reflectance spectrum was converted to absorbance using the Kubelka-Munk function[129,130].

First-principles calculations were performed using density functional theory (DFT) with the Vienna Ab-initio Package (VASP) planewave code[131,132], generalized gradient approximation of Perdew, Burke, and Ernzerhof (PBE)[133], and projector augmented wave (PAW) method [134,135].The Na, K, Sr, Ge, and O valence electron configurations considered for construction of PAW potentials were $2p^6 3s^1$, $3s^2 3p^6 4s^1$, $4s^2 4p^6 5s^2$, $4s^2 3d^{10} 4p^2$, and $2s^2 2p^4$, respectively. To eliminate partial occupancy on the Sr/Na site in $Na_2SrGe_6O_{14}$, the symmetry of the structure was lowered to triclinic and 2 out of 3 equivalent sites were assigned to Na. Spin-polarized calculations were performed, with 520 eV cut-off energy for the plane wave basis set, 10^{-6} eV energy convergence criteria and 5×5×7 and 3×3×2 *k*-point meshes for $Na_2SrGe_6O_{14}$ and $K_2SrGe_8O_{18}$. The ground state geometries at 0 K were optimized by relaxing the cell volume, atomic positions, and cell symmetry until the maximum force on each atom is less than 0.001 eV/Å.

6.3. Results and Discussion

6.3.1. Crystal structure

Phase (1): $Na_{0.36}Sr_{0.82}Ge_4O_9$ or γ-$SrGe_4O_9$? The structure solution and refinement of $Na_{0.36}Sr_{0.82}Ge_4O_9$ was performed with the *R*32 space group. As we mentioned above, the electron density on the 9*e* Wyckoff position where the cations reside would be insufficient for a fully occupied Sr position. Additionally, the fully occupied Sr position would make the structure not

charge balanced. Thus, the mixed Na-Sr site was accepted as a possible reason for the presence of the electron density deficient position.

There are two crystallographic Ge sites in the structure of this rhombohedral tetragermanate, octahedral Ge1 (3*b* Wyckoff position) and tetrahedrally coordinated Ge2 (9*d*). The Ge-O bond lengths are 1.891(3) Å for the six symmetrically equivalent Ge1-O bonds and 1.738(3)–1.758(2) Å for the Ge2-O bonds, and are in a good agreement with the previously reported values [20]. The corner sharing GeO_4 tetrahedra form infinite helical chains running along the *c* direction (Figure 6.1). These chains are linked into an infinite framework by the GeO_6 octahedra. Na and Sr cations share the same 9*e* site and occupy the channels within the anionic germanate framework.

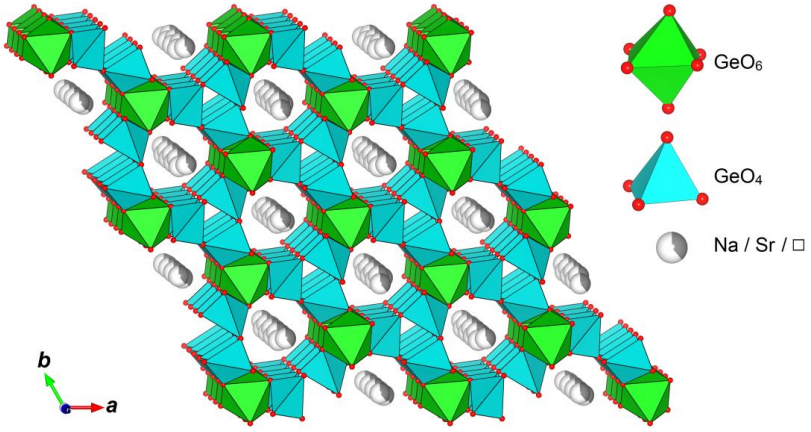

Figure 6.1. A view of the $Na_{0.36}Sr_{0.82}Ge_4O_9$ (**1**) structure fragment along the *c* direction. Hereinafter, GeO_6 octahedra are green, GeO_4 tetrahedra are cyan, oxygen atoms are red. Na^+ and Sr^{2+} cations are gray (with □ representing the deficiency).

In comparison to the previously reported tetragermanates, $SrGe_4O_9$ [127] and $Na_2Ge_4O_9$ [99], the $Na_{0.36}Sr_{0.82}Ge_4O_9$ (**1**) structure containing mixed Na-Sr positions demonstrates new features. First, $Na_{0.36}Sr_{0.82}Ge_4O_9$ crystallizes with a rhombohedral unit cell, while the pure Na and pure Sr phases

crystallize with primitive trigonal ones. Another feature of $Na_{0.36}Sr_{0.82}Ge_4O_9$ (**1**) is the cationic deficiency on the Na/Sr site, which is only 39% occupied by the cations. Thus, the chemical formula for **1** can be also written as $Na_{0.36}Sr_{0.82}\square_{1.82}Ge_4O_9$, with □ representing the deficiency.

When compared to $SrGe_4O_9$[127], $Na_{0.36}Sr_{0.82}Ge_4O_9$ (**1**) has nearly the same unit cell dimensions but there is a significant topological difference between the two structures. As illustrated in Figure 6.2, the GeO_4 tetrahedra in $SrGe_4O_9$ form isolated rings that are stacked along the *c* direction and connected to each other through GeO_6 octahedra. In $Na_{0.36}Sr_{0.82}Ge_4O_9$ (**1**), the rings open, and two terminal GeO_4 units shift along the stacking direction, connecting to the adjacent units to form infinite helical chains (Figure 6.2). These chains and rings are further connected by GeO_6 octahedra. The topological analysis of the GeO_n polyhedra connectivity in **1** performed with the ToposPro[82] software did not reveal any matches within the topological database. On the contrary, the germanate framework in $SrGe_4O_9$[127] resembles the titanate-silicate one in the naturally occurring $BaTiSi_3O_9$ compound[136] (a rare mineral benitoite). Thus, the cationic vacancies and the rare connectivity type of the germanate framework in the $Na_{0.36}Sr_{0.82}Ge_4O_9$ (**1**) phase establishes that the phase formation cannot be described as a simple Na / Sr admixture in the $SrGe_4O_9$ structure[127].

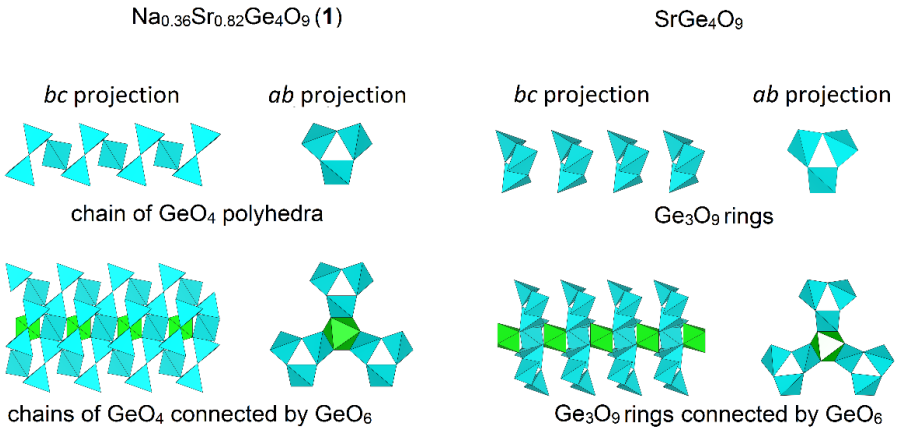

Figure 6.2. The comparison between GeO_n (n = 4 and 6) polyhedra connectivity in $Na_{0.36}Sr_{0.82}Ge_4O_9$ (**1**) and $SrGe_4O_9$ [127]. Oxygen atoms are omitted.

An alternative structure solution for phase **1** should be mentioned. The literature reports the γ-$PbGe_4O_9$ phase, a lead tetragermanate polymorph with the *C*2 symmetry possessing a trigonal pseudosymmetry[137]. The structural similarities between phase **1** and γ-$PbGe_4O_9$ include the formation of the infinite helical chains from GeO_4 units. Because of these similarities, phase **1** can be thought as γ-$SrGe_4O_9$, since the structure solution and refinement can be done in the *C*2 space group as well, with a = 7.2490(14) Å, b = 11.333(2) Å, c = 4.6562(9) Å, and β = 115.45(3)°. However, the available experimental data casts doubt on the existence of the monoclinic γ-$SrGe_4O_9$. First, polymorphism of $SrGe_4O_9$ has never been reported as there is only one entry in ICSD for $SrGe_4O_9$ and it is for the trigonal *P*321 phase. Moreover, differential thermal analysis for $SrGe_4O_9$ shows no phase transition until the melting point (Figure 6.13). Second, there was no experimental evidence of twinning from our single crystal XRD experiment (the data processed with Apex4[138]). Third, phase **1** was obtained in the presence of NaCl, which gives the possibility of mixed Sr/Na sites. If the synthesis is repeated under the same conditions, but in the absence of NaCl, the well-known trigonal $SrGe_4O_9$ phase forms. Finally, the Le Bail simulated diffraction pattern of the *R*32 cell demonstrates the same features as the experimental diffractogram (Figure 6.14, 6.15). These features are not described in the *C*2 Le Bail simulation. Taking these points into account, we consider phase **1** as $Na_{0.36}Sr_{0.82}Ge_4O_9$.

$Na_2SrGe_6O_{14}$ (2). The Ge atoms in $Na_2SrGe_6O_{14}$ occupy three sites: 3*f* (Ge1), 1*a* (Ge2), and 2*d* (Ge3). Ge2 is octahedrally coordinated by oxygen, while Ge1 and Ge3 adopt a tetrahedral environment. GeO_4 tetrahedra corner-share to form infinite layers that are parallel to the *ab* plane (Figure 6.3 top). The neighboring layers are connected into a 3D anionic framework by the GeO_6 polyhedra (Figure 6.3 center). The channels of this framework are occupied by Na and Sr cations

(Figure 6.3 bottom). The Na and Sr cations share the 3*e* site in a 2:1 ratio, giving the $Na_2SrGe_6O_{14}$ composition.

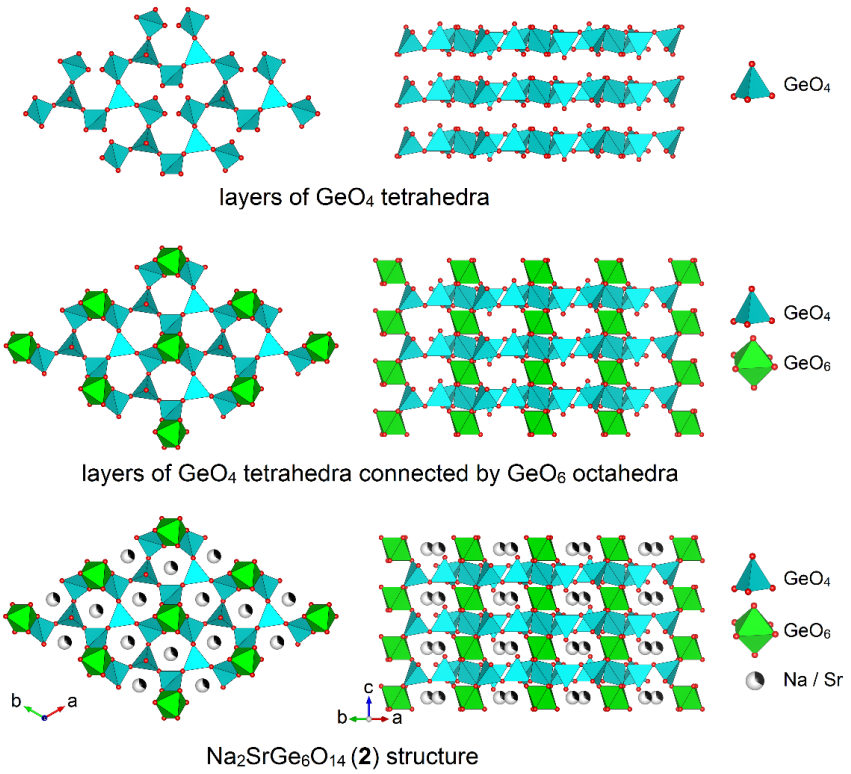

Figure 6.3. GeO_n polyhedra connectivity in $Na_2SrGe_6O_{14}$ (**2**) and a fragment of the $Na_2SrGe_6O_{14}$ (**2**) structure in two projections.

The $Na_2SrGe_6O_{14}$ (**2**) structure demonstrates the same features as $Na_2CaGe_6O_{14}$ one [117]. Ge2 is surrounded by six oxygen atoms forming a regular octahedron. $Ge1O_4$ is slightly distorted (with two shorter and two longer Ge–O bonds), while the distortion of the Ge3 tetrahedral surrounding is more pronounced. One of the Ge–O bonds (1.68 Å) is much shorter than the three other (1.76 Å). Overall, the $Na_2SrGe_6O_{14}$ (**2**) phase adopts a langasite-type[139] crystal structure.

$K_2SrGe_8O_{18}$ (3). Similar to **1** and **2**, the $K_2SrGe_8O_{18}$ (**3**) structure contains germanium atoms in both octahedral and tetrahedral oxygen environments. Three tetrahedrally coordinated Ge atoms occupy general positions, while four octahedrally coordinated ones are located on special positions. In contrast to **1** and **2**, K and Sr atoms occupy two distinct crystallographic sites in **3**, 12*g* (K) and 6*f* (Sr). As in **1** and **2**, GeO_4 and GeO_6 polyhedra are connected to form an anionic framework. The arrangement of the Ge polyhedra in **3** is similar to that in $K_2Ge_4O_9$ [100] and $SrGe_4O_9$ [127] with 0D Ge_3O_9 rings connected by GeO_6 octahedra through corner sharing.

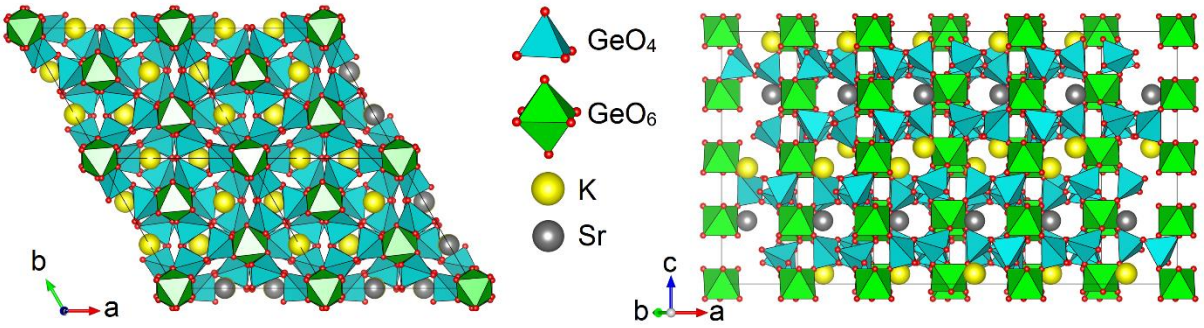

Figure 6.4. The fragment of the $K_2SrGe_8O_{18}$ (**3**) structure in two projections. K atoms are yellow, Sr – gray.

$K_2SrGe_8O_{18}$ (**3**) and $K_2Ge_4O_9$[100] crystallize with the $P\bar{3}c1$ space group, while $SrGe_4O_9$ adopts the non-centrosymmetric $P321$ group[127]. Despite the similar stoichiometries and germanium polyhedra arrangements, there is a subtle difference between these three structures resulting from differences of the GeO_n polyhedra connectivity. This connectivity difference for some germanates structures has been analyzed in a previous work on $Na_2BaGe_8O_{18}$ and $Rb_2BaGe_8O_{18}$ phases[140].

6.3.2 Calculated and experimental band gap

The electronic structures of $Na_2SrGe_6O_{14}$ and $K_2SrGe_8O_{18}$ were calculated using *ab initio* methods (Figure 6.5). In both compounds, the top of the valence band consists mostly of O states, whereas the bottom of the conduction band consists of both Ge states with a significant contribution from the O orbitals. The theoretical bandgaps, 2.61 and 2.78 eV for $Na_2SrGe_6O_{14}$ and $K_2SrGe_8O_{18}$, respectively, indicate insulating behavior in both oxides.

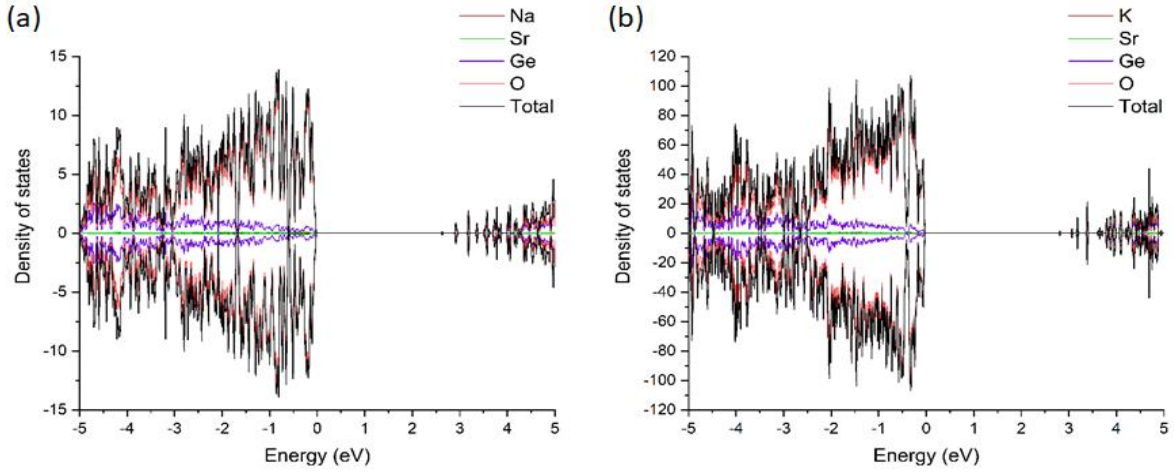

Figure 6.5. Density of states of $Na_2SrGe_6O_{14}$(a) and $K_2SrGe_8O_{18}$ (b).

The calculated values of the band gaps for **2** and **3** are significantly lower than the experimental data (Figure 6.6): 2.61 eV and 2.78 eV vs. 4.82 eV and 5.23 eV for $Na_2SrGe_6O_{14}$ and $K_2SrGe_8O_{18}$, respectively. The mismatch is the result of the known drawbacks of DFT calculations of insulators using the PBE functional. The magnitude of the mismatch for our calculations is comparable to that of another germanate phosphor material – $Li_3RbGe_8O_{18}$, where the calculated band gap was 2.72 eV, while the experimental one was measured to be 5.26 eV[63].

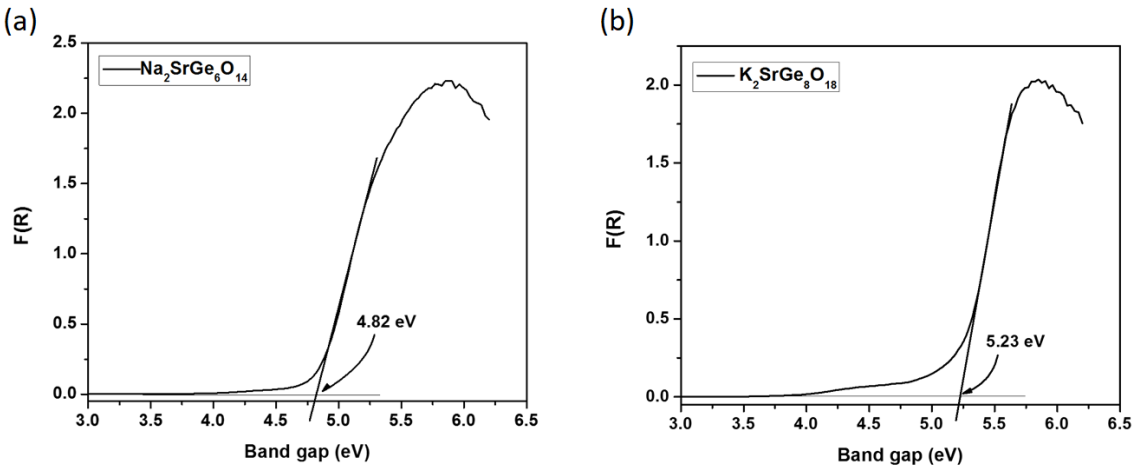

Figure 6.6. The F(R) versus energy (in eV) plot for the pristine $Na_2SrGe_6O_{14}$ (a) and $K_2SrGe_8O_{18}$ (b) phases. The corresponding optical band gap values are given on the plot.

6.3.3 Photoluminescent properties of the Pr^{3+} and Mn^{4+} activated germanates

A phosphor was prepared from the $Na_2SrGe_6O_{14}$ phase via Pr^{3+} doping and the photoluminescent emission (PL) and excitation (PLE) spectra were collected (Figure 6.7). The Pr^{3+} content was 0.6 mol. %, which is identical to that of the previously studied $Na_2CaGe_6O_{14}$ [122]. Under the UV excitation ($\lambda_{ex.}$ = 246 nm), the $Na_2Sr_{0.994}Ge_6O_{14}$:0.006 Pr^{3+} sample demonstrates the same emission features as Pr^{3+}-substituted $Na_2CaGe_6O_{14}$ [122]: one emission peak at 493 ($^3P_0 \rightarrow {}^3H_4$ transition) and a second, dominating emission peak at 610 nm ($^1D_2 \rightarrow {}^3H_4$ transition) in the visible region (Figure 6.7). The peaks are slightly shifted (1-2 nm) compared to $Na_2CaGe_6O_{14}$, where the corresponding peaks occur at 492 and 612 nm[122].

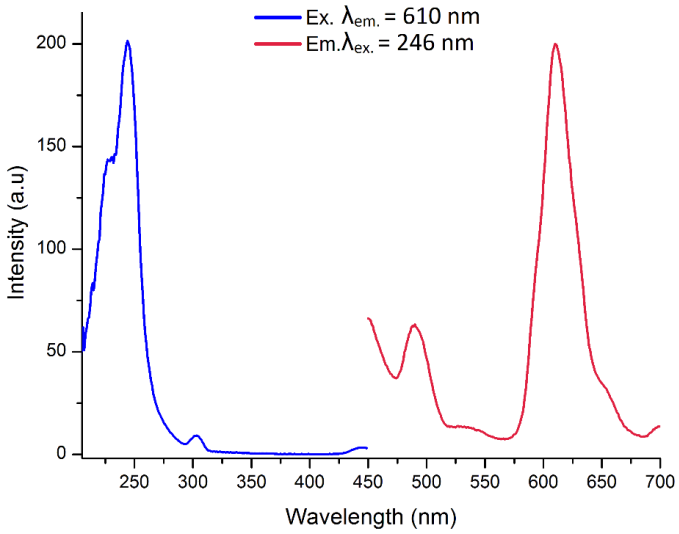

Figure 6.7. PLE and PL spectra of the $Na_2Sr_{0.994}Ge_6O_{14}$: 0.006 Pr^{3+} sample at room temperature.

The octahedral Ge site in the $Na_2SrGe_6O_{14}$ (**2**) structure was doped with Mn^{4+} and the PL and PLE spectra were collected (Figure 6.8a) for the corresponding samples. This material has two distinct absorption maxima. The first and dominant absorption peak is located in the UV region at 290 nm, and the second is in the visible region ≈ 440 nm. The latter is associated with $^4T_{2g} \leftarrow {}^4A_{2g}$ transition of the Mn^{4+} ion. The UV absorption band is asymmetric and likely formed by the overlap of the O^{2-} to Mn^{4+} charge-transfer band and the allowed $^4T_{1g} \leftarrow {}^4A_{2g}$ electron transitions of Mn^{4+} [1].

The emission peak at 663 nm is associated with $^2E_g \rightarrow {}^4A_{2g}$ relaxation of Mn^{4+} and the peak position is in good agreement with previous reports of Mn^{4+} phosphors[59,62,141–143]. The position of the emission peak is known to be independent on the crystal field strength but affected by the covalency of the Mn–ligand bonds[91].

The performance of the $Na_2SrGe_{6-x}O_{14}:Mn^{4+}$ (x = 0.002, 0.008, 0.016) phosphor was optimized by adjusting the activator substitution level. We found that $Na_2SrGe_{5.992}O_{14}$:0.008 Mn^{4+} sample exhibits much higher emission intensity compared with the initially prepared

$Na_2SrGe_{5.998}O_{14}$:0.002 Mn^{4+} sample (Figure 6.8b), whereas a higher substitution level of Mn^{4+} leads to luminescence quenching and a decrease in the emission intensity.

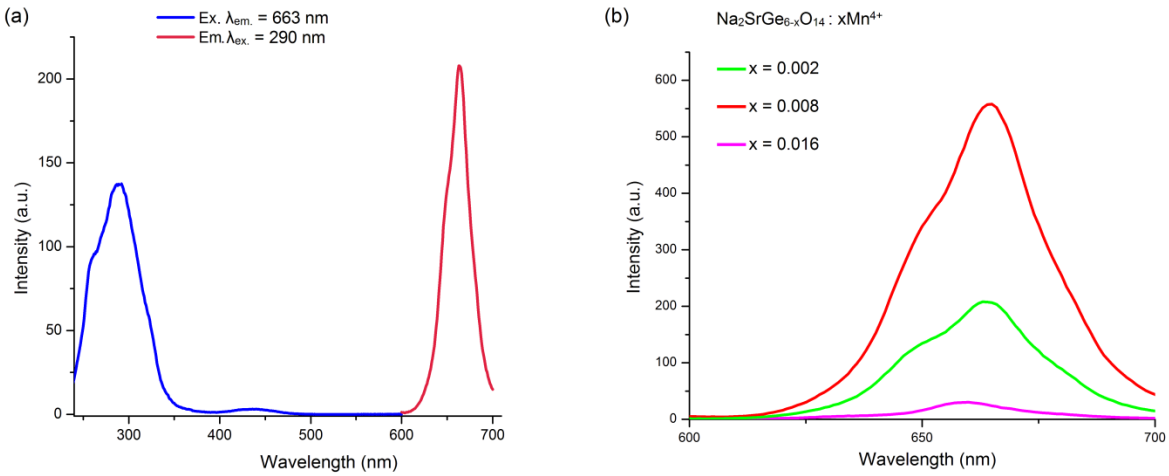

Figure 6.8. PLE and PL spectra of the $Na_2SrGe_{5.998}O_{14}$: 0.002 Mn^{4+} sample (a) and the PLE spectra of the $Na_2SrGe_{6-x}O_{14}$: xMn^{4+} series (x = 0.002, 0.008, and 0.016) (b).

The PLE and PL data for the Mn^{4+} doped $K_2SrGe_8O_{18}$ (**3**) samples were collected at room temperature (Figure 6.9a). The emission peak positions are close to those observed from $Na_2SrGe_6O_{14}$:Mn^{4+}. Under UV excitation, the sample emits red light with a narrow peak at 662 nm. This data is in a good agreement with other reported Mn^{4+}-substituted germanate phases[71,96,144]. $K_2SrGe_{7.995}O_{18}$:0.005 Mn^{4+} exhibits the highest emission intensity (Figure 6.9b) in the series.

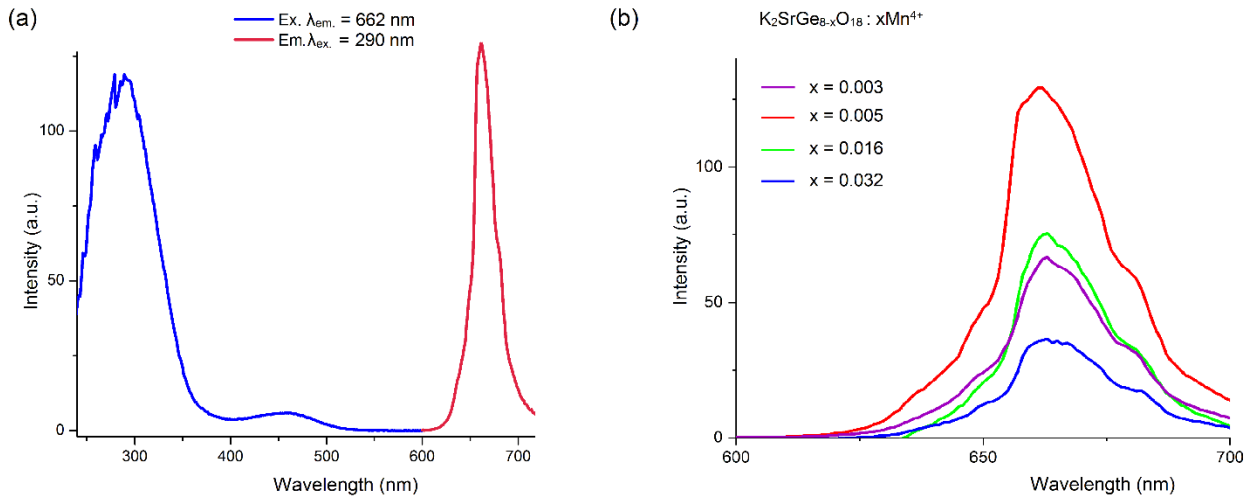

Figure 6.9. PLE and PL spectra of the $K_2SrGe_{7.995}O_{18}$: 0.005 Mn^{4+} sample (a) and the emission spectra of $K_2SrGe_{8-x}O_{18}$: xMn^{4+} (x = 0.003, 0.005, 0.016, and 0.032) (b).

For both $Na_2SrGe_6O_{14}$ (**2**) and $K_2SrGe_8O_{18}$ (**3**) the approximate positions of the $^4T_{1g} \leftarrow {}^4A_{2g}$ (^4F) peaks overlap with the charge-transfer peaks, which can be estimated from the following equations[2]:

$$D_q = E(\,^4T_{2g} \leftarrow {}^4A_{2g})\,/10 \quad (1)$$

$$\frac{D_q}{B} = \frac{15(x-8)}{x^2 - 10x} \quad (2)$$

$$x = \frac{E(^4T_{1g} \leftarrow {}^4A_{2g}) - E(^4T_{2g} \leftarrow {}^4A_{2g})}{D_q} \quad (3)$$

$$\frac{E(^2E_g \rightarrow {}^4A_{2g})}{B} = \frac{3.05C}{B} + 7.9 - \frac{1.8B}{D_q} \quad (4)$$

where D_q is a crystal field strength for Mn^{4+}, B and C are Racah parameters.

If a free Mn^{4+} cation is introduced into a crystal field, the Racah parameters are reduced due to the nephelauxetic effect[3]. The magnitude of this effect depends on the covalency of the Mn-ligand bonds and influences the optical properties of the Mn^{4+}-substituted phosphors. The nephelauxetic ratio β_1, suggested by Brik et al.,[91] has a linear correlation to the energy of the ^2E_g level (i.e. the emission frequency, cm^{-1}):

$$E(^2E_g \rightarrow {}^4A_{2g}) = -880.49 + 16261.92\ \beta_1 \quad (5)$$

$$\text{where } \beta_1 = \sqrt{\left(\frac{B}{B_0}\right)^2 + \left(\frac{C}{C_0}\right)^2} \quad (6)$$

(B_0 = 1160 cm^{-1} and C_0 = 4303 cm^{-1} are free Mn^{4+} Racah parameters[145]). The results of the calculations for $Na_2SrGe_6O_{14}$ (**2**) and $K_2SrGe_8O_{18}$ (**3**) are summarized in Table 2. The calculated positions of the $^4T_{1g} \leftarrow {}^4A_{2g}$ absorption peaks are 328 and 337 nm for $Na_2SrGe_6O_{14}$ (**2**) and $K_2SrGe_8O_{18}$ (**3**), respectively.

Table 6.2. PLE and PL parameters of the Mn^{4+} doped $Na_2SrGe_6O_{14}$ (**2**) and $K_2SrGe_8O_{18}$ (**3**) samples*

Sample	Dq, cm^{-1}	B, cm^{-1}	C, cm^{-1}	β_1	$E(^2E_g)$, cm^{-1}	$E(^4T_{1g})$, cm^{-1}
$Na_2SrGe_6O_{14}$ (**2**)	2252	774	3099	0.982	15083	30520
$K_2SrGe_8O_{18}$ (**3**)	2174	771	3117	0.983	15106	29664

*The values of B, C, and $E(^4T_{1g})$ calculated from equations 1-6 and may vary from the experimental data.

The calculated values of the crystal field parameters Dq, B and C, and nephelauxetic ratio β_1 for **2** and **3** are close to those reported for the $K_2Ge_4O_9$ phase at room temperature [70]. The Mn^{4+} cation in the oxide matrix with the more covalent bonds typically has $\beta_1 < 1$, while in the fluoride matrix with more ionic bonds this value exceeds 1[91]. Thus, the β_1 values for $Na_2SrGe_6O_{14}$ (**2**) and $K_2SrGe_8O_{18}$ (**3**) are in the typical covalent oxide region.

6.3.4 Temperature-dependent phosphorescence in $Na_2SrGe_6O_{14}$ (2) and $K_2SrGe_8O_{18}$ (3)

Photoluminescence thermal quenching is one of the limitations of transition metal-based luminescent materials. To study the change in emission intensity as a function of temperature, temperature-dependent luminescence spectra were collected for the $Na_2SrGe_{5.992}O_{14}$:$0.008Mn^{4+}$ and $K_2SrGe_{7.995}O_{18}$:$0.005Mn^{4+}$ samples (Figure 6.16 and 6.17in the Supplementary). The emission from the $Na_2SrGe_{5.992}O_{14}$:$0.008Mn^{4+}$ sample was weak and demonstrated significant artifacts; for that reason, only the data for $K_2SrGe_{7.995}O_{18}$:$0.005Mn^{4+}$ is shown below.

Figure 6.10 includes a contour plot of the temperature dependent PL spectra for the $K_2SrGe_{7.995}O_{18}$: $0.005Mn^{4+}$ sample (Figure 6.10a) and the normalized integrated intensity data for the 77 – 500 K temperature range (Figure 6.10b). As expected, the increasing temperature results in the decrease in the photoluminescence intensity, which gradually drops to 50 % of the low temperature emission intensity at 420 K (Figure 6.10b). The decrease in the photoluminescence intensity at the elevated temperatures originates from the higher probability of the non-radiative relaxation[1]. It can be illustrated with configurational coordinate diagram: at elevated temperatures the relaxation from ^2E_g state may occurs to $^4T_{2g}$ state and then to the ground $^4A_{2g}$ state via the crossover points without emission of light. The sample demonstrates decent luminescence thermal stability at the operational temperature of LED bulbs. A moderate redshift and broadening of the emission peak with the increasing temperature was also observed (Figure 6.18 in the Supplementary).

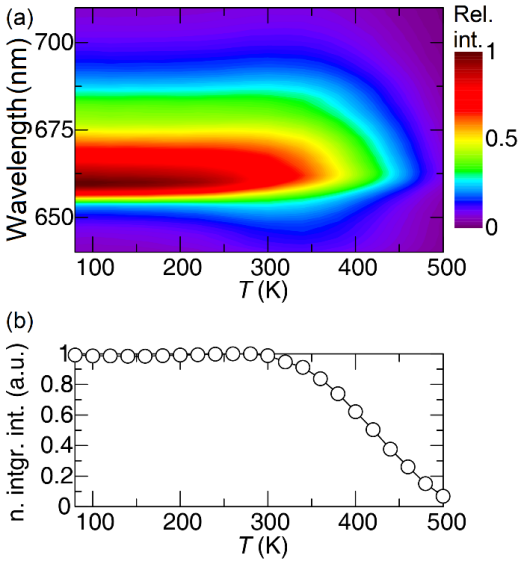

Figure 6.10. Contour plot of the temperature dependent PL spectra for $K_2SrGe_{7.995}O_{18}$: $0.005Mn^{4+}$ (a) and the normalized integrated intensity of its emission as a function of temperature (b).

The thermal quenching activation energy (ΔE) can be calculated from the following equation [146]:

$$I_T = \frac{I_0}{1 + A \exp\left(\frac{-\Delta E}{kT}\right)}$$

where I_T is the emission intensity at given temperature, I_0 - emission intensity at room temperature, k – Boltzmann constant, A – constant for a host material, ΔE – activation energy. By plotting $\ln(I_0/I_T\text{-}1)$ versus 1/kT from the experimental data and the following linear fitting (Figure 6.19), the activation energy ΔE was found to be 0.33 eV for the $K_2SrGe_{7.995}O_{18}$:$0.005Mn^{4+}$ sample.

6.4 Conclusion

Single crystal X-ray diffraction was used to study the structures of three new Na-Sr and K-Sr germanates, $Na_{0.36}Sr_{0.82}Ge_4O_9$ (**1**), $Na_2SrGe_6O_{14}$ (**2**), and $K_2SrGe_8O_{18}$ (**3**) while **2** and **3** adopt known structural types with primitive unit cells, **1** demonstrates a rare example of the Ge polyhedra connection and has a rhombohedral lattice. The new phases doped with Pr^{3+} (**2**) and Mn^{4+} (**2** and **3**) exhibit the red emission upon UV excitation. The phosphorescence intensity of the Mn^{4+} doped $Na_2SrGe_6O_{14}$ (**2**) and $K_2SrGe_8O_{18}$ (**3**) was optimized by adjusting the doping level. The temperature dependent phosphorescence spectra of $K_2SrGe_{7.995}O_{18}$: $0.005Mn^{4+}$ showed that the material loses half of the intensity at 420 K, which is at the normal LED lamps operating temperature range. Further research should focus on the application of the $K_2SrGe_8O_{18}$ (**3**) phase, rather than the $Na_2SrGe_6O_{14}$ (**2**) compound. Furthermore, the $Na_2SrGe_6O_{14}$ (**2**) phase also exhibits non-linear optical properties, yet the SHG activity of the phase is low.

6.5 Supplementary information

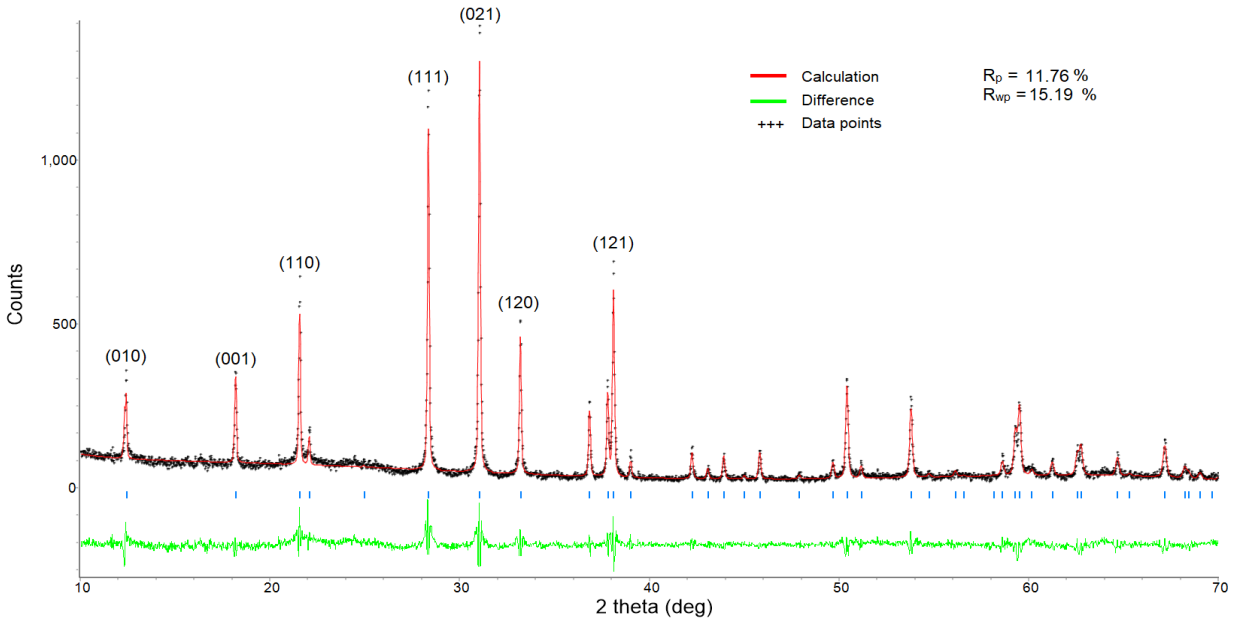

Figure 6.11. Rietveld refinement of the $Na_2SrGe_{5.992}O_{14}$: $0.008Mn^{4+}$ sample.

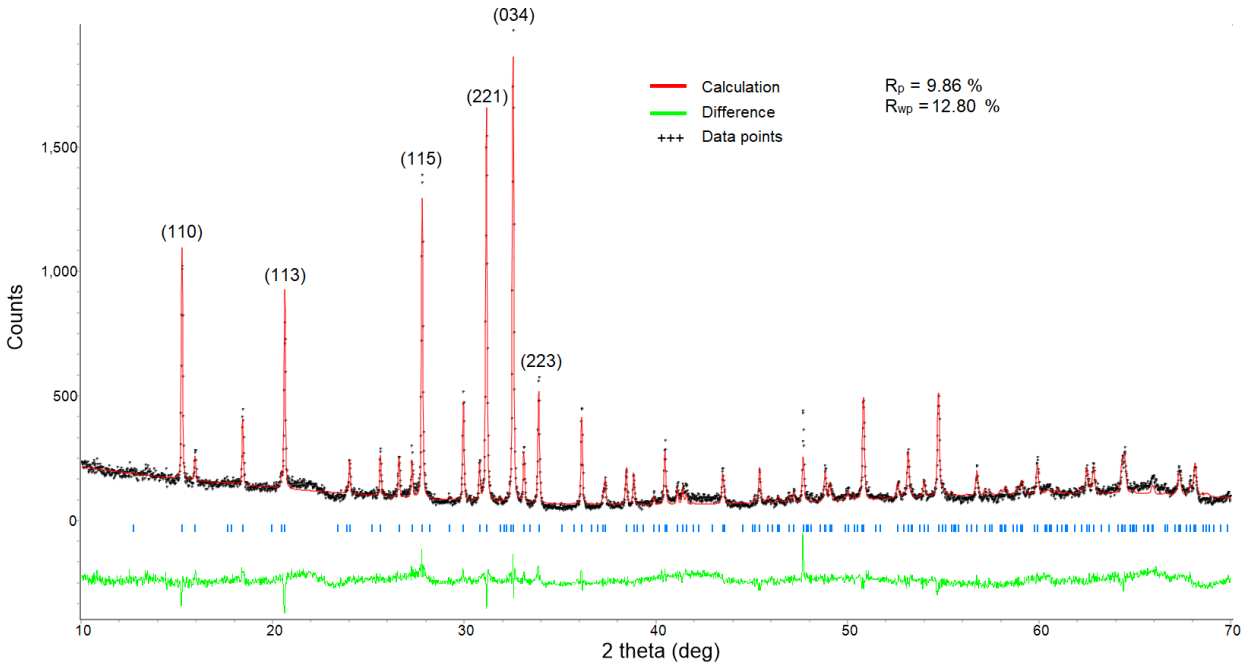

Figure 6.12. Rietveld refinement of the $K_2SrGe_{7.995}O_{18}$: $0.005Mn^{4+}$ sample.

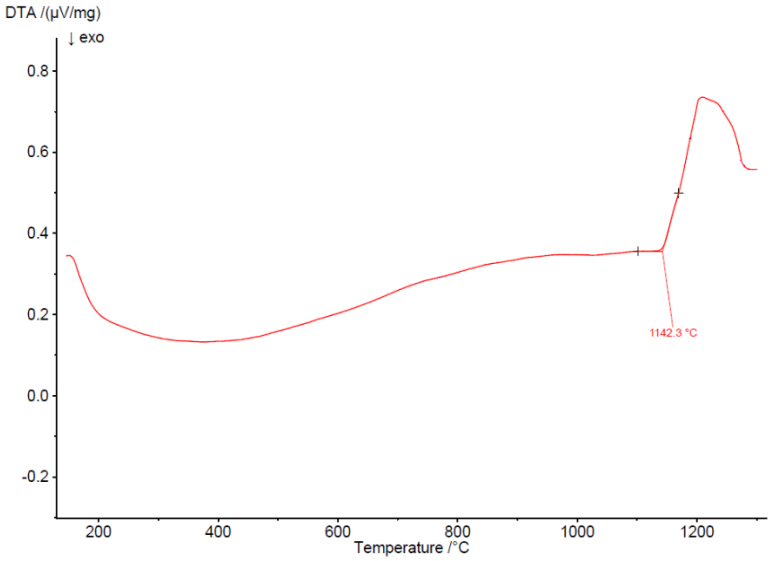

Figure 6.13. DTA curve (heating) for the $SrGe_4O_9$ phase. Sample starts melting at 1142 °C. There is no indication of phase transitions prior the melting point.

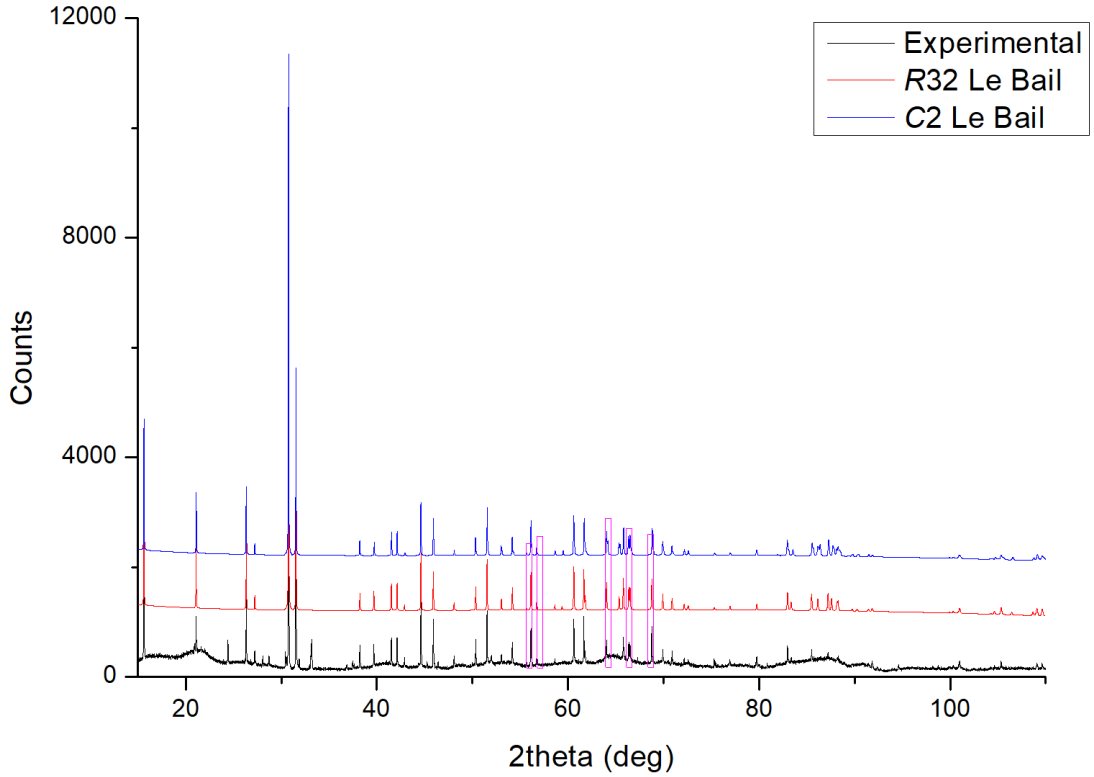

Figure 6.14. Experimental data and the Le Bail simulation (*R*32 and *C*2 space groups) for $Na_{0.36}Sr_{0.82}Ge_4O_9$.

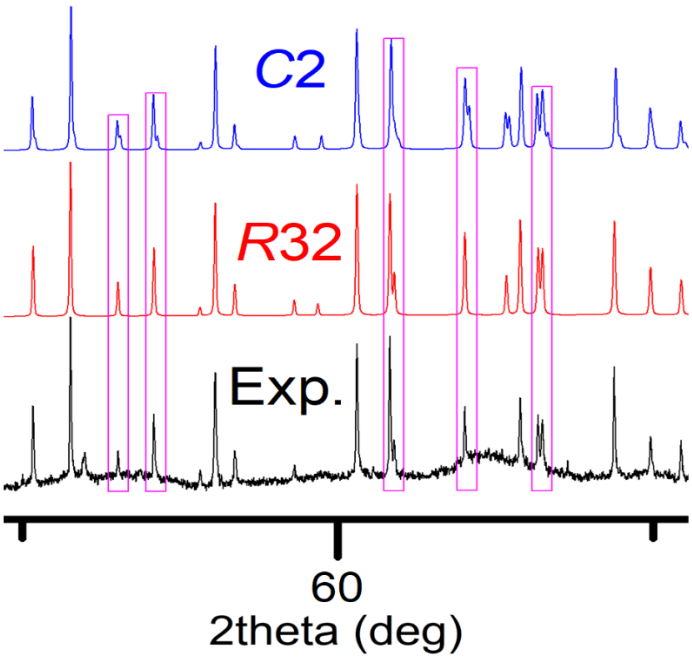

Figure 6.15. Fragment of the Figure S1 at 50–80° 2θ range. The features of experimental peaks (black) matching the *R*32 Le Bail model (red), but not the *C*2 model (blue).

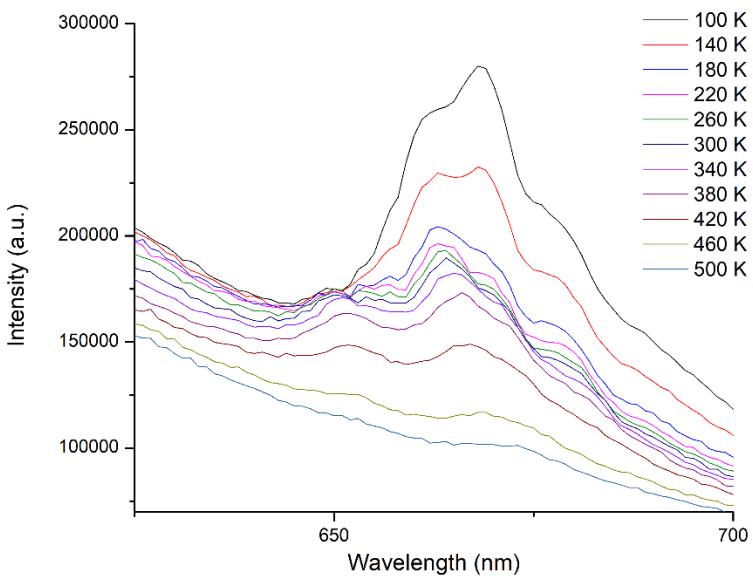

Figure 6.16. Temperature dependent emission spectra of $Na_2SrGe_{5.992}O_{14}$: $0.008Mn^{4+}$ sample in the 100-500 K range

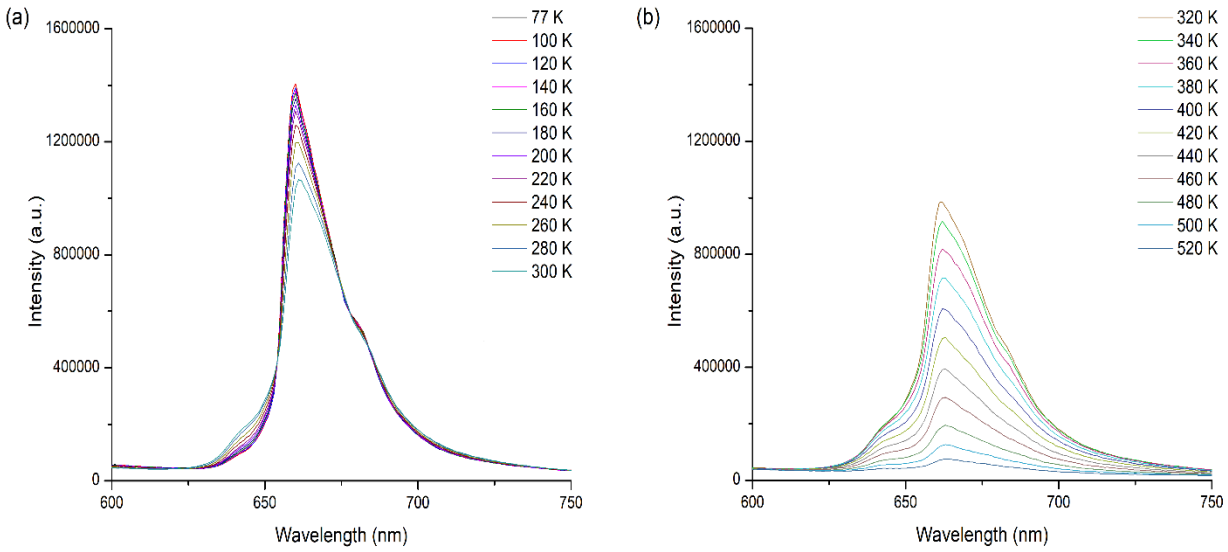

Figure 6.17. Temperature dependent emission spectra of the $K_2SrGe_{7.995}O_{18}$: $0.005Mn^{4+}$ sample in two temperature regions (for clarity): 77-300 K (a) and 320-520 K (b)

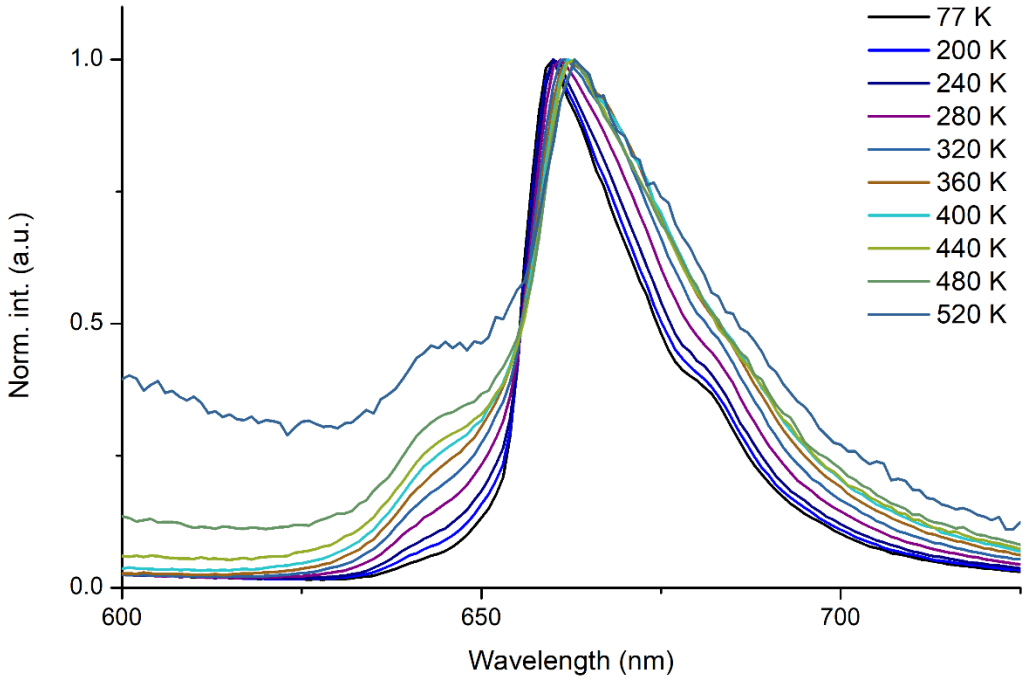

Figure 6.18. Normalized temperature dependent emission spectra of the $K_2SrGe_{7.995}O_{18}$: $0.005Mn^{4+}$ sample in 77-520 K range.

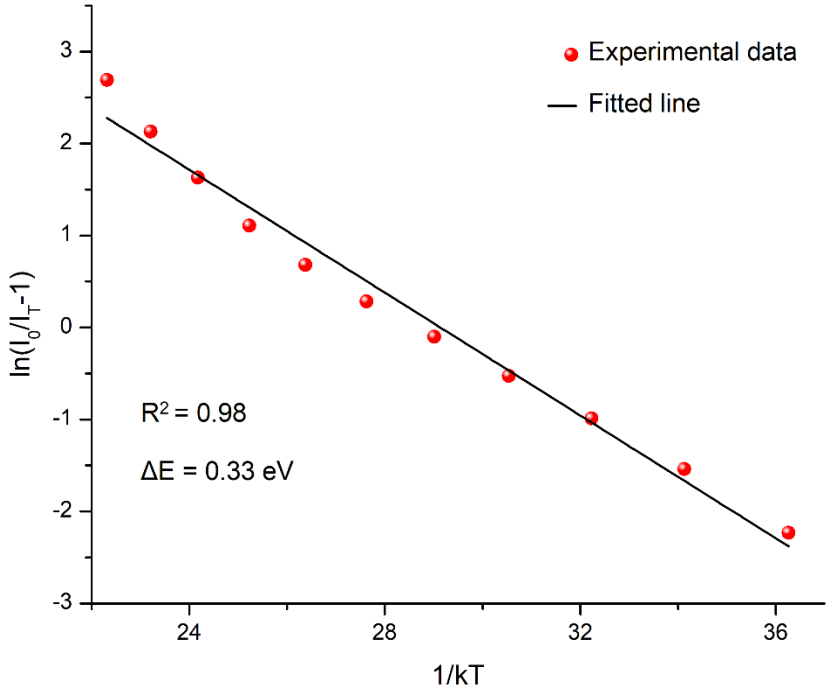

Figure 6.19. Linear fitting of the $\ln(I_0/I_T-1)$ versus 1/kT data for the $K_2SrGe_{7.995}O_{18}$: $0.005Mn^{4+}$ sample.

Chapter 7. Conclusions and future work

The dissertation was focused on the preparation and characterization of the new germanate phases. Firstly, we aimed to unravel some uncertainties in the structural data on the magnesium fluorogermanates. Then, the halogen-germanate series was expanded to the strontium and barium compounds. Next, the phases, featuring extended anionic frameworks based on the GeO_n polyhedra (n = 4 or 6), were successfully synthesized. These phases (referred as "polygermanates") were explored for the emission of red light under the UV excitation. The synthesis conditions were established and optimized for new germanate phosphors.

7.1 Magnesium fluorogermanates

The solid-state reaction between MgO, GeO_2, and MgF_2 produces various compounds depending on the reagent ratio. Among these compounds, the $Mg_{28}Ge_{7.5}O_{38}F_{10}$ phase activated with Mn^{4+} was used as a red phosphor for many decades. The reports on the other magnesium fluorogermanates were scarce and no crystal structures were reported. We were able to prepare a new phase, $Mg_3Ge_{1-\delta}O_{4(1-\delta)}F_{2(1+2\delta)}$, featuring notable germanium deficiency in the structure. Note that the $Mg_{28}Ge_{7.5}O_{38}F_{10}$ is deficient as well. The reason for the deficiency is a partial oxygen for fluorine substitution, creating a charge imbalance. Additionally, the other magnesium fluorogermanates related to the humite mineral series with the $n(Mg_2GeO_4)\cdot MgF_2$ (n = 2, 3, 4) general composition were predicted[38]. More research is required to confirm their existence and to study the trends in the structural deficiencies.

7.2 R^{2+} halogen-germanates (R^{2+} = Sr^{2+} or Ba^{2+})

This research was not limited to the magnesium fluorogermanates. More halogen-germanates, namely $Sr_3GeO_4Cl_2$, $Ba_3GeO_4Br_2$, $Sr_6Ge_2O_7Cl_6$, and $Ba_5GeO_4Br_6$, were prepared via solid-state reactions or by the application of the halide fluxes. These materials feature intriguing mixed oxygen-halogen coordination of the alkaline earth cations. From the practical point of view, the doping of the large alkaline earth sites with the rare-earth cations should be possible in the new compounds yielding luminescent materials. Of particular interest would be the doping with Eu^{2+} as this cation is known for a tunable emission wavelength depending on the covalency of the surrounding. Before that, however, the preparation routine for the phase-pure Sr and Ba halogen-germanates needs to be established, which was not done in our research.

7.3 New germanates with extended anionic frameworks

Unlike the revised $Mg_{28}Ge_{7.5}O_{38}F_{10}$ phase, the new halogen-germanates synthesized in this research contain only tetrahedrally coordinated germanium atoms. The GeO_4 pohyhedra do not form extended anionic frameworks – instead there are just GeO_4 monomers and Ge_2O_7 dimers. Since our primary focus was on the luminescence of the Mn^{4+} doped oxides, the presence of the GeO_6 units in the structure of the new compounds was essential. Due to this, the following phases prepared in this research are of great interest: $Na_2BaGe_8O_{18}$, $Rb_2BaGe_8O_{18}$, $K_2SrGe_8O_{18}$ octagermanates and $Na_2SrGe_6O_{14}$ hexagermanate. Initially obtained as single crystals, these phases contain germanium atoms in both octahedral and tetrahedral oxygen surroundings with GeO_n units sharing vertices and forming infinite frameworks.

The octagermanates are isostructural and possess their own structure type, with $K_2Ba(Ge_4O_9)_2$ being the first reported compound of the series[98]. The $Na_2SrGe_6O_{14}$ phases adopts

the common $Ca_3(Ga_2Ge)Ge_3O_{14}$ structure. The octagermanates feature unique way of the germanium polyhedra connection distinct from the alkali metals tetragermanates and alkaline earth tetragermanates. Moreover, $R_2Ge_4O_9$ and RGe_4O_9 tetragermanates are related to the naturally occurring minerals – catapleite ($Na_2ZrSi_3O_9 \cdot 2H_2O$) and benitoite ($BaTiSi_3O_9$) respectively, while there is no such correspondence for the octagermantes.

As intentioned, the luminescent materials were prepared from $Na_2BaGe_8O_{18}$, $Rb_2BaGe_8O_{18}$, $K_2SrGe_8O_{18}$ and $Na_2SrGe_6O_{14}$ by a partial substitution of Ge^{4+} for Mn^{4+}, and the corresponding luminescence spectra were collected. The level of the substitution was optimized for a better performance. The emission from the new phosphors is in the far-red region, typical for the oxide materials. Considering the preparation routine and cost, further investigation should be focused on the Mn^{4+} activated $K_2SrGe_8O_{18}$. The Pr^{3+} activated $Na_2SrGe_6O_{14}$ also requires further investigation, namely temperature-dependent luminescence property measurements.

The follow-up research on the $K_2SrGe_8O_{18} : Mn^{4+}$ should look at its quantum efficiency. Additionally, the actual white LED should be fabricated, and the produced white light should be tested for color rendering.

As we can see, there are minerals related to some germanates structures, but not to the octagermanates. What we can learn from the nature is that GeO_4 is a structural resemblance of SiO_4, while GeO_6 unit resembles ZrO_6 or TiO_6 in the structure of the corresponding minerals. If we seek for the wide-scale applications and cost efficiency in the octagermanate series, we can try to synthesize analogues of the germanates by replacing Ge (low abundant element) for much more available Si, Ti, Zr, Sn etc. The new phases will have to be tested for the luminescent performance.

Appendix A1. Energy levels of octahedrally coordinated activator

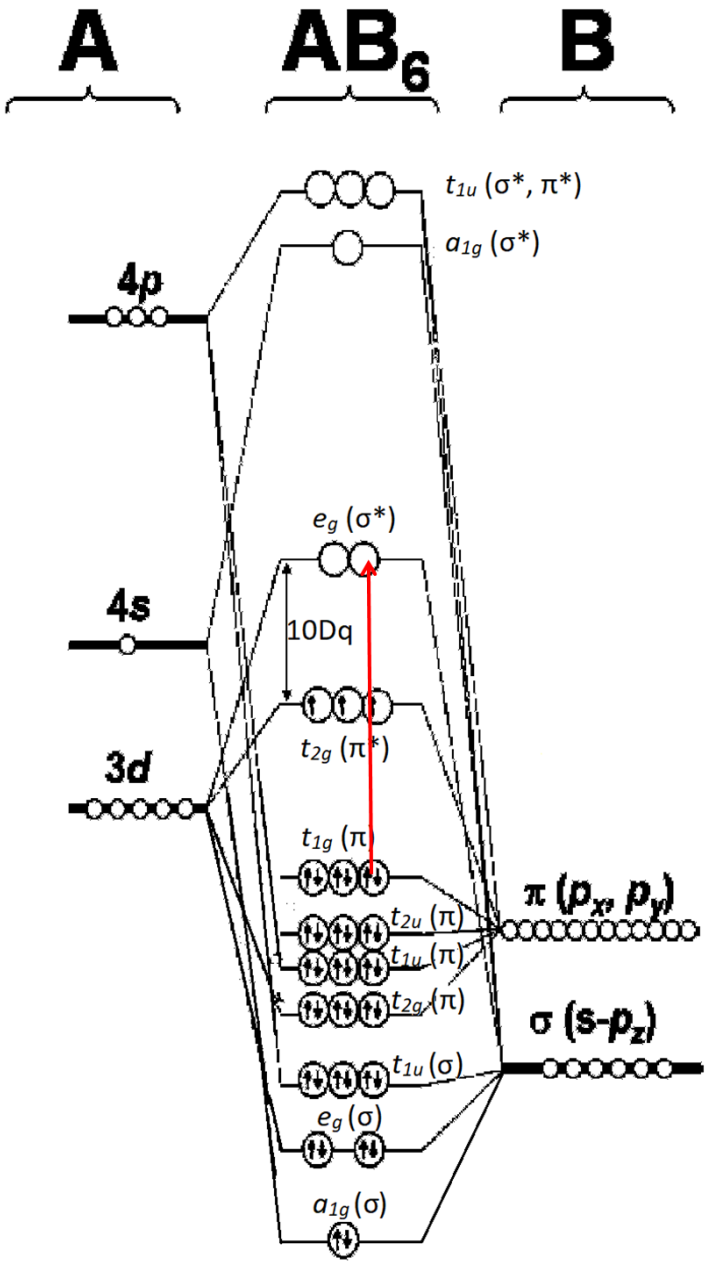

Figure A1.1 The energy levels of the octahedrally coordinated activator A in terms of the molecular orbital theory[5,147]. The "ligand-to-metal" charge transfer transition is shown by red arrow.

Appendix A2. $Na_4Sn_2Ge_5O_{16}$ structure and Na^+ ionic conductivity in the $Na_{4-x}Sn_{2-x}Sb_xGe_5O_{16}$ series

This chapter contains unpublished data on the structure of the $Na_4Sn_2Ge_5O_{16}$ phase and the ionic conductivity of the Sb-doped $Na_{4-x}Sn_{2-x}Sb_xGe_5O_{16}$ samples (x = 0, 0.05, 0.10, 0.15, 0.25, 0.30, 0.35). The candidate synthesized and characterized the new material by means of XRD, prepared a series of the pristine and Sb-doped samples for the electrical impedance measurements, wrote the part of manuscript covering these results. The electrical impedance measurements, data interpretation and writing were done by Christopher J. Franko. The DFT calculations were provided by Zan Yang. The study requires additional data before submission to a peer-reviewed journal.

New $Na_4Sn_2Ge_5O_{16}$ phase was characterized with single crystal X-ray diffraction. Data analysis demonstrated a potential Na^+ ionic conductivity in the new phase. To achieve a higher conductivity through increase in the Na^+ mobility, Sn^{4+} atoms in the structure were partially substituted for Sb^{5+} yielding a lower concentration of the Na^+ ions. A series of the $Na_{4-x}Sn_{2-x}Sb_xGe_5O_{16}$ (x = 0, 0.05, 0.10, 0.15, 0.25, 0.30, 0.35) samples was prepared via solid-state reactions, and electrical impedance spectroscopy (EIS) data were collected in the 25-200 °C range. Bond-valence energy landscape calculations were used to investigate the Na^+ conductivity pathways in $Na_4Sn_2Ge_5O_{16}$.

A2.1 Introduction

Nowadays small electronics (cell phones, tablets, laptops) as well as electric vehicles rely on the rechargeable lithium-ion batteries (LIB). Moreover, wind and solar electrical energy production depends on the energy storage technologies since the solar and wind output is weather dependent. The excess of energy from the sustainable sources should be stored to provide a constant supply to the power grid irrespectively of the weather conditions. Rechargeable batteries can be used to store the energy[148]. The increasing energy demands and high cost of the LIB components stimulated interest in the alternatives to LIB, such as sodium-ion[149–151] and multivalent ion batteries[152–154]. Historically, the LIB outperformed the sodium batteries because of the superior intercalation of lithium into the electrode materials – $LiCoO_2$ and graphite[151]. Search for similar materials for the sodium-ion batteries is an ongoing challenge[149–151,155–157]. While electrode materials for the sodium-ion batteries draw a huge attention, the other crucial component – a suitable electrolyte – is yet to be discovered. The potential electrolytes can be liquids (solvents or ionic liquids), gels, or solid phases (polymers or inorganic compounds)[158–161]. In terms of safety,

solid electrolytes are preferred over liquid ones, since the latter may leak from a battery causing significant damage.

Oxide-based materials are commonly considered as promising solid electrolytes due to their high chemical and thermal stability. The structures of the oxide-based electrolytes are divided into "layered" materials and materials featuring extended 3D frameworks. Examples of the "layered" materials include the Li_2SnO_3-type phases and β-alumina, while the most known 3D materials belong to the NASICON family[162,163].

Inorganic Crystal Structure Database (ICSD)[25] contains 56 entries on the Li_2SnO_3 type oxides with the A_2BO_3 general formula (*A* – mostly Li or Na, *B* – various p-, d-, or f-elements). In the Li_2SnO_3 structure, two types of the alternating layers can be distinguished: layers made from both SnO_6 and LiO_6 octhahedra and layers built from LiO_6 polyhedra exclusivelly[164]. Li^+ ions here support the overall 3D framework.

The discovery of the ionic conductivity in the non-stoichiometric Na-Al oxides, referred as β-Al_2O_3 and β″-Al_2O_3, was extremely important for the Na ion batteries[165–168]. These two structures are sometimes referred as "layered" too. Indeed, the alternating Al-O and Na-O layers can be distinguished in their structures, however the Al-O-Al bridges between the neighboring Al-O layers connecting these layers into infinite frameworks[166,168].

Various NASICON-type electrolytes are a broad group of the 3D oxide-based Na^+ ion conductors, originally reported in 1976[162,163]. The anionic framework of the original $NaZr_2P_3O_{12}$ structure is built from the corner-sharing ZrO_6 octahedra and PO_4 tetrahedra, while the Na ions occupy the channels of the framework. The composition, structure and properties of the NASICON type phases can be tuned within a very broad range by the chemical substitution[169,170].

In the present work we report synthesis and structure of the new 3D sodium ion conductor, $Na_4Sn_2Ge_5O_{16}$, and the ion conductivity study of the $Na_{4-x}Sn_{2-x}Sb_xGe_5O_{16}$ (x = 0, 0.05, 0.10, 0.15, 0.25, 0.30, 0.35) series. The structure of $Na_4Sn_2Ge_5O_{16}$ was determined from single crystal X-ray diffraction (XRD) data and feature an anionic framework built on the SnO_6 and GeO_4 polyhedra. The patrial Sn^{4+} substitution for Sb^{5+} improved the ion conductivity, and the highest conductivity value was achieved for the $Na_{3.80}Sn_{1.80}Sb_{0.20}Ge_5O_{16}$ sample. The $Na_4Sn_2Ge_5O_{16}$ phase can be a prototype for the new family of the Na^+ ion conductors.

A2.2 Methods

A2.2.1 Synthesis of the $Na_4Sn_2Ge_5O_{16}$ single crystals

Crystals of the $Na_4Sn_2Ge_5O_{16}$ phase were obtained from the reaction between Na_2CO_3 (98 wt.%), $SrCO_3$ (99 wt.%), SnO_2 (99.9 wt.%), and GeO_2 (99.999 wt.%) in the 2 : 1 :1 : 5 molar ratio. The powders were mixed in an agate mortar and pressed into pellet with a steel die. The pellet was placed in a platinum crucible and heated to 1050 °C at the 200 °/ h rate in a box furnace. After 2 hours at 1050 °C, the furnace was cooled down to 900 °C at 100 °/ h and then to 800 C at 10 °/ h. The further cooling was done by switching of a furnace. $Na_4Sn_2Ge_5O_{16}$ crystals were picked manually from the reaction products and studied with single crystal XRD.

A2.2.2 Single crystal XRD

Single crystal XRD (Mo Kα radiation) were carried out on a STOE IPDS II diffractometers equipped with an image plate detector. The absorption correction was performed based on the optimization of the crystal shape against the equivalent reflections (X-shape software[39]). The structures were solved by intrinsic phasing (SHELXT[28], Olex2[42]) and refined by the full-matrix least squares method against F^2 in an anisotropic approximation (SHELXL[43]).

A2.2.3 Synthesis of the $Na_{4-x}Sn_{2-x}Sb_xGe_5O_{16}$ series (x = 0, 0.05, 0.10, 0.15, 0.25, 0.30, 0.35)

The preparation of the $Na_{4-x}Sn_{2-x}Sb_xGe_5O_{16}$ samples (x = 0, 0.05, 0.10, 0.15, 0.25, 0.30, 0.35) was done by solid-state reaction between $Na_2Sn(OH)_6$ (98 wt. %), GeO_2 (99.999 wt. %), and $NaSbO_3$. Ball milling in the isopropanol medium was used to grind and mix the reagents. After the complete isopropanol removal, the powder was pressed, and the pellet was placed in a platinum crucible. This crucible was heated to 1050 °C at 100 °/h in a box furnace and sintered at this temperature for 24 hours. After this the furnace was switched off and the product purity was tested with powder XRD.

A2.2.4 Powder XRD

To confirm the formation of the $Na_{4-x}Sn_{2-x}Sb_xGe_5O_{16}$ phases and study their purity, powder XRD data were collected on a PANalytical X'Pert PRO diffractometer ($CuK\alpha_1$ radiation) equipped with the Ge monochromator. Rietveld refinements of the data were done with the Rietica software[44].

A2.2.5 Calculations

Density functional theory calculations were performed via the Quantum Espresso software[171,172]. The exchange-correlation energy was in the form of Predew-Burke-Ernzerfhof (PBE) pseudopotentials based on generalized gradient approximation (GGA) and projector-augmented wave (PAW) technique was chosen to model the electron-ion interaction[173–175]. The cutoff energy for the wave function was set to 80 Ry, and a 12 × 6 × 4 k mesh was adopted for the Brillouin zone integration. Both cell parameters and atomic positions were fully relaxed until the force on each atom is less than 10^{-4} eV/ Å.

The relaxed structure was used to illustrate the diffusion paths and estimate the migration energy barriers for the Na^+ cations in the $Na_4Sn_2Ge_5O_{16}$ crystal structure. Bond valence (BV)

maps[176] and bond-valence energy landscapes (BVEL)[177–179] for the Na^+ cations were calculated with Bond_Str program implemented within the FullProf Suite[180] and visualized with Vesta[181].

A2.3 Results and Discussion

A2.3.1 Crystal structure

The $Na_4Sn_2Ge_5O_{16}$ phase crystallizes with the *Pbcn* space group, $Z = 4$ (Table 1). There is a sole Sn 8*d* general position in the structure, three germanium sites – two *8d* (Ge1 and Ge3) and one special *4c* (Ge2), three sodium sites– one *8d* (Na1) and two *4c* (Na2 and Na3). Sn atoms in are surrounded by six oxygen atoms in a distorted octahedral manner, while Ge and oxygen atoms form GeO_4 tetrahedra.

Table A2.1. Selected crystallographic data and refinement results for $Na_4Sn_2Ge_5O_{16}$

Formula	$Na_4Sn_2Ge_5O_{16}$
Formula weight	948.29
Crystal system	Orthorhombic
Space group	*Pbcn*
a, Å	6.5063(13)
b, Å	11.912(2)
c, Å	18.995(4)
Volume, Å^3	1472.2(5)
Z	4
ρ_{calcg}, cm^3	4.278
μ/mm^{-1}	13.613
F(000)	1728.0
Radiation	MoKα (λ = 0.71073)
2θ range, °	6.842 - 70.012
Index ranges	$-10 \leq h \leq 10$, $-19 \leq k \leq 18$, $-30 \leq l \leq 28$
Reflections collected	23211
Data /restraints/ parameters	3225/0/124
GOOF	1.041
R_1 (I>2σ (I))	0.0542
Largest diff. peak/hole, e/Å^3	1.91/-3.58

Corner-sharing germanium polyhedra form quite rare $Ge_5O_{16}^{12-}$ polyanionic chains in the $Na_4Sn_2Ge_5O_{16}$ structure. These chains stack parallel the *bc* plane of the unit cell (Figure A2.1). Each SnO_6 octahedron connects four Ge_5O_{16} units through corner sharing to form a 3D anionic framework with Na^+ cations located in the channels of the framework. The Na2 and Na3 atoms occupy the same type of channels marked as A, while Na1 atoms – different channels marked as B in Figure A2.1.

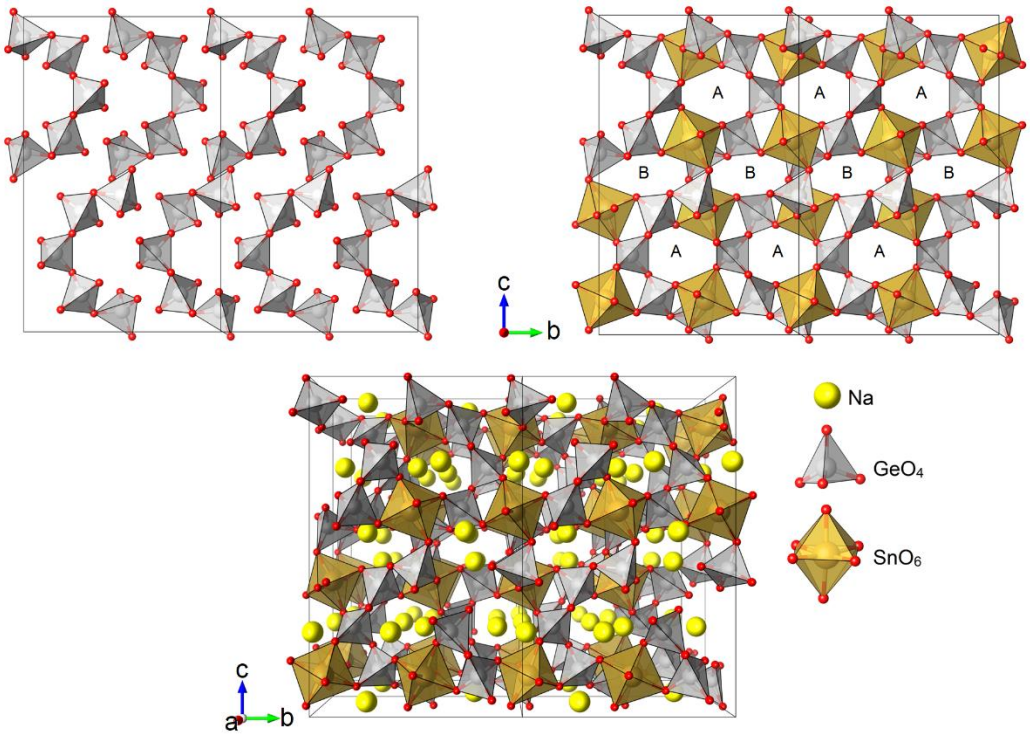

Figure A2.1 (top left) $Ge_5O_{16}^{12-}$ polyanions stacking in the $Na_4Sn_2Ge_5O_{16}$ structure; (top right) anionic framework built on GeO_4 and SnO_6 units in the $Na_4Sn_2Ge_5O_{16}$ structure; (bottom center) Na^+ cations in the channels of the anionic framework.

ISCD contains entries on two phases structurally related to $Na_4Sn_2Ge_5O_{16}$. The phases – $Na_4Sn_2Ge_5O_{16}{\cdot}H_2O$ (ICSD #20545) and $Na_4Sn_2Si_5O_{16}{\cdot}H_2O$ (ICSD #20551) – were obtained via hydrothermal synthesis at 450 °C and 1000 atm of pressure[182,183]. As we can see, the hydrated compounds have lower symmetry compared to $Na_4Sn_2Ge_5O_{16}$: the silicate crystalizes with the *C*2/*c* space group, while the germanate – with the acentric *P*2 group. Like $Na_4Sn_2Ge_5O_{16}$, the structures

of the hydrothermally obtained compounds contain T_5O_{16} polyanions (T = Si or Ge) connected by the SnO_6 octahedra into infinite frameworks and Na atoms (and water molecules) occupying the channels of the frameworks. Geometric configuration of the polyanions differs between the three compounds. In $Na_4Sn_2Ge_5O_{16}\cdot H_2O$ and $Na_4Sn_2Si_5O_{16}\cdot H_2O$ the T_5O_{16} groups are almost linear with the distances between the terminal T atoms of ~11.0 Å and ~11.6 Å for the Si and Ge, respectively. In the $Na_4Sn_2Ge_5O_{16}$, the T_5O_{16} units are curved, so the terminal Ge atoms are at ~7.5 Å from each other. The way the polyanions and SnO_6 groups are connected changes between the three structures. In the hydrated phases, each SnO_6 connects six TO_4 tetrahedra from five T_5O_{16} units through the corner sharing, so only one 6-membered SnT_2O_3 cycle forms (Figure A2.2). As we mentioned before, in the $Na_4Sn_2Ge_5O_{16}$ structure each SnO_6 unit connects four T_5O_{16} units and two $SnGe_2O_3$ cycles form instead of one (Figure A2.2).

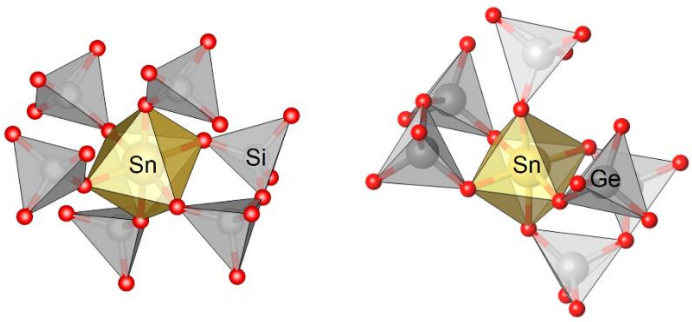

Figure A2.2 SnO_6 and TO_4 (T = Si or Ge) polyhedra connection in the $Na_4Sn_2Si_5O_{16}\cdot H_2O$ (left) and $Na_4Sn_2Ge_5O_{16}$ (right) structures. One SnT_2O_3 cycle forms in silicate, while two cycles form in the germanate.

A2.3.2 Na^+ ionic conductivity

The Na^+ ionic conductivity of the $Na_{4-x}Sn_{2-x}Sb_xGe_5O_{16}$ samples was measured using EIS. The electrochemical impedance spectra of the pristine $Na_4Sn_2Ge_5O_{16}$ sample and the doped $Na_{3.8}Sn_{1.8}Sb_{0.2}Ge_5O_{16}$ one, as well as the corresponding equivalent circuit model fits, are shown in Figures A2.3a and A2.3b respectively. Each spectrum shows the expected features of a solid-state ion conductor, including the high frequency semi-circle representing the bulk conductivity and

capacitance, as well as the low frequency tail representing unideal Warburg diffusion. In both samples the capacitance is not ideal, giving depressed semi-circles. This depression is likely the result of the natural inhomogeneity of ceramic conduction grains, leading to a dispersion in the distribution of grain boundary resistances. This dispersion may result in the grain boundaries acting as so-called "leaky capacitors", causing the aforementioned semi-circle depression[184]. The extent of these grain boundary effects appears to be larger in the $Na_{3.8}Sn_{1.8}Sb_{0.2}Ge_5O_{16}$ phase than in the undoped analogue.

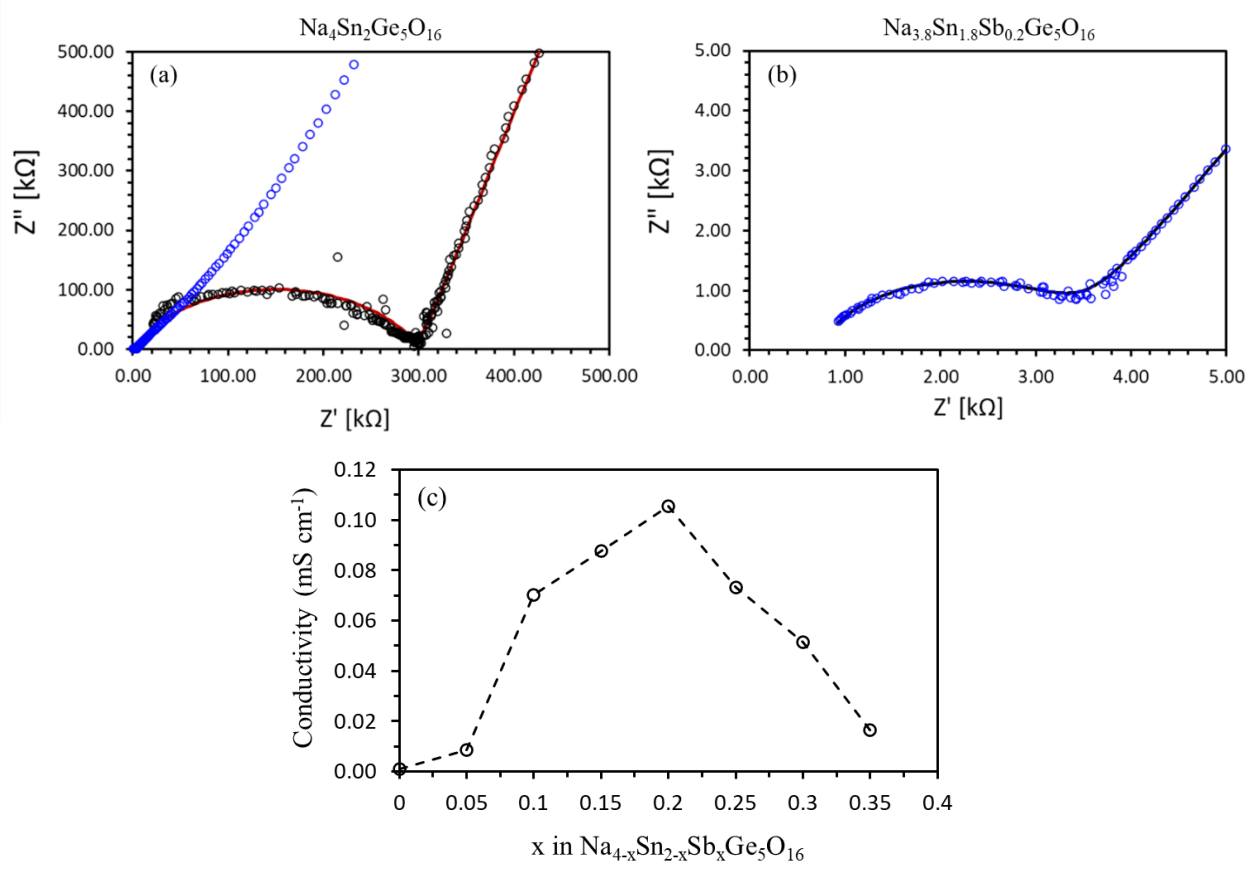

Figure A2.3 (a) EIS spectrum (black circles) and corresponding equivalent circuit model fit (red line) of the undoped $Na_4Sn_2Ge_5O_{16}$ phase. The EIS spectrum of the doped $Na_{3.8}Sn_{1.8}Sb_{0.2}Ge_5O_{16}$ phase is included for comparison (blue circles). (b) EIS spectrum of the $Na_{3.8}Sn_{1.8}Sb_{0.2}Ge_5O_{16}$, zoomed into the high frequency region (blue circles). As well as the corresponding equivalent circuit model fit (black line). (c) Ionic conductivity values of each $Na_{4-x}Sn_{2-x}Sb_xGe_5O_{16}$ phase.

The obtained Na^+ ionic conductivity is plotted as a function of the Sb content (x in $Na_{4-x}Sn_{2-x}Sb_xGe_5O_{16}$) in Figure A2.3c. The undoped phase ($Na_4Sn_2Ge_5O_{16}$) expectedly gives the lowest bulk conductivity of 1.0 x 10^{-3} mS·cm^{-1}. As Sn^{4+} is substituted for Sb^{5+}, a stoichiometric number of the Na^+ vacancies is created in order to conserve the charge balance. The Na^+ vacancies facilitate the Na^+ migration. As a result, the conductivity increases significantly as more Sb^{5+} is doped into the structure. The ionic conductivity of 0.11 mS·cm^{-1} is reached in the $Na_{3.8}Sn_{1.8}Sb_{0.2}Ge_5O_{16}$ (x = 0.2) phase at room temperature, and the maximum conductivity measured for this phase is 1.6 mS·cm^{-1} at 200 °C. At higher Sb^{5+} doping levels, the creation of vacancies begins to have the opposite effect as the number of charge carriers is significantly reduced, and the ionic conductivity begins to fall.

A room temperature conductivity of the $Na_{3.8}Sn_{1.8}Sb_{0.2}Ge_5O_{16}$ phase is similar to that of other Na-conductors (~10^{-1} mS·cm^{-1}) studied for use in Na-ion solid state cells[185]. The large difference in conductivity values between this sample and the undoped phase is highlighted in Figure A2.3a, where only the high-frequency Warburg tail of the $Na_{3.8}Sn_{1.8}Sb_{0.2}Ge_5O_{16}$ is visible when overlaid with the EIS spectrum of $Na_4Sn_2Ge_5O_{16}$.

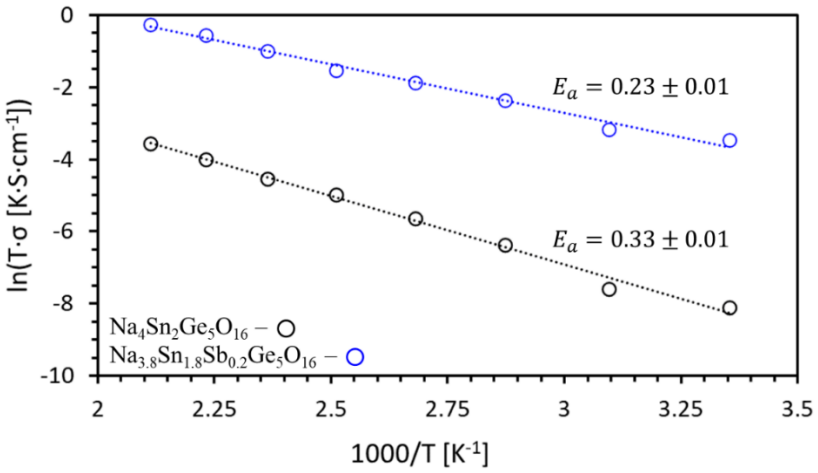

Figure A2.4 Temperature dependent ionic conductivity measurements of $Na_4Sn_2Ge_5O_{16}$ (black) and $Na_{3.8}Sn_{1.8}Sb_{0.2}Ge_5O_{16}$ (blue), with the corresponding activation energies obtained from the slope.

In order to probe the mechanism of conduction from this new phase, further temperature dependent ionic conductivity was measured for both the undoped $Na_4Sn_2Ge_5O_{16}$ and the most conductive $Na_{3.8}Sn_{1.8}Sb_{0.2}Ge_5O_{16}$ phases. The corresponding Arrhenius plots are shown in Figure A2.4. As expected, the ionic conductivity increases with temperature for both phases. The activation energy for conduction is extracted from the slope of the linear fit and found to be 0.33 ± 0.01 eV for the undoped phase, and 0.23 ± 0.01 eV for the optimally doped phase.

A2.3.3 BVEL calculations

Na^+ migration pathways from the BVEL calculations for the $Na_4Sn_2Ge_5O_{16}$ structure are shown in Figure A2.5. The diffusion of the Na^+ cations is possible in two dimensions with small energy barriers of 0.30 eV and 0.36 eV along the *a* and *b* directions, respectively, which agrees well with the activation energies obtained from the EIS as discussed above. The 3D migration requires much a higher activation energy of 1.14 eV.

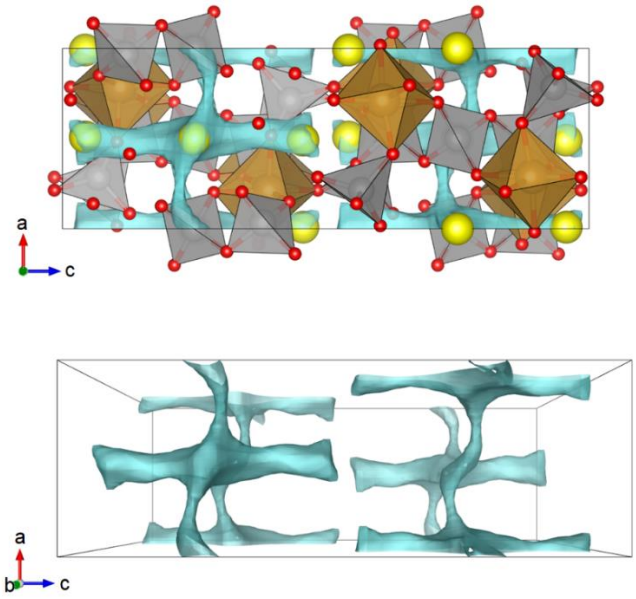

Figure A2.5 (top) Na^+ conduction pathways in the $Na_4Sn_2Ge_5O_{16}$ unit cell viewed on the *b* direction; (bottom) 2D Na^+ conduction pathways in the $Na_4Sn_2Ge_5O_{16}$ unit cell with atoms omitted for clarity.

Appendix A3. Single exponential fit of the decays for the $Rb_2BaGe_{8-x}O_{18}$: xMn^{4+} phosphors

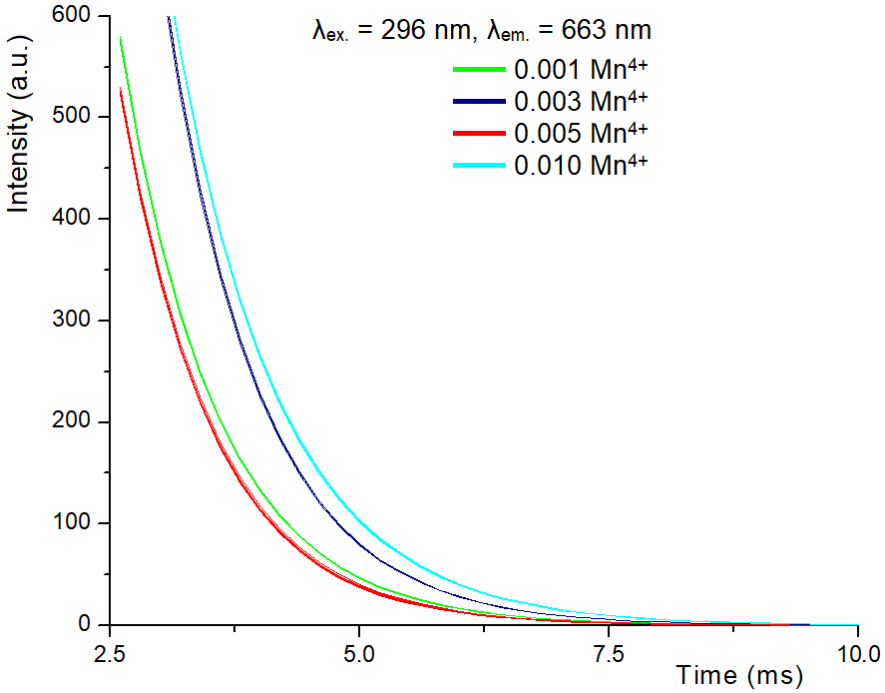

Figure A3.1 Single exponential fit of the luminescence decay curves for the $Rb_2BaGe_{8-x}O_{18}$: xMn^{4+} phosphors (x = 0.001, 0.003, 0.005, and 0.010).

References

(1) Blasse, G.; Grabmaier, B. C. *Luminescent Materials*; Springer-Verlag: Berlin Heidelberg, 1994.

(2) Henderson, B.; Imbusch, G. F. *Optical Spectroscopy of Inorganic Solids*; Monographs on the Physics and Chemistry of Materials; Oxford University Press: Oxford, New York, 2006.

(3) Powell, R. C. *Physics of Solid-State Laser Materials*; Atomic, Molecular and Optical Physics Series; Springer-Verlag: New York, 1998.

(4) Huang, K.; Rhys, A.; Mott, N. F. Theory of Light Absorption and Non-Radiative Transitions in F-Centres. *Proceedings of the Royal Society of London. Series A. Mathematical and Physical Sciences* **1950**, *204* (1078), 406–423. https://doi.org/10.1098/rspa.1950.0184.

(5) García Solé, J.; Bausá, L. E.; Jaque, D. *An Introduction to the Optical Spectroscopy of Inorganic Solids*; John Wiley & Sons, Ltd, 2005.

(6) Förster, Th. Zwischenmolekulare Energiewanderung und Fluoreszenz. *Annalen der Physik* **1948**, *437* (1–2), 55–75. https://doi.org/10.1002/andp.19484370105.

(7) Dexter, D. L. A Theory of Sensitized Luminescence in Solids. *J. Chem. Phys.* **1953**, *21* (5), 836–850. https://doi.org/10.1063/1.1699044.

(8) Morrison, C. A. *Crystal Fields for Transition-Metal Ions in Laser Host Materials*, 1st ed.; Springer Berlin, Heidelberg, 1992.

(9) Tanabe, Y.; Sugano, S. On the Absorption Spectra of Complex Ions. I. *J. Phys. Soc. Jpn.* **1954**, *9* (5), 753–766. https://doi.org/10.1143/JPSJ.9.753.

(10) Tanabe, Y.; Sugano, S. On the Absorption Spectra of Complex Ions II. *J. Phys. Soc. Jpn.* **1954**, *9* (5), 766–779. https://doi.org/10.1143/JPSJ.9.766.

(11) Tanabe, Y.; Sugano, S. On the Absorption Spectra of Complex Ions, III The Calculation of the Crystalline Field Strength. *J. Phys. Soc. Jpn.* **1956**, *11* (8), 864–877. https://doi.org/10.1143/JPSJ.11.864.

(12) Brik, M. G.; Srivastava, A. M. A Computation Study of Site Occupancy in the Commercial Mg28Ge7.55O32F15.04:Mn4+ Phosphor. *Optical Materials* **2016**, *54*, 245–251. https://doi.org/10.1016/j.optmat.2016.02.044.

(13) Brik, M. G.; Srivastava, A. M. Electronic Energy Levels of the Mn4+ Ion in the Perovskite, CaZrO3. *ECS J. Solid State Sci. Technol.* **2013**, *2* (7), R148–R152. https://doi.org/10.1149/2.020307jss.

(14) Thorington, L. Color-Corrected Light Source and Phosphors Therefor. US2748303A, May 29, 1956.

(15) Blasse, G.; Bril, A. A NEW PHOSPHOR FOR FLYING-SPOT CATHODE-RAY TUBES FOR COLOR TELEVISION: YELLOW-EMITTING $Y_3Al_5O_{12}$–Ce^{3+}. *Appl. Phys. Lett.* **1967**, *11* (2), 53–55. https://doi.org/10.1063/1.1755025.

(16) Nair, G. B.; Swart, H. C.; Dhoble, S. J. A Review on the Advancements in Phosphor-Converted Light Emitting Diodes (Pc-LEDs): Phosphor Synthesis, Device Fabrication and Characterization. *Progress in Materials Science* **2020**, *109*, 100622. https://doi.org/10.1016/j.pmatsci.2019.100622.

(17) Adachi, S. Review—Mn4+-Activated Red and Deep Red-Emitting Phosphors. *ECS J. Solid State Sci. Technol.* **2019**, *9* (1), 016001. https://doi.org/10.1149/2.0022001JSS.

(18) Thejas, K. K.; Abraham, M.; Kunti, A. K.; Tchernycheva, M.; Ahmad, S.; Das, S. Review on Deep Red-Emitting Rare-Earth Free Germanates and Their Efficiency as Well as Adaptability for Various Applications. *Applied Materials Today* **2021**, *24*, 101094. https://doi.org/10.1016/j.apmt.2021.101094.

(19) Shannon, R. D. Revised Effective Ionic Radii and Systematic Studies of Interatomic Distances in Halides and Chalcogenides. *Acta Cryst A* **1976**, *32* (5), 751–767. https://doi.org/10.1107/S0567739476001551.

(20) Gagné, O. C.; Hawthorne, F. C. Bond-Length Distributions for Ions Bonded to Oxygen: Metalloids and Post-Transition Metals. *Acta Cryst B* **2018**, *74* (1), 63–78. https://doi.org/10.1107/S2052520617017437.

(21) Williams, F. E. Some New Aspects of Germanate and Fluoride Phosphors*. *J. Opt. Soc. Am., JOSA* **1947**, *37* (4), 302–307. https://doi.org/10.1364/JOSA.37.000302.

(22) Thorington, L. Temperature Dependence of the Emission of an Improved Manganese-Activated Magnesium Germanate Phosphor. *J. Opt. Soc. Am., JOSA* **1950**, *40* (9), 579–583. https://doi.org/10.1364/JOSA.40.000579.

(23) von Dreele, R. B.; Bless, P. W.; Kostiner, E.; Hughes, R. E. The Crystal Structure of Magnesium Germanate: A Reformulation of Mg_4GeO_6 as $Mg_{28}Ge_{10}O_{48}$. *Journal of Solid State Chemistry* **1970**, *2* (4), 612–618. https://doi.org/10.1016/0022-4596(70)90058-7.

(24) Bless, P. W.; Von Dreele, R. B.; Kostiner, E.; Hughes, R. E. Anion and Cation Defect Structure in Magnesium Fluorogermanate. *Journal of Solid State Chemistry* **1972**, *4* (2), 262–268. https://doi.org/10.1016/0022-4596(72)90115-6.

(25) Hellenbrandt, M. The Inorganic Crystal Structure Database (ICSD)—Present and Future. *Crystallography Reviews* **2004**, *10* (1), 17–22. https://doi.org/10.1080/08893110410001664882.

(26) Baran, A.; Mahlik, S.; Grinberg, M.; Zych, E. High Pressure and Time-Resolved Luminescence Spectra of $Ca_3Y_2(SiO_4)_3$ Doped with Eu^{2+} and Eu^{3+}. *J. Phys.: Condens. Matter* **2012**, *25* (2), 025603. https://doi.org/10.1088/0953-8984/25/2/025603.

(27) Karle, J.; Hauptman, H. A Theory of Phase Determination for the Four Types of Non-Centrosymmetric Space Groups 1P222, 2P22, 3P12, 3P22. *Acta Cryst* **1956**, *9* (8), 635–651. https://doi.org/10.1107/S0365110X56001741.

(28) Sheldrick, G. M. SHELXT – Integrated Space-Group and Crystal-Structure Determination. *Acta Cryst A* **2015**, *71* (1), 3–8. https://doi.org/10.1107/S2053273314026370.

(29) Buerger, M. J. *Vector Space and Its Application in Crystal-Structure Investigation*; Wiley: New York, 1959.

(30) Wilson, A. J. C. Statistical Bias in Least-Squares Refinement. *Acta Cryst A* **1976**, *32* (6), 994–996. https://doi.org/10.1107/S0567739476002039.

(31) Pecharsky, V. K.; Zavalij, P. Y. *Fundamentals of Powder Diffraction and Structural Characterization of Materials, Second Edition*; Springer New York, NY, 2009.

(32) Rietveld, H. M. Line Profiles of Neutron Powder-Diffraction Peaks for Structure Refinement. *Acta Cryst* **1967**, *22* (1), 151–152. https://doi.org/10.1107/S0365110X67000234.

(33) Rietveld, H. M. A Profile Refinement Method for Nuclear and Magnetic Structures. *J Appl Cryst* **1969**, *2* (2), 65–71. https://doi.org/10.1107/S0021889869006558.

(34) Srivastava, A.; Comanzo, H.; Manivannan, V.; Setlur, A. A. Red Phosphors for Use in High CRI Fluorescent Lamps. US6965193B2, November 15, 2005.

(35) Soules, T.; Beers, W.; Greci, M.; Setlur, A.; Comanzo, H.; Manivannan, V.; Srivastava, A. Optimized Phosphor System for Improved Efficacy Lighting Sources. US7119488B2, October 10, 2006.

(36) Leverenz, H. W. Luminescent Material. US2066044, 1936.

(37) Robbins, C. R.; Levin, E. M. The System Magnesium Oxide-Germanium Dioxide. *Am J Sci* **1959**, *257* (1), 63–70. https://doi.org/10.2475/ajs.257.1.63.

(38) Lyon, S. R.; Ehlers, E. G. Phase Relations in the System MgO-GeO_2-MgF_2. *Journal of the American Ceramic Society* **1971**, *54* (7), 341–346. https://doi.org/10.1111/j.1151-2916.1971.tb12310.x.

(39) Stoe & Cie. X-AREA (Version 1.31), X-RED32 (Version 1.28b) and X-SHAPE (Version 2.05). *Stoe & Cie, Darmstadt, Germany* **2005**.

(40) SADABS. Bruker AXS Inc., Madison, Wisconsin, USA. **2008**.

(41) Sheldrick, G. M. A Short History of SHELX. *Acta Cryst A* **2008**, *64* (1), 112–122. https://doi.org/10.1107/S0108767307043930.

(42) Dolomanov, O. V.; Bourhis, L. J.; Gildea, R. J.; Howard, J. a. K.; Puschmann, H. OLEX2: A Complete Structure Solution, Refinement and Analysis Program. *J Appl Cryst* **2009**, *42* (2), 339–341. https://doi.org/10.1107/S0021889808042726.

(43) Sheldrick, G. M. Crystal Structure Refinement with SHELXL. *Acta Cryst C* **2015**, *71* (1), 3–8. https://doi.org/10.1107/S2053229614024218.

(44) Hunter, B. Rietica - A Visual Rietveld Program. *International Union of Crystallography Commission on Powder Diffraction Newsletter* **1998**, No. 20 (Summer).

(45) Gagné, O. C.; Hawthorne, F. C. Bond-Length Distributions for Ions Bonded to Oxygen: Alkali and Alkaline-Earth Metals. *Acta Cryst B* **2016**, *72* (4), 602–625. https://doi.org/10.1107/S2052520616008507.

(46) Zhen, N.; Wu, K.; Li, Q.; Pan, S.; Gao, W.; Yang, Z. Synthesis, Structures, and Properties of Two Magnesium Silicate Fluorides $Mg_5(SiO_4)_2F_2$ and $Mg_3SiO_4F_2$. *New J. Chem.* **2015**, *39* (11), 8866–8873. https://doi.org/10.1039/C5NJ01911G.

(47) Griffin, J. M.; Yates, J. R.; Berry, A. J.; Wimperis, S.; Ashbrook, S. E. High-Resolution 19F MAS NMR Spectroscopy: Structural Disorder and Unusual J Couplings in a Fluorinated Hydroxy-Silicate. *J. Am. Chem. Soc.* **2010**, *132* (44), 15651–15660. https://doi.org/10.1021/ja105347q.

(48) Nakamoto, K. *Infrared and Raman Spectra of Inorganic and Coordination Compounds, Part A, Theory and Applications in Inorganic Chemistry*, 6th Edition.; Wiley, 2009.

(49) Gabrielson, O. The Crystal Structures of Kentrolite and Melanotekite. *Arkiv foer Mineralogi och Geologi* **1962**, *3*, 141–151.

(50) Moore, P. B.; Sen Gupta, P. K.; Shen, J.; Schlemper, E. O. The Kentrolite-Melanotekite Series, $4Pb_2(Mn, Fe)_2^{3+}O_2[Si_2O_7]$: Chemical Crystallographic Relations, Lone-Pair Splitting, and Cation Relation to $8URe_2$. *American Mineralogist* **1991**, *76* (8), p1389–p1399.

(51) Dörsam, G.; Liebscher, A.; Wunder, B.; Franz, G. Crystal Structures of Synthetic Melanotekite ($Pb_2Fe_2Si_2O_9$), Kentrolite ($Pb_2Mn_2Si_2O_9$), and the Aluminum Analogue ($Pb_2Al_2Si_2O_9$). *American Mineralogist* **2008**, *93* (4), 573–583. https://doi.org/10.2138/am.2008.2594.

(52) Duan, C. J.; Wang, X. J.; Otten, W. M.; Delsing, A. C. A.; Zhao, J. T.; Hintzen, H. T. Preparation, Electronic Structure, and Photoluminescence Properties of Eu^{2+}- and Ce^{3+}/Li^{+}-Activated Alkaline Earth Silicon Nitride $MSiN_2$ (M = Sr, Ba). *Chem. Mater.* **2008**, *20* (4), 1597–1605. https://doi.org/10.1021/cm701875e.

(53) Hecht, C.; Stadler, F.; Schmidt, P. J.; auf der Günne, J. S.; Baumann, V.; Schnick, W. $SrAlSi_4N_7:Eu^{2+}$ − A Nitridoalumosilicate Phosphor for Warm White Light (Pc)LEDs with Edge-Sharing Tetrahedra. *Chem. Mater.* **2009**, *21* (8), 1595–1601. https://doi.org/10.1021/cm803231h.

(54) Sakuma, K.; Omichi, K.; Kimura, N.; Ohashi, M.; Tanaka, D.; Hirosaki, N.; Yamamoto, Y.; Xie, R.-J.; Suehiro, T. Warm-White Light-Emitting Diode with Yellowish Orange SiAlON Ceramic Phosphor. *Opt. Lett., OL* **2004**, *29* (17), 2001–2003. https://doi.org/10.1364/OL.29.002001.

(55) Yeh, C.-W.; Chen, W.-T.; Liu, R.-S.; Hu, S.-F.; Sheu, H.-S.; Chen, J.-M.; Hintzen, H. T. Origin of Thermal Degradation of Sr2–XSi5N8:Eux Phosphors in Air for Light-Emitting Diodes. *J. Am. Chem. Soc.* **2012**, *134* (34), 14108–14117. https://doi.org/10.1021/ja304754b.

(56) Pust, P.; Wochnik, A. S.; Baumann, E.; Schmidt, P. J.; Wiechert, D.; Scheu, C.; Schnick, W. $Ca[LiAl_3N_4]:Eu^{2+}$—A Narrow-Band Red-Emitting Nitridolithoaluminate. *Chem. Mater.* **2014**, *26* (11), 3544–3549. https://doi.org/10.1021/cm501162n.

(57) Pust, P.; Hintze, F.; Hecht, C.; Weiler, V.; Locher, A.; Zitnanska, D.; Harm, S.; Wiechert, D.; Schmidt, P. J.; Schnick, W. Group (III) Nitrides M[$Mg_2Al_2N_4$] (M = Ca, Sr, Ba, Eu) and Ba[$Mg_2Ga_2N_4$]—Structural Relation and Nontypical Luminescence Properties of Eu^{2+} Doped Samples. *Chem. Mater.* **2014**, *26* (21), 6113–6119. https://doi.org/10.1021/cm502280p.

(58) Tsai, Y.-T.; Chiang, C.-Y.; Zhou, W.; Lee, J.-F.; Sheu, H.-S.; Liu, R.-S. Structural Ordering and Charge Variation Induced by Cation Substitution in (Sr,Ca)AlSiN3:Eu Phosphor. *J. Am. Chem. Soc.* **2015**, *137* (28), 8936–8939. https://doi.org/10.1021/jacs.5b06080.

(59) Lü, W.; Lv, W.; Zhao, Q.; Jiao, M.; Shao, B.; You, H. A Novel Efficient Mn^{4+} Activated $Ca_{14}Al_{10}Zn_6O_{35}$ Phosphor: Application in Red-Emitting and White LEDs. *Inorg. Chem.* **2014**, *53* (22), 11985–11990. https://doi.org/10.1021/ic501641q.

(60) Wang, B.; Lin, H.; Xu, J.; Chen, H.; Wang, Y. CaMg2Al16O27:Mn4+-Based Red Phosphor: A Potential Color Converter for High-Powered Warm W-LED. *ACS Appl. Mater. Interfaces* **2014**, *6* (24), 22905–22913. https://doi.org/10.1021/am507316b.

(61) Zhu, H.; Lin, C. C.; Luo, W.; Shu, S.; Liu, Z.; Liu, Y.; Kong, J.; Ma, E.; Cao, Y.; Liu, R.-S.; Chen, X. Highly Efficient Non-Rare-Earth Red Emitting Phosphor for Warm White Light-Emitting Diodes. *Nature Communications* **2014**, *5*, 4312. https://doi.org/10.1038/ncomms5312.

(62) Peng, M.; Yin, X.; Tanner, P. A.; Brik, M. G.; Li, P. Site Occupancy Preference, Enhancement Mechanism, and Thermal Resistance of Mn^{4+} Red Luminescence in $Sr_4Al_{14}O_{25}$: Mn^{4+} for Warm WLEDs. *Chem. Mater.* **2015**, *27* (8), 2938–2945. https://doi.org/10.1021/acs.chemmater.5b00226.

(63) Singh, S. P.; Kim, M.; Park, W. B.; Lee, J.-W.; Sohn, K.-S. Discovery of a Red-Emitting $Li_3RbGe_8O_{18}$:Mn^{4+} Phosphor in the Alkali-Germanate System: Structural Determination and Electronic Calculations. *Inorg. Chem.* **2016**, *55* (20), 10310–10319. https://doi.org/10.1021/acs.inorgchem.6b01576.

(64) Zhou, Z.; Zhou, N.; Xia, M.; Yokoyama, M.; Hintzen, H. T. (Bert). Research Progress and Application Prospects of Transition Metal Mn4+-Activated Luminescent Materials. *J. Mater. Chem. C* **2016**, *4* (39), 9143–9161. https://doi.org/10.1039/C6TC02496C.

(65) Zhou, Q.; Dolgov, L.; Srivastava, A. M.; Zhou, L.; Wang, Z.; Shi, J.; Dramićanin, M. D.; Brik, M. G.; Wu, M. Mn2+ and Mn4+ Red Phosphors: Synthesis, Luminescence and Applications in WLEDs. A Review. *J. Mater. Chem. C* **2018**, *6* (11), 2652–2671. https://doi.org/10.1039/C8TC00251G.

(66) Omel'chenko, K. S.; Khmelenko, O. V.; Panchenko, T. V.; Volnyanskii, M. D. Photoluminescence of Manganese-Doped $LiNaGe_4O_9$ Crystals. *Phys. Solid State* **2014**, *56* (4), 751–756. https://doi.org/10.1134/S1063783414040246.

(67) Kunitomo J.; Suzuki R.; Takahashi Y.; Miyazaki T.; Terakado N.; Fujiwara T. Red-emissive Mn-doped $Li_2Ge_4O_9$ phase synthesized via glass-ceramic route. *J. Ceram. Soc. Japan* **2014**, *122* (1428), 725–727. https://doi.org/10.2109/jcersj2.122.725.

(68) Li, P.; Tan, L.; Wang, L.; Zheng, J.; Peng, M.; Wang, Y. Synthesis, Structure, and Performance of Efficient Red Phosphor LiNaGe4O9:Mn4+ and Its Application in Warm

WLEDs. *Journal of the American Ceramic Society* **2016**, *99* (6), 2029–2034. https://doi.org/10.1111/jace.14168.

(69) Ding, X.; Wang, Q.; Wang, Y. Rare-Earth-Free Red-Emitting $K_2Ge_4O_9:Mn^{4+}$ Phosphor Excited by Blue Light for Warm White LEDs. *Phys. Chem. Chem. Phys.* **2016**, *18* (11), 8088–8097. https://doi.org/10.1039/C6CP00168H.

(70) Baur, F.; Jüstel, T. Dependence of the Optical Properties of Mn^{4+} Activated $A_2Ge_4O_9$ (A=K,Rb) on Temperature and Chemical Environment. *Journal of Luminescence* **2016**, *177*, 354–360. https://doi.org/10.1016/j.jlumin.2016.04.046.

(71) Liang, S.; Shang, M.; Lian, H.; Li, K.; Zhang, Y.; Lin, J. Deep Red $MGe_4O_9:Mn^{4+}$ (M = Sr, Ba) Phosphors: Structure, Luminescence Properties and Application in Warm White Light Emitting Diodes. *J. Mater. Chem. C* **2016**, *4* (26), 6409–6416. https://doi.org/10.1039/C6TC01813K.

(72) Garcia, A.; Latourrette, B.; Fouassier, C. Ba5SiO4Cl6 : Eu , A New Blue-Emitting Photoluminescent Material with High Quenching Temperature. *J. Electrochem. Soc.* **1979**, *126* (10), 1734–1736. https://doi.org/10.1149/1.2128788.

(73) Meijerink, A.; Blasse, G.; Struye, L. A New Photostimulable Phosphor: Eu2+-Activated Bariumbromosilicate (Ba5SiO4Br6). *Materials Chemistry and Physics* **1989**, *21* (3), 261–270. https://doi.org/10.1016/0254-0584(89)90119-3.

(74) Schipper, W. J.; Blasse, G.; Leblans, P. Nb(V) as an Electron Trap in the Storage Phosphor Ba5SiO4Br6:Eu(II),Nb(V). *Chem. Mater.* **1994**, *6* (10), 1784–1789. https://doi.org/10.1021/cm00046a035.

(75) Ijdo, D. J. W.; Jansen, J.; Schipper, W. J. The Crystal Structure of Ba5SiO4Br6. *Materials Research Bulletin* **1992**, *27* (1), 45–51. https://doi.org/10.1016/0025-5408(92)90041-W.

(76) Abed, M.; Müller-Buschbaum, Hk. Zur Kristallstruktur von Ba5SiO4Cl6. *Journal of Alloys and Compounds* **1992**, *190* (1), 61–64. https://doi.org/10.1016/0925-8388(92)90174-8.

(77) Rezende, M. V. S.; Araújo, R. M.; Montes, P. J. R.; Valerio, M. E. G. Optical Properties of Rare-Earth Doped Sr3Al2O6. *Optical Materials* **2010**, *32* (10), 1341–1344. https://doi.org/10.1016/j.optmat.2010.04.015.

(78) Parmentier, A. B.; Smet, P. F.; Poelman, D. Broadband Luminescence in Rare Earth Doped Sr2SiS4: Relating Energy Levels of Ce3+ and Eu2+. *Materials* **2013**, *6* (8), 3663–3675. https://doi.org/10.3390/ma6083663.

(79) Herrmann, A.; Friedrich, D.; Zscheckel, T.; Rüssel, C. Luminescence Properties of Sm3+ Doped Alkali/Earth Alkali Orthoborates of the Type XZBO3 with X = Li, Na, Cs and Z = Ca, Sr, Ba. *Journal of Luminescence* **2019**, *214*, 116550. https://doi.org/10.1016/j.jlumin.2019.116550.

(80) Gibbs, G. V.; Ribbe, P. H. THE CRYSTAL STRUCTURES OF THE HUMITE MINERALS: I. NORBERGITE. *American Mineralogist* **1969**, *54*, p376–p389.

(81) Redhammer, G. J.; Roth, G.; Amthauer, G. Ca3GeO4Cl2 with a Norbergite-like Structure. *Acta Cryst C* **2007**, *63* (8), i69–i72. https://doi.org/10.1107/S0108270107030478.

(82) Blatov, V. A.; Shevchenko, A. P.; Proserpio, D. M. Applied Topological Analysis of Crystal Structures with the Program Package ToposPro. *Crystal Growth & Design* **2014**, *14* (7), 3576–3586. https://doi.org/10.1021/cg500498k.

(83) O'Keeffe, M.; Peskov, M. A.; Ramsden, S. J.; Yaghi, O. M. The Reticular Chemistry Structure Resource (RCSR) Database of, and Symbols for, Crystal Nets. *Acc. Chem. Res.* **2008**, *41* (12), 1782–1789. https://doi.org/10.1021/ar800124u.

(84) Schubert, E. F.; Kim, J. K. Solid-State Light Sources Getting Smart. *Science* **2005**, *308* (5726), 1274–1278. https://doi.org/10.1126/science.1108712.

(85) Pimputkar, S.; Speck, J. S.; DenBaars, S. P.; Nakamura, S. Prospects for LED Lighting. *Nature Photonics* **2009**, *3* (4), 180–182. https://doi.org/10.1038/nphoton.2009.32.

(86) Bergh, A.; Craford, G.; Duggal, A.; Haitz, R. The Promise and Challenge of Solid-State Lighting. *Physics Today* **2001**, *54* (12), 42–47. https://doi.org/10.1063/1.1445547.

(87) *Use of electricity - U.S. Energy Information Administration (EIA)*. https://www.eia.gov/energyexplained/electricity/use-of-electricity.php (accessed 2021-04-09).

(88) Nakamura, S.; Fasol, G. *The Blue Laser Diode: GaN Based Light Emitters and Lasers*; Springer-Verlag: Berlin Heidelberg, 1997. https://doi.org/10.1007/978-3-662-03462-0.

(89) Kimura, N.; Sakuma, K.; Hirafune, S.; Asano, K.; Hirosaki, N.; Xie, R.-J. Extrahigh Color Rendering White Light-Emitting Diode Lamps Using Oxynitride and Nitride Phosphors Excited by Blue Light-Emitting Diode. *Appl. Phys. Lett.* **2007**, *90* (5), 051109. https://doi.org/10.1063/1.2437090.

(90) Lin, C. C.; Zheng, Y. S.; Chen, H. Y.; Ruan, C. H.; Xiao, G. W.; Liu, R. S. Improving Optical Properties of White LED Fabricated by a Blue LED Chip with Yellow/Red Phosphors. *J. Electrochem. Soc.* **2010**, *157* (9), H900. https://doi.org/10.1149/1.3465654.

(91) Brik, M. G.; Camardello, S. J.; Srivastava, A. M. Influence of Covalency on the Mn^{4+} $^2E_g \rightarrow {}^4A_{2g}$ Emission Energy in Crystals. *ECS J. Solid State Sci. Technol.* **2015**, *4* (3), R39–R43. https://doi.org/10.1149/2.0031503jss.

(92) Xia, Z.; Liu, Q. Progress in Discovery and Structural Design of Color Conversion Phosphors for LEDs. *Progress in Materials Science* **2016**, *84*, 59–117. https://doi.org/10.1016/j.pmatsci.2016.09.007.

(93) Kröger, F. A.; Urbach, F. Some Aspects of the Luminescence of Solids. *Physics Today* **2009**, *1* (7), 24. https://doi.org/10.1063/1.3066188.

(94) Brik, M. G.; Srivastava, A. M. On the Optical Properties of the Mn4+ Ion in Solids. *Journal of Luminescence* **2013**, *133*, 69–72. https://doi.org/10.1016/j.jlumin.2011.08.047.

(95) Novikov, S.; Bagum, R.; Yan, Z. B.; Clancy, J. P.; Mozharivskyj, Y. Two New Magnesium and Magnesium-Lead Fluorogermanates and Revision of the $Mg_{28}Ge_{7.5}O_{38}F_{10}$ Phase. *Journal of Solid State Chemistry* **2020**, 121741. https://doi.org/10.1016/j.jssc.2020.121741.

(96) Xue, J.; Ran, W.; Noh, H. M.; Choi, B. C.; Park, S. H.; Jeong, J. H.; Kim, J. H. Influence of Alkaline Ions on the Luminescent Properties of Mn^{4+}-Doped MGe_4O_9 (M = Li_2, LiNa and K_2) Red-Emitting Phosphors. *Journal of Luminescence* **2017**, *192*, 1072–1083. https://doi.org/10.1016/j.jlumin.2017.08.036.

(97) Li, P.; Brik, M. G.; Li, L.; Han, J.; Li, X.; Peng, M. Prediction on Mn^{4+}-Doped Germanate Red Phosphor by Crystal Field Calculation on Basis of Exchange Charge Model: A Case Study on $K_2Ge_4O_9$:Mn^{4+}. *Journal of the American Ceramic Society* **2016**, *99* (7), 2388–2394. https://doi.org/10.1111/jace.14236.

(98) Baumgartner, O.; Völlenkle, H. Die Kristallstruktur des Tetragermanats $K_2Ba[Ge_4O_9]_2$. *Monatshefte für Chemie* **1978**, *109* (5), 1145–1153. https://doi.org/10.1007/BF00913016.

(99) Fleet, M. E.; Muthupari, S. Structure of $A_2Ge_4O_9$-Type Sodium Tetragermanate ($Na_2Ge_4O_9$) and Comparison with Other Alkali Germanate and Silicate Mixed Tetrahedral–Octahedral Framework Structures. *Journal of Solid State Chemistry* **1998**, *140* (2), 175–181. https://doi.org/10.1006/jssc.1998.7839.

(100) Redhammer, G. J.; Tippelt, G. The Tetra-germanates $A_2Ge_4O_9$ (A = Na, K and Rb). *Acta Cryst C* **2013**, *69* (9), 995–1001. https://doi.org/10.1107/S0108270113020921.

(101) Smolin, Yu. I. Crystal Structure of Barium Tetragermanate. *Doklady Akademii Nauk SSSR* **1968**, *181*, p595–p598.

(102) Pendlebury, G. B. Catapleiite from Saint Hilaire Mountain, Quebec. *The Canadian Mineralogist* **1964**, *8* (1), 120–121.

(103) Fischer, K. Verfeinerung Der Kristallstruktur von Benitoit $BaTi[Si_3O_9]$. *Zeitschrift für Kristallographie* **1969**, *129* (1–4), 222–243. https://doi.org/10.1524/zkri.1969.129.1-4.222.

(104) O'Keeffe, M. Coordination Sequences for Lattices. *Zeitschrift für Kristallographie - Crystalline Materials* **2010**, *210* (12), 905–908. https://doi.org/10.1524/zkri.1995.210.12.905.

(105) Nguyen, Q. B.; Chen, C.-L.; Chiang, Y.-W.; Lii, K.-H. $Cs_3UGe_7O_{18}$: A Pentavalent Uranium Germanate Containing Four- and Six-Coordinate Germanium. *Inorg. Chem.* **2012**, *51* (6), 3879–3882. https://doi.org/10.1021/ic3000872.

(106) Riseberg, L. A.; Weber, M. J. Spectrum and Anomalous Temperature Dependence of the $^2E \rightarrow {}^4A_2$ Emission of $Y_3Al_5O_{12}$: Mn^{4+}. *Solid State Communications* **1971**, *9* (11), 791–794. https://doi.org/10.1016/0038-1098(71)90565-5.

(107) Brik, M. G.; Srivastava, A. M. Critical Review—A Review of the Electronic Structure and Optical Properties of Ions with d^3 Electron Configuration (V^{2+} , Cr^{3+} , Mn^{4+} , Fe^{5+}) and Main Related Misconceptions. *ECS J. Solid State Sci. Technol.* **2018**, *7* (1), R3079–R3085. https://doi.org/10.1149/2.0041801jss.

(108) Shi, L.; Wang, S.; Han, Y.; Ji, Z.; Ma, D.; Mu, Z.; Mao, Z.; Wang, D.; Zhang, Z.; Liu, L. $Sr_2LaSbO_6:Mn^{4+}$ Far-Red Phosphor for Plant Cultivation: Synthesis, Luminescence Properties and Emission Enhancement by Al^{3+} Ions. *Journal of Luminescence* **2020**, *221*, 117091. https://doi.org/10.1016/j.jlumin.2020.117091.

(109) Kang, X.; Yang, W.; Ling, D.; Jia, C.; Lü, W. A Novel Far-Red Emitting Phosphor Activated $Ba_2LuTaO_6:Mn^{4+}$: Crystal Structure, Optical Properties and Application in Plant Growth Lighting. *Materials Research Bulletin* **2021**, *140*, 111301. https://doi.org/10.1016/j.materresbull.2021.111301.

(110) Carone, D.; Usman, M.; Klepov, V. V.; Smith, M. D.; Kocevski, V.; Besmann, T. M.; Loye, H.-C. zur. New Germanate and Mixed Cobalt Germanate Salt Inclusion Materials: $[(Rb_6F)(Rb_4F)][Ge_{14}O_{32}]$ and $[(Rb_6F)(Rb_{3.1}Co_{0.9}F_{0.96})][Co_{3.8}Ge_{10.2}O_{30}F_2]$. *CrystEngComm* **2020**, *22* (46), 8072–8080. https://doi.org/10.1039/D0CE01099E.

(111) Usman, M.; Kocevski, V.; Smith, M. D.; Morrison, G.; Zhang, W.; Besmann, T.; Halasyamani, P. Shiv.; zur Loye, H.-C. Polymorphism and Molten Nitrate Salt-Assisted Single Crystal to Single Crystal Ion Exchange in the Cesium Ferrogermanate Zeotype: $CsFeGeO_4$. *Inorg. Chem.* **2020**, *59* (14), 9699–9709. https://doi.org/10.1021/acs.inorgchem.0c00936.

(112) Usman, M.; Smith, M. D.; Kocevski, V.; Besmann, T.; Loye, H.-C. zur. Complex Cobalt Silicates and Germanates Crystallizing in a Porous Three-Dimensional Framework Structure. *CrystEngComm* **2020**, *22* (6), 1112–1119. https://doi.org/10.1039/C9CE01662G.

(113) Carone, D.; Morrison, G.; Smith, M. D.; zur Loye, H.-C. Crystal Growth of New Germanate Framework Structures: Impact of the Presence of Square Planar Copper Species and Mixed Ge/Mn Sites on the Overall Structures of $Rb_2Cu_3Ge_5O_{14}$, $Cs_2Cu_3Ge_5O_{14}$, $Cs_7Cu_2Ge_{11}O_{27}F$, and $[(Cs_6F)(Cs_3AgF)][Ge_{12}Mn_2O_{32}]$. *Crystal Growth & Design* **2022**. https://doi.org/10.1021/acs.cgd.2c00133.

(114) Liebau, F. *Structural Chemistry of Silicates: Structure, Bonding, and Classification*; Springer Science & Business Media, 2012.

(115) Ding, X.; Zhu, G.; Geng, W.; Wang, Q.; Wang, Y. Rare-Earth-Free High-Efficiency Narrow-Band Red-Emitting Mg3Ga2GeO8:Mn4+ Phosphor Excited by Near-UV Light for White-Light-Emitting Diodes. *Inorg. Chem.* **2016**, *55* (1), 154–162. https://doi.org/10.1021/acs.inorgchem.5b02048.

(116) Takahashi, Y.; Fujiwara, T.; Benino, Y.; Komatsu, T. Crystallization and Raman Spectra of Langasite-Type $Na_2CaGe_6O_{14}$, $Na_2SrGe_6O_{14}$ and $Pb_3Ga_2Ge_4O_{14}$ in Corresponding Glasses. *Key Engineering Materials* **2010**, 213–216. https://doi.org/10.4028/www.scientific.net/KEM.421-422.213.

(117) Takeda, H.; Uecker, R.; Kumatoriya, M.; Shimamura, K.; Reiche, P.; Fukuda, T. Growth and Characterization of $Na_2CaGe_6O_{14}$ Single Crystals. *Crystal Research and Technology* **1997**, *32* (7), 939–945. https://doi.org/10.1002/crat.2170320707.

(118) Pust, P.; Schmidt, P. J.; Schnick, W. A Revolution in Lighting. *Nature Mater* **2015**, *14* (5), 454–458. https://doi.org/10.1038/nmat4270.

(119) Amarasinghe, D. K.; Rabuffetti, F. A. Bandshift Luminescence Thermometry Using Mn^{4+}:$Na_4Mg(WO_4)_3$ Phosphors. *Chem. Mater.* **2019**, *31* (24), 10197–10204. https://doi.org/10.1021/acs.chemmater.9b03886.

(120) Cai, P.; Wang, X.; Seo, H. J. Excitation Power Dependent Optical Temperature Behaviors in Mn^{4+} Doped Oxyfluoride $Na_2WO_2F_4$. *Phys. Chem. Chem. Phys.* **2018**, *20* (3), 2028–2035. https://doi.org/10.1039/C7CP07123J.

(121) Glais, E.; Đorđević, V.; Papan, J.; Viana, B.; Dramićanin, M. D. $MgTiO_3$:Mn^{4+} a Multi-Reading Temperature Nanoprobe. *RSC Adv.* **2018**, *8* (33), 18341–18346. https://doi.org/10.1039/C8RA02482K.

(122) Tang, X.; Li, X.; Zou, Z.; Ma, Z.; Zhang, J.; Wang, Z.; Ci, Z.; Wang, D.; Peng, S.; Li, H.; Wang, Y. A Thermal-Sensitizing and Thermochromic Phosphor. *J. Mater. Chem. C* **2017**, *5* (39), 10369–10374. https://doi.org/10.1039/C7TC03833J.

(123) Dunaeva, E. E.; Ivleva, L. I.; Doroshenko, M. E.; Boldyrev, K. N.; Papashvili, A. G. Growth and Spectral-Luminescence Characteristics of Modified BGO Crystals. *Journal of Crystal Growth* **2019**, *525*, 125205. https://doi.org/10.1016/j.jcrysgro.2019.125205.

(124) Lipina, O. A.; Melkozerova, M. A.; Chufarov, A. Yu.; Baklanova, Y. V.; Surat, L. L.; Tyutyunnik, A. P.; Zubkov, V. G. Structure–Luminescence Relationship in Eu^{3+}-Doped $Sr_3La_2(Ge_3O_9)_2$ Phosphors. *Optical Materials* **2019**, *87*, 145–150. https://doi.org/10.1016/j.optmat.2018.04.006.

(125) Huang, Q.; Ye, W.; Hu, G.; Liu, X. Strong Red Emission in Bi^{3+} and Mn^{4+} Codoped $Mg_{3.5}Ge_{1.25}O_6$ Phosphors Applied in Optical Agriculture. *Journal of Luminescence* **2019**, *210*, 89–95. https://doi.org/10.1016/j.jlumin.2019.01.047.

(126) Hyoung Jung, I.; Ho Auh, K. Crystal Growth and Piezoelectric Properties of Langasite ($La_3Ga_5SiO_{14}$) Crystals. *Materials Letters* **1999**, *41* (5), 241–246. https://doi.org/10.1016/S0167-577X(99)00137-8.

(127) Nishi, F. Strontium Tetragermanate, $SrGe_4O_9$. *Acta Cryst C* **1996**, *52* (10), 2393–2395. https://doi.org/10.1107/S0108270196006737.

(128) Redhammer, G. J.; Tippelt, G. The Polar Phase of $Li_2Ge_4O_9$ at 298, 150 and 90 K. *Acta Cryst C* **2013**, *69* (10), 1091–1095. https://doi.org/10.1107/S0108270113025110.

(129) Kubelka, P.; Munk, F. Ein Beitrag Zur Optik Der Farbanstriche. *Zeitschrift für Technische Physik* **1931**, *12*, 593–601.

(130) *Modern Aspects of Reflectance Spectroscopy*; Wendlandt, W. W., Ed.; Springer US, 1968. https://doi.org/10.1007/978-1-4684-7182-3.

(131) Kresse, G.; Furthmüller, J. Efficiency of Ab-Initio Total Energy Calculations for Metals and Semiconductors Using a Plane-Wave Basis Set. *Computational Materials Science* **1996**, *6* (1), 15–50. https://doi.org/10.1016/0927-0256(96)00008-0.

(132) Kresse, G.; Furthmüller, J. Efficient Iterative Schemes for Ab Initio Total-Energy Calculations Using a Plane-Wave Basis Set. *Phys. Rev. B* **1996**, *54* (16), 11169–11186. https://doi.org/10.1103/PhysRevB.54.11169.

(133) Perdew, J. P.; Burke, K.; Ernzerhof, M. Generalized Gradient Approximation Made Simple. *Phys. Rev. Lett.* **1996**, *77* (18), 3865–3868. https://doi.org/10.1103/PhysRevLett.77.3865.

(134) Blöchl, P. E. Projector Augmented-Wave Method. *Phys. Rev. B* **1994**, *50* (24), 17953–17979. https://doi.org/10.1103/PhysRevB.50.17953.

(135) Kresse, G.; Joubert, D. From Ultrasoft Pseudopotentials to the Projector Augmented-Wave Method. *Phys. Rev. B* **1999**, *59* (3), 1758–1775. https://doi.org/10.1103/PhysRevB.59.1758.

(136) Zachariasen, W. H. The Crystal Structure of Benitoite $BaTiSi_3O_9$. *Z. Kristallogr.* **1930**, *74*, 139–146.

(137) Bush, A. A.; Stefanovich, S. Yu. Piezoelectric and Nonlinear Optical Properties of PbGe4O9 Crystals. *Inorganic Materials* **2002**, *38* (2), 168–171. https://doi.org/10.1023/A:1014073329197.

(138) *APEX4 Software*. https://www.bruker.com/en/products-and-solutions/diffractometers-and-scattering-systems/single-crystal-x-ray-diffractometers/sc-xrd-software/apex.html (accessed 2021-10-22).

(139) Kaminskii, A. A.; Mill, B. V.; Khodzhabagyan, G. G.; Konstantinova, A. F.; Okorochkov, A. I.; Silvestrova, I. M. Investigation of Trigonal $(La_{1-x}Nd_x)_3Ga_5SiO_{14}$ Crystals. I. Growth and Optical Properties. *physica status solidi (a)* **1983**, *80* (1), 387–398. https://doi.org/10.1002/pssa.2210800142.

(140) Novikov, S. A.; Mozharivskyj, Y. Synthesis and Structure of the Na–Ba and Rb–Ba Octagermanates and Phosphorescence of the $Rb_2BaGe_{8-x}O_{18}$:XMn^{4+} Series. *Journal of Solid State Chemistry* **2021**, *304*, 122607. https://doi.org/10.1016/j.jssc.2021.122607.

(141) Lin, H.; Hu, T.; Huang, Q.; Cheng, Y.; Wang, B.; Xu, J.; Wang, J.; Wang, Y. Non-Rare-Earth K_2XF_7:Mn^{4+} (X = Ta, Nb): A Highly-Efficient Narrow-Band Red Phosphor Enabling the Application in Wide-Color-Gamut LCD. *Laser & Photonics Reviews* **2017**, *11* (6), 1700148. https://doi.org/10.1002/lpor.201700148.

(142) Wang, B.; Lin, H.; Huang, F.; Xu, J.; Chen, H.; Lin, Z.; Wang, Y. Non-Rare-Earth $BaMgAl_{10-2x}O17$:XMn^{4+},XMg^{2+}: A Narrow-Band Red Phosphor for Use as a High-Power Warm w-LED. *Chem. Mater.* **2016**, *28* (10), 3515–3524. https://doi.org/10.1021/acs.chemmater.6b01303.

(143) Li, X.; Chen, Z.; Wang, B.; Liang, R.; Li, Y.; Kang, L.; Liu, P. Effects of Impurity Doping on the Luminescence Performance of Mn^{4+}-Doped Aluminates with the Magnetoplumbite-Type Structure for Plant Cultivation. *Materials (Basel)* **2018**, *12* (1). https://doi.org/10.3390/ma12010086.

(144) Shao, Q.; Lin, H.; Hu, J.; Dong, Y.; Jiang, J. Temperature-Dependent Photoluminescence Properties of Deep-Red Emitting Mn^{4+}-Activated Magnesium Fluorogermanate Phosphors. *Journal of Alloys and Compounds* **2013**, *552*, 370–375. https://doi.org/10.1016/j.jallcom.2012.11.078.

(145) Uylings, P. H. M.; Raassen, A. J. J.; Wyart, J. F. Energies of N Equivalent Electrons Expressed in Terms of Two-Electron Energies and Independent Three-Electron Parameters: A New Complete Set of Orthogonal Operators. II. Application to $3d^N$ Configurations. *J. Phys. B: At. Mol. Phys.* **1984**, *17* (20), 4103–4126. https://doi.org/10.1088/0022-3700/17/20/010.

(146) Bhushan, S.; Chukichev, M. V. Temperature Dependent Studies of Cathodoluminescence of Green Band of ZnO Crystals. *J Mater Sci Lett* **1988**, *7* (4), 319–321. https://doi.org/10.1007/BF01730729.

(147) Ballhausen, C. J.; Gray, H. B. *Molecular Orbital Theory*; W. A. Benjamin, Inc., New York, 1965.

(148) Dunn, B.; Kamath, H.; Tarascon, J.-M. Electrical Energy Storage for the Grid: A Battery of Choices. *Science* **2011**, *334* (6058), 928–935. https://doi.org/10.1126/science.1212741.

(149) Palomares, V.; Casas-Cabanas, M.; Castillo-Martínez, E.; Han, M. H.; Rojo, T. Update on Na-Based Battery Materials. A Growing Research Path. *Energy Environ. Sci.* **2013**, *6* (8), 2312–2337. https://doi.org/10.1039/C3EE41031E.

(150) Sawicki, M.; Shaw, L. L. Advances and Challenges of Sodium Ion Batteries as Post Lithium Ion Batteries. *RSC Adv.* **2015**, *5* (65), 53129–53154. https://doi.org/10.1039/C5RA08321D.

(151) Eftekhari, A.; Kim, D.-W. Sodium-Ion Batteries: New Opportunities beyond Energy Storage by Lithium. *Journal of Power Sources* **2018**, *395*, 336–348. https://doi.org/10.1016/j.jpowsour.2018.05.089.

(152) Muldoon, J.; Bucur, C. B.; Gregory, T. Quest for Nonaqueous Multivalent Secondary Batteries: Magnesium and Beyond. *Chem. Rev.* **2014**, *114* (23), 11683–11720. https://doi.org/10.1021/cr500049y.

(153) Canepa, P.; Sai Gautam, G.; Hannah, D. C.; Malik, R.; Liu, M.; Gallagher, K. G.; Persson, K. A.; Ceder, G. Odyssey of Multivalent Cathode Materials: Open Questions and Future Challenges. *Chem. Rev.* **2017**, *117* (5), 4287–4341. https://doi.org/10.1021/acs.chemrev.6b00614.

(154) Liang, Y.; Dong, H.; Aurbach, D.; Yao, Y. Current Status and Future Directions of Multivalent Metal-Ion Batteries. *Nature Energy* **2020**, *5* (9), 646–656. https://doi.org/10.1038/s41560-020-0655-0.

(155) Kim, S.-W.; Seo, D.-H.; Ma, X.; Ceder, G.; Kang, K. Electrode Materials for Rechargeable Sodium-Ion Batteries: Potential Alternatives to Current Lithium-Ion Batteries. *Advanced Energy Materials* **2012**, *2* (7), 710–721. https://doi.org/10.1002/aenm.201200026.

(156) Slater, M. D.; Kim, D.; Lee, E.; Johnson, C. S. Sodium-Ion Batteries. *Advanced Functional Materials* **2013**, *23* (8), 947–958. https://doi.org/10.1002/adfm.201200691.

(157) Kundu, D.; Talaie, E.; Duffort, V.; Nazar, L. F. The Emerging Chemistry of Sodium Ion Batteries for Electrochemical Energy Storage. *Angewandte Chemie International Edition* **2015**, *54* (11), 3431–3448. https://doi.org/10.1002/anie.201410376.

(158) Ponrouch, A.; Dedryvère, R.; Monti, D.; Demet, A. E.; Mba, J. M. A.; Croguennec, L.; Masquelier, C.; Johansson, P.; Palacín, M. R. Towards High Energy Density Sodium Ion Batteries through Electrolyte Optimization. *Energy Environ. Sci.* **2013**, *6* (8), 2361–2369. https://doi.org/10.1039/C3EE41379A.

(159) Ponrouch, A.; Marchante, E.; Courty, M.; Tarascon, J.-M.; Palacín, M. R. In Search of an Optimized Electrolyte for Na-Ion Batteries. *Energy Environ. Sci.* **2012**, *5* (9), 8572–8583. https://doi.org/10.1039/C2EE22258B.

(160) Che, H.; Chen, S.; Xie, Y.; Wang, H.; Amine, K.; Liao, X.-Z.; Ma, Z.-F. Electrolyte Design Strategies and Research Progress for Room-Temperature Sodium-Ion Batteries. *Energy Environ. Sci.* **2017**, *10* (5), 1075–1101. https://doi.org/10.1039/C7EE00524E.

(161) Zhang, J.; Yao, X.; Misra, R. K.; Cai, Q.; Zhao, Y. Progress in Electrolytes for Beyond-Lithium-Ion Batteries. *Journal of Materials Science & Technology* **2020**, *44*, 237–257. https://doi.org/10.1016/j.jmst.2020.01.017.

(162) Goodenough, J. B.; Hong, H. Y.-P.; Kafalas, J. A. Fast Na+-Ion Transport in Skeleton Structures. *Materials Research Bulletin* **1976**, *11* (2), 203–220. https://doi.org/10.1016/0025-5408(76)90077-5.

(163) Hong, H. Y.-P. Crystal Structures and Crystal Chemistry in the System Na1+xZr2SixP3−xO12. *Materials Research Bulletin* **1976**, *11* (2), 173–182. https://doi.org/10.1016/0025-5408(76)90073-8.

(164) Lang, G. Strukturvergleiche an ternären und quarternären Oxiden. *Zeitschrift für anorganische und allgemeine Chemie* **1966**, *348* (5–6), 246–256. https://doi.org/10.1002/zaac.19663480505.

(165) Yung-Fang Yu Yao; Kummer, J. T. Ion Exchange Properties of and Rates of Ionic Diffusion in Beta-Alumina. *Journal of Inorganic and Nuclear Chemistry* **1967**, *29* (9), 2453–2475. https://doi.org/10.1016/0022-1902(67)80301-4.

(166) Boilot, J. P.; Collin, G.; Colomban, Ph.; Comes, R. X-Ray-Scattering Study of the Fast-Ion Conductor β''-Alumina. *Phys. Rev. B* **1980**, *22* (12), 5912–5923. https://doi.org/10.1103/PhysRevB.22.5912.

(167) Sutter, P. H.; Cratty, L.; Saltzberg, M.; Farrington, G. C. Diffusion and Conductivity in Na+Cd2+ β Alumina. *Solid State Ionics* **1983**, *9–10*, 295–298. https://doi.org/10.1016/0167-2738(83)90250-3.

(168) Edström, K.; Thomas, J. O.; Farrington, G. C. Structural Aspects of the Na+ → Cd2+ Ion-Exchange Process in Na+ β-Alumina. *Acta Cryst B* **1991**, *47* (5), 635–643. https://doi.org/10.1107/S0108768191003075.

(169) Zhao, L. N.; Zhang, T.; Zhao, H. L.; Hou, Y. L. Polyanion-Type Electrode Materials for Advanced Sodium-Ion Batteries. *Materials Today Nano* **2020**, *10*, 100072. https://doi.org/10.1016/j.mtnano.2020.100072.

(170) Rajagopalan, R.; Zhang, Z.; Tang, Y.; Jia, C.; Ji, X.; Wang, H. Understanding Crystal Structures, Ion Diffusion Mechanisms and Sodium Storage Behaviors of NASICON Materials. *Energy Storage Materials* **2021**, *34*, 171–193. https://doi.org/10.1016/j.ensm.2020.09.007.

(171) Giannozzi, P.; Baroni, S.; Bonini, N.; Calandra, M.; Car, R.; Cavazzoni, C.; Ceresoli, D.; Chiarotti, G. L.; Cococcioni, M.; Dabo, I.; Corso, A. D.; Gironcoli, S. de; Fabris, S.; Fratesi, G.; Gebauer, R.; Gerstmann, U.; Gougoussis, C.; Kokalj, A.; Lazzeri, M.; Martin-Samos, L.; Marzari, N.; Mauri, F.; Mazzarello, R.; Paolini, S.; Pasquarello, A.; Paulatto, L.; Sbraccia, C.; Scandolo, S.; Sclauzero, G.; Seitsonen, A. P.; Smogunov, A.; Umari, P.; Wentzcovitch, R. M. QUANTUM ESPRESSO: A Modular and Open-Source Software Project for Quantum Simulations of Materials. *J. Phys.: Condens. Matter* **2009**, *21* (39), 395502. https://doi.org/10.1088/0953-8984/21/39/395502.

(172) Giannozzi, P.; Baseggio, O.; Bonfà, P.; Brunato, D.; Car, R.; Carnimeo, I.; Cavazzoni, C.; de Gironcoli, S.; Delugas, P.; Ferrari Ruffino, F.; Ferretti, A.; Marzari, N.; Timrov, I.; Urru, A.; Baroni, S. Quantum ESPRESSO toward the Exascale. *J. Chem. Phys.* **2020**, *152* (15), 154105. https://doi.org/10.1063/5.0005082.

(173) Dal Corso, A. Pseudopotentials Periodic Table: From H to Pu. *Computational Materials Science* **2014**, *95*, 337–350. https://doi.org/10.1016/j.commatsci.2014.07.043.

(174) Prandini, G.; Marrazzo, A.; Castelli, I. E.; Mounet, N.; Marzari, N. Precision and Efficiency in Solid-State Pseudopotential Calculations. *npj Comput Mater* **2018**, *4* (1), 1–13. https://doi.org/10.1038/s41524-018-0127-2.

(175) Lejaeghere, K.; Bihlmayer, G.; Björkman, T.; Blaha, P.; Blügel, S.; Blum, V.; Caliste, D.; Castelli, I. E.; Clark, S. J.; Dal Corso, A.; de Gironcoli, S.; Deutsch, T.; Dewhurst, J. K.; Di Marco, I.; Draxl, C.; Dułak, M.; Eriksson, O.; Flores-Livas, J. A.; Garrity, K. F.; Genovese, L.; Giannozzi, P.; Giantomassi, M.; Goedecker, S.; Gonze, X.; Grånäs, O.; Gross, E. K. U.; Gulans, A.; Gygi, F.; Hamann, D. R.; Hasnip, P. J.; Holzwarth, N. A. W.; Iuşan, D.; Jochym, D. B.; Jollet, F.; Jones, D.; Kresse, G.; Koepernik, K.; Küçükbenli, E.; Kvashnin, Y. O.; Locht, I. L. M.; Lubeck, S.; Marsman, M.; Marzari, N.; Nitzsche, U.; Nordström, L.; Ozaki, T.; Paulatto, L.; Pickard, C. J.; Poelmans, W.; Probert, M. I. J.; Refson, K.; Richter, M.; Rignanese, G.-M.; Saha, S.; Scheffler, M.; Schlipf, M.; Schwarz, K.; Sharma, S.; Tavazza, F.; Thunström, P.; Tkatchenko, A.; Torrent, M.; Vanderbilt, D.; van Setten, M. J.; Van Speybroeck, V.; Wills, J. M.; Yates, J. R.; Zhang, G.-X.; Cottenier, S. Reproducibility in Density Functional Theory Calculations of Solids. *Science* **2016**, *351* (6280), aad3000. https://doi.org/10.1126/science.aad3000.

(176) Brown, I. D. Recent Developments in the Methods and Applications of the Bond Valence Model. *Chem. Rev.* **2009**, *109* (12), 6858–6919. https://doi.org/10.1021/cr900053k.

(177) Adams, S. Relationship between Bond Valence and Bond Softness of Alkali Halides and Chalcogenides. *Acta Cryst B* **2001**, *57* (3), 278–287. https://doi.org/10.1107/S0108768101003068.

(178) Adams, S. From Bond Valence Maps to Energy Landscapes for Mobile Ions in Ion-Conducting Solids. *Solid State Ionics* **2006**, *177* (19), 1625–1630. https://doi.org/10.1016/j.ssi.2006.03.054.

(179) Adams, S.; Rao, R. P. Understanding Ionic Conduction and Energy Storage Materials with Bond-Valence-Based Methods. In *Bond Valences*; Brown, I. D., Poeppelmeier, K. R., Eds.; Springer: Berlin, Heidelberg, 2014; pp 129–159. https://doi.org/10.1007/430_2013_137.

(180) Rodríguez-Carvajal, J. Recent Advances in Magnetic Structure Determination by Neutron Powder Diffraction. *Physica B: Condensed Matter* **1993**, *192* (1), 55–69. https://doi.org/10.1016/0921-4526(93)90108-I.

(181) Momma, K.; Izumi, F. VESTA 3 for Three-Dimensional Visualization of Crystal, Volumetric and Morphology Data. *J Appl Cryst* **2011**, *44* (6), 1272–1276. https://doi.org/10.1107/S0021889811038970.

(182) Safronov, A. N.; Nevskii, N. N.; Ilyukhin, V. V.; Belov, N. V. A New Tetrahedral Radical (Ge_5O_{16}) in the Structure $Na_4Sn_2(Ge_5O_{16})(H_2O)$ (in Russian). *Dokl. Akad. Nauk. SSSR* **1982**, *267* (4), 850–853.

(183) Safronov, A. N.; Nevskii, N. N.; Ilyukhin, V. V.; Belov, N. V. A new type of silicate radical (Si_5O_{16}) in the structure $Na_4Sn_2(Si_5O_{16})(H_2O)$ (in Russian). *Dokl. Akad. Nauk. SSSR* **1983**, *269*, 850–852.

(184) Smith, A.; Baumard, J.; Abélard, P.; Denanot, M. Ac Impedance Measurements and V-I Characteristics for Co-, Mn-, or Bi-doped ZnO. *Journal of Applied Physics* **1989**, *65* (12), 5119–5125. https://doi.org/10.1063/1.343190.

(185) Zhao, C.; Liu, L.; Qi, X.; Lu, Y.; Wu, F.; Zhao, J.; Yu, Y.; Hu, Y.-S.; Chen, L. Solid-State Sodium Batteries. *Advanced Energy Materials* **2018**, *8* (17), 1703012. https://doi.org/10.1002/aenm.201703012.